

Synthesis and Characterization of Dynamic Covalent Materials

Zur Erlangung des akademischen Grades eines

DOKTORS DER NATURWISSENSCHAFTEN

(Dr. rer. nat.)

von der KIT-Fakultät für Chemie und Biowissenschaften

des Karlsruher Instituts für Technologie (KIT)

genehmigte

DISSERTATION

von

Qi An

aus

Qingdao, Shandong, V.R. China

KIT-Dekan: Prof Reinhard Fischer

Referent: KIT Associate Fellow Dr. Manuel Tsotsalas

Korreferent: Prof. Patrick Théato

Tag der mündlichen Prüfung: 09.05.2019



This document – excluding the pictures and graphs – is licensed under a Creative Commons Attribution-Non Commercial – Share Alike 4.0 International License (CC BY-NC-SA 4.0):
<https://creativecommons.org/licenses/by-nc-sa/4.0/deed.en>

Eidesstattliche Erklärung

Ich versichere hiermit, dass ich diese Arbeit selbstständig angefertigt habe und keine anderen, als die angegebenen Quellen und Hinweise benutzt, sowie die wörtlich oder inhaltlich übernommenen Stellen als solche kenntlich gemacht und die Satzung des Karlsruher Instituts für Technologie (KIT) zur Sicherung guter wissenschaftlicher Praxis in der gültigen Fassung beachtet habe. Die elektronische Version der Arbeit stimmt mit der schriftlichen überein und die Abgabe und Archivierung der Primärdaten gemäß Abs. A (6) der Regeln zur Sicherung guter wissenschaftlicher Praxis des KIT beim Institut ist gesichert.

Karlsruhe, 27.05.2019

Die vorliegende Arbeit wurde im Zeitraum von Januar 2016 bis März 2019 unter Anleitung von Dr. Manuel Tsotsalas (Institut für Funktionelle Grenzflächen) des Karlsruher Institut für Technologie angefertigt.

Abstract

Polymeric frameworks have attracted huge interest due to their enormous potential and application perspectives. Controlling molecular structure of the polymeric framework is essential for tailoring the final macroscopic properties of the material to the desired application. By employing reversible covalent bonds in the framework formation, robust frameworks can be obtained with controllable crosslinking degree, which allows the structural adjustment for certain properties, like catalysis.

In this thesis, direct construction of polymeric frameworks from rigid molecular precursors via multifold nitroxide exchange reaction is introduced. This reaction offers new opportunities for polymer materials with precisely controllable and reversibly tuneable crosslinking degree, adjustable porosity as well as self-healing property. The reversible control can be easily performed by altering the reaction equilibrium. Beside the framework synthesis, the progress and the kinetics of the nitroxide exchange process can be precisely followed *in situ* via electron paramagnetic resonance (EPR), in case of different hyperfine coupling constants of the employed nitroxides. By using the EPR, the defect density of the polymeric framework can be also measured, which can be used for precise determination of the crosslinking degree. In addition to EPR, fluorescence spectroscopy can be used in case of employing profluorescent nitroxide species. By modulating the reaction equilibrium, the porosity and pore size can be adjusted for future application, especially in the field of catalysis. The alkoxyamine functional groups within the polymeric framework can be both utilized as dynamic bonds in the nitroxide exchange reaction, as well as initiator for nitroxide mediated polymerization (NMP). Using the multifold alkoxyamines, well defined prepolymers can be synthesized, which are later crosslinked to multifold nitroxides. In addition, nitroxide exchange reaction is also performed with thermally induced layer by layer method to synthesize thin films. Using mild and precise synthesis method, fast and efficient light induced layer by layer synthesis is further developed using thiol-yne coupling reaction as a model system.

Zusammenfassung

Aufgrund des enormen Potenzials in zahlreichen Anwendungsgebieten erwecken Polymer-Gerüstverbindungen weltweit großes Interesse unter Forschern. Dabei ist die Kontrolle über die molekulare Strukturierung essenziell für die Anpassung der makroskopischen Eigenschaften des Materials an die gewünschte Anwendung. Durch die Nutzung von reversiblen kovalenten Bindungen beim Aufbau der Netzwerkverbindungen werden robuste Gerüste mit kontrolliertem Vernetzungsgrad erzielt, welche sich auf bestimmte Anwendungen abstimmen lassen.

In der vorliegenden Arbeit werden Polymernetzwerke aus starren molekularen Ausgangsverbindungen mittels mehrfacher Nitroxid-Austauschreaktion aufgebaut. Diese Reaktion erlaubt es das Polymermaterial mit neuen Eigenschaften wie präzise und reversibel einstellbarem Vernetzungsgrad, anpassbarer Porosität und selbstheilenden Eigenschaften auszustatten. Die reversible Kontrolle über den Vernetzungsgrad kann durch Modulieren des Reaktionsgleichgewichts erreicht werden. Neben dem Aufbau der Polymerverbindung, kann der Fortschritt und die Kinetik der Nitroxid-Austauschreaktion präzise über der Elektronenspinresonanz-Spektroskopie (ESR) verfolgt werden. Auch die Defektdichte kann über ESR Spektroskopie präzise bestimmt werden, welche für die Berechnung des Vernetzungsgrads verwendet werden kann. Zusätzlich kann Fluoreszenzspektroskopie für die Untersuchung der Materialien herangezogen werden, wenn profluoreszierende Nitroxide eingesetzt werden. Durch Modulierung des Reaktionsgleichgewichts können die Porosität und die Porengrößen verändert werden, die eventuell für spätere Anwendung interessant werden können. Die Alkoxyamine können sowohl für die Aufbau der Polymerverbindungen als auch in der Nitroxid-vermittelten-Polymerisation (NMP) als Initiator eingesetzt werden. Unter Verwendung mehrarmiger Alkoxyaminen können mittels NMP wohldefinierte Vorpolymere hergestellt werden, die in dem nächsten Schritt mit mehrarmigen Nitroxiden vernetzt werden können. Um weitere Anwendungsfelder für diese Netzwerke zu eröffnen, wurde die Nitroxid-Austauschreaktion mit der thermisch induzierten Schicht-für-Schicht-Synthese auf Goldoberflächen angewendet. Um eine mildere und hochpräzise Synthesemethode zu finden wurden die schnelle und effiziente lichtinduzierte Schicht-für-Schicht-Synthese mittels Thiol-yne Kupplungsreaktion als Modellsystem entwickelt, die auch analog auf andere lichtinduzierte Systeme angewendet werden kann.

CONTENT

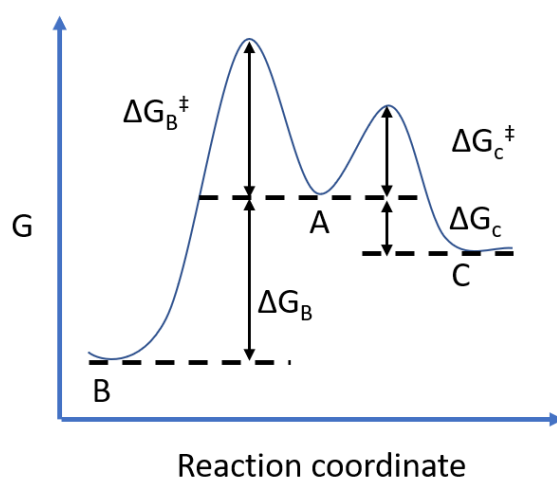
ABSTRACT	VII
ZUSAMMENFASSUNG	IX
1. INTRODUCTION.....	1
1.1 DYNAMIC COVALENT MATERIALS.....	1
1.2 NITROXIDE EXCHANGE REACTION	3
1.2.1 <i>Alkoxyamines</i>	5
1.2.2 <i>Nitroxides</i>	7
1.3 STIMULI RESPONSIVE MATERIALS	9
1.4 POROUS ORGANIC MATERIALS	11
2. METHODS.....	15
2.1 ELECTRON PARAMAGNETIC RESONANCE (EPR).....	15
2.1.1 <i>Theoretical background</i>	15
2.1.2 <i>Instrumental information</i>	17
2.2 GAS ADSORPTION.....	17
2.2.1 <i>Theoretical background</i>	17
2.2.2 <i>Instrumental information</i>	22
2.3 FLUORESCENCE SPECTROSCOPY	22
2.3.1 <i>Theoretical background</i>	22
2.3.2 <i>Instrumental information</i>	23
2.4 INFRARED SPECTROSCOPY (IR)	23
2.4.1 <i>Theoretical background</i>	23
2.4.2 <i>Attenuated Total Reflection (ATR)</i>	25
2.4.3 <i>Infrared reflection adsorption spectroscopy (IRRAS)</i>	25
2.4.4 <i>Instrumental information</i>	26
2.5 X-RAY DIFFRACTION (XRD)	27
2.5.1 <i>Theoretical background</i>	27
2.5.2 <i>Instrumental information</i>	27
2.6 MASS SPECTROMETRY	28
2.6.1 <i>Theoretical background</i>	28
2.6.2 <i>Electrospray Ionization Mass Spectrometry (ESI-MS)</i>	28
2.6.3 <i>Fast Atom Bombardment Mass Spectrometry (FAB-MS)</i>	28
2.6.4 <i>Time of Flight Secondary Ion Mass Spectrometry (ToF-SIMS)</i>	28
2.7 GEL PERMEATION CHROMATOGRAPHY (GPC)	29
2.7.1 <i>Theoretical background</i>	29
2.7.2 <i>Instrumental information</i>	29
2.8 NUCLEAR MAGNETIC RESONANCE SPECTROSCOPY (NMR)	30
2.8.1 <i>Theoretical background</i>	30
2.8.2 <i>Instrumental information</i>	30
2.9 THERMOGRAVIMETRIC ANALYSIS (TGA).....	30
2.9.1 <i>Theoretical background</i>	30
2.9.2 <i>Instrumental information</i>	31
2.10 DIFFERENTIAL SCANNING CALORIMETRY (DSC).....	31
2.10.1 <i>Theoretical background</i>	31
2.11 SPECTROSCOPIC ELLIPSOMETRY (SE)	31
2.11.1 <i>Theoretical background</i>	31

2.11.2	<i>Instrumental information</i>	32
2.12	MICROSCOPY	32
2.12.1	<i>Atomic Force Microscopy (AFM)</i>	32
2.12.2	<i>Scanning Electron Microscopy (SEM)</i>	32
3.	MATERIAL AND EXPERIMENT	34
3.1	MATERIAL.....	34
3.2	SYNTHESIS OF THE BUILDING BLOCKS FOR NITROXIDE EXCHANGE REACTION.....	34
3.3	SYNTHESIS OF SELF-ASSEMBLED MONOLAYER FOR THE THIN-FILM PREPARATION	38
3.4	SYNTHESIS OF BUILDING BLOCKS FOR THIOL-YNE COUPLING THIN FILMS	39
3.5	SYNTHESIS OF DYNAMIC COVALENT POLYMER FRAMEWORK.....	40
3.6	SYNTHESIS OF THIOL-YNE COUPLING THIN FILM	48
3.7	INVESTIGATION OF SIDE GROUP EFFECT FROM ALKOXYAMINE VIA EPR SPECTROSCOPY	49
3.8	SYNTHESIS OF CROSSLINKED POLYSTYRENE VIA NITROXIDE EXCHANGE REACTION	51
4.	RESULT	53
4.1	OPTIMIZATION OF THE REACTION CONDITION FOR THE SYNTHESIS OF ORGANIC FRAMEWORK VIA NITROXIDE EXCHANGE REACTION	54
4.2	SYNTHESIS OF STIMULI RESPONSIVE SELF-HEALABLE ORGANIC FRAMEWORK	57
4.3	SYNTHESIS OF POROUS ORGANIC FRAMEWORK WITH TUNABLE POROSITY.....	69
4.4	SYNTHESIS OF CROSSLINKED POLYSTYRENE VIA NITROXIDE EXCHANGE REACTION	91
4.5	SIDE GROUP EFFECT INVESTIGATION OF ALKOXYAMINE VIA EPR SPECTROSCOPY.....	99
4.6	SYNTHESIS OF NITROXIDE EXCHANGE ORGANIC FRAMEWORK ON GOLD SURFACE	103
4.7	SYNTHESIS OF FREESTANDING THIOL-YNE COUPLING THIN FILMS.....	107
5.	CONCLUSION AND OUTLOOK	110
6.	ABBREVIATION	113
7.	REFERENCES	118
8.	ATTACHMENT	125
8.1	CV.....	125
8.2	PUBLICATIONS	126
8.3	CONFERENCE CONTRIBUTIONS AS ORAL PRESENTATIONS	127
8.4	CONFERENCE CONTRIBUTIONS AS POSTER PRESENTATIONS.....	127
9.	ACKNOWLEDGMENT	129

1. Introduction

1.1 Dynamic covalent materials

Dynamic covalent materials are materials constructed by covalent bonds, which can undergo reversible formation and cleavage under external influences.^[1] The main feature of the dynamic covalent chemistry is the dynamically controlled product distribution at the equilibrium.^[2] In case of reversible reactions, molecular components are allowed to cleave and recombine to achieve the thermodynamic minimum of the system at equilibrium.^[3]



Scheme 1: Free energy profile of kinetically ($A \rightarrow C$) as well as thermodynamically ($A \rightarrow B$) controlled reaction.

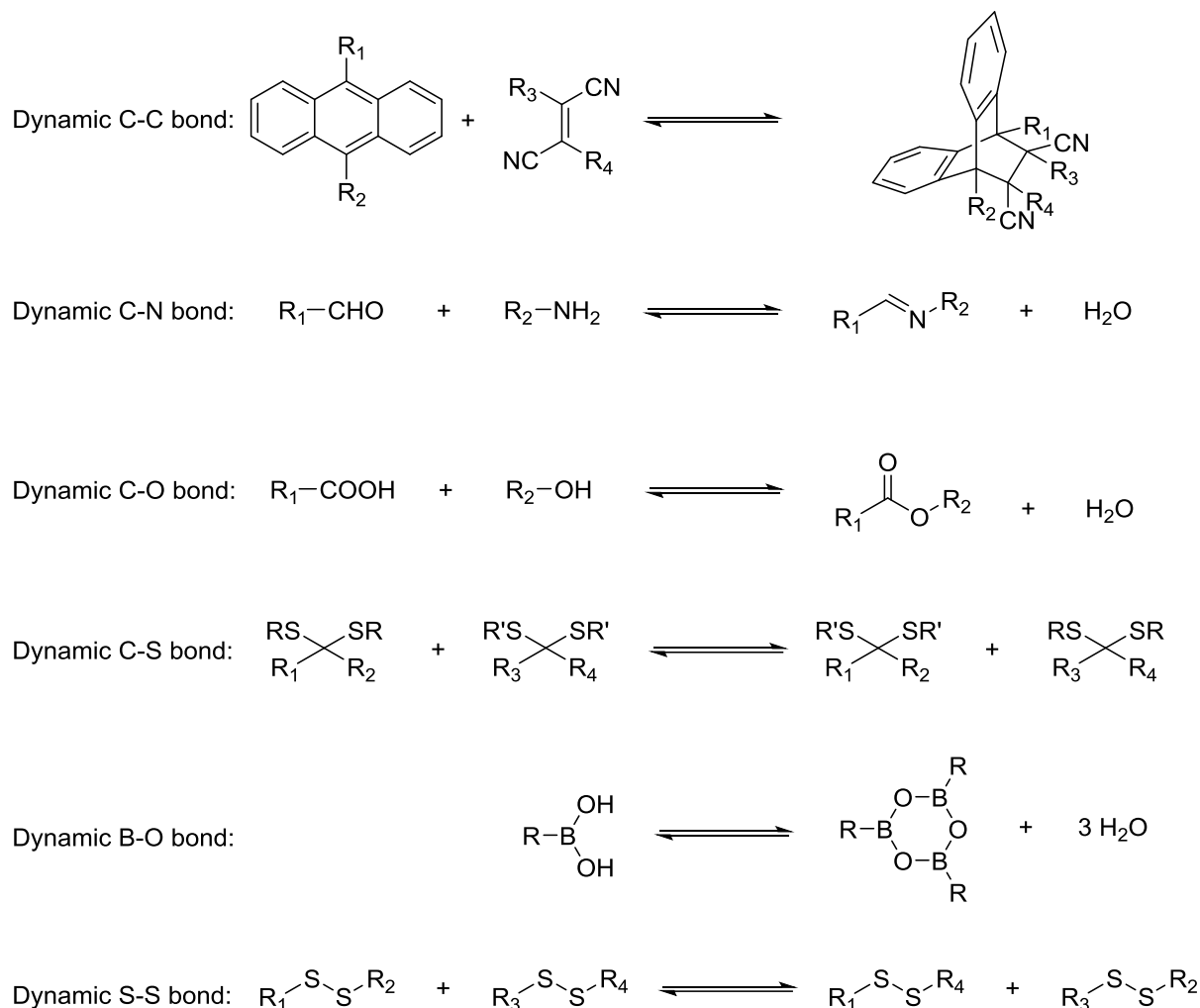
In Scheme 1, the schematic illustration of the kinetically as well as the thermodynamically controlled reaction is shown. During a dynamic covalent reaction, the starting material A reacts to a mixture of thermodynamically controlled product B and kinetically controlled product C. On the basis of the reversible reaction, bond breakage and recombination lead to more B instead of C due to the higher stability of B.^[4] Having this feature, the product can undergo “error-checking” or “proof-reading” to remove the thermodynamically unstable product.^[3]

There are two types of dynamic covalent reactions:

- (i) Reactions with reaction partners which result in the formation of the identical type of bonding.^[5]
- (ii) Formation of a new dynamic covalent bond.

Covalent bonds with reversible nature are: C-C bond, C-N bond, C-O bond, C-S bond, S-S bond and B-O bond. One of the famous reversible C-C bond reactions is the Diels-Alder reaction^[6], which involves a [4+2] pericyclic reaction. Alkyne^[7] and olefin^[8] metathesis belong as well to the dynamic C-C bond reactions.

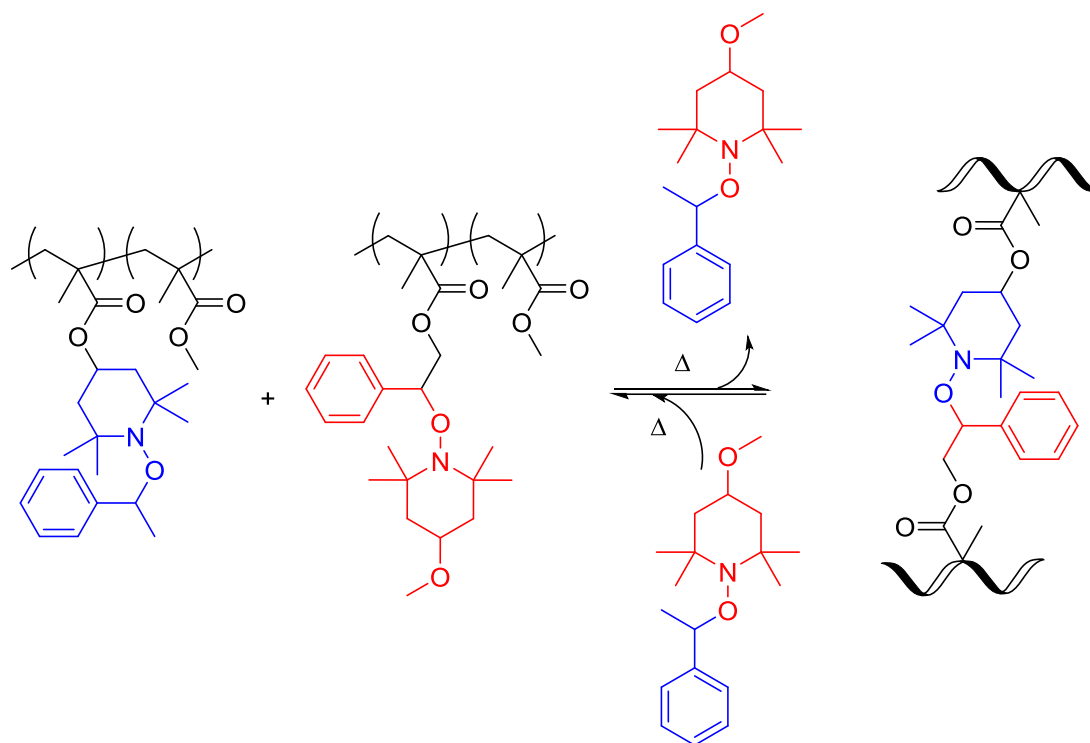
In case of covalent C-N bond, imines can be reversibly formed either through condensation, exchange or metathesis.^[9] Similar to previous mentioned reactions, esters and acetals can be synthesized in a completely reversible fashion by condensation or exchange reactions.^[10] Sulfur containing molecules with C-S or S-S bonds can be synthesized via reversible exchange reaction.^[10,11] Some of the covalent bonds are unsymmetrical and need the combination of two different components, e.g. condensation reaction of aldehydes and amines to imine bonds.^[9] On the other hand, symmetrical alkynes and olefins allow self-exchange. Example of different dynamic covalent reaction are listed in Scheme 2.



Scheme 2: Examples of different dynamic covalent reactions with C-C, C-N, C-O, C-S, B-O and S-S bond.

Among those different dynamic covalent reactions, nitroxide exchange is one of the few reactions based on the radical exchange process.^[12] At elevated temperature, the C-O bond of the alkoxyamine cleaves to a persistent nitroxide radical and a transient C-centered radical. This procedure is fully reversible, because both the moieties can easily recombine again^[13] In presence of an additional alkoxyamine, the cleaved nitroxides and transient C-centered radicals can exchange with each other to two new alkoxyamines. It is mainly applied in the synthesis of dynamically crosslinked polymers.^[14] Those crosslinked polymers are made of polymer chains with alkoxyamine moieties either on the main

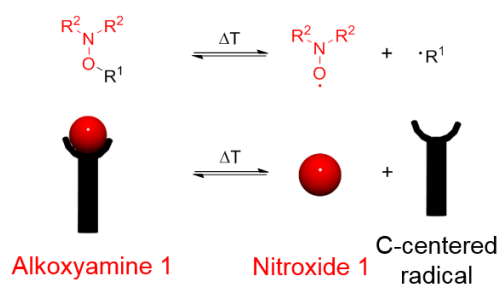
or side chain. Otsuka *et al.*^[15] explored the alkoxyamine exchange reaction between two types of alkoxyamine moieties. Those alkoxyamine moieties were incorporated into the polymer side chain, resulting in two different block copolymers. The exchange reaction is caused by heating and can be de-crosslinked under stoichiometric control (Scheme 3).



Scheme 3: Thermodynamic formation of crosslinked polymer via nitroxide exchange reaction.

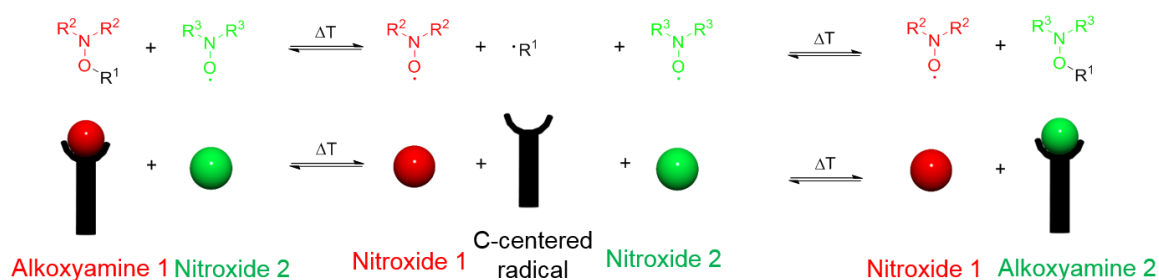
1.2 Nitroxide Exchange Reaction

The nitroxide exchange reaction is based on the reaction of an alkoxyamine and a nitroxide. Like already mentioned before, the C-O bond of the alkoxyamine cleaves reversibly to a persistent nitroxide radical and a transient C-centered radical. (Scheme 4). At elevated temperature, one transient C-centered radical and two types of nitroxides are in the intermediate state. In this case, both nitroxide moieties can react with the C-centered radical in a competitive fashion and form a mixture of two alkoxyamines and two nitroxides. The C-O bonding energy can vary significantly depending on the nitroxide bonded to the C-centered radical. This means, alkoxyamine with low C-O bonding energy are weaker and less stable, while alkoxyamines with higher C-O bonding energies are stronger bond and more stable. Therefore, after reaching the equilibrium, the thermodynamically favored product will be obtained. (Scheme 5)



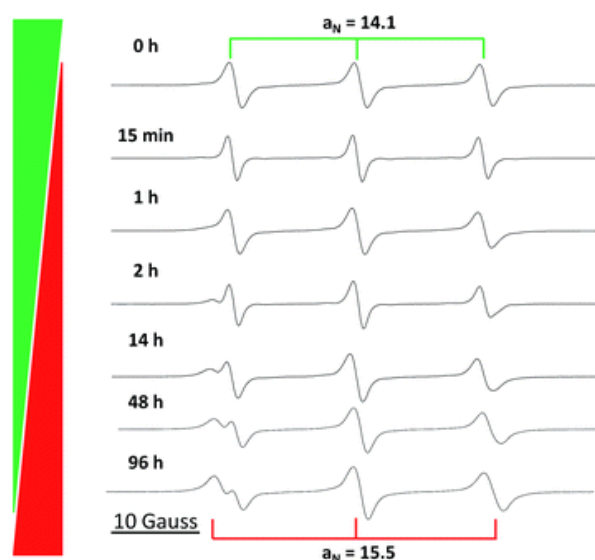
Scheme 4: Reversible cleavage of alkoxyamine to persistent nitroxide and transient C-centered radical.

Since nitroxides are paramagnetic compounds, electron paramagnetic resonance (abbreviated as EPR) spectroscopy was used to characterize those compounds. In 2016, Wessely *et al.* investigated the four-fold exchange reaction between TEMPO-alkoxyamine and tetraphenylmethane nitroxide (abbreviated as TPM-NO) using EPR spectroscopy. As different nitroxides have different hyperfine coupling constant, EPR spectroscopy was revealed to be a versatile tool to follow the exchange progress during the reaction.^[16] (Scheme 6)



Scheme 5: Mechanism of the Nitroxide Exchange reaction.

Furthermore, nitroxide which are tethered on fluorophores have been observed to form a “encounter complex”, that induces the fluorescence quenching.^[17] This is due to the interaction of the unpaired spin of the nitroxide with the electronic system of the fluorophore moiety.^[18] The interaction leads to an apparent change in multiplicity of the “encounter complex” from singlet to doublet state. After an excitation, the “encounter complex” is in one of the instable excited doublet states. Within the excited state, the electrons between the nitroxide and the highest fluorophore level can exchange. This process causes an intersystem crossing of the fluorophore, while the multiplicity of the “encounter complex” remains. From this excited state, usually the relaxation to the ground state occurs via a non-radiative process. The quenching effect is inhibited if the nitroxide is reacted to other forms, e.g. respective alkoxyamine derivatives.^[19]

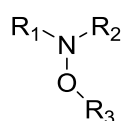


Scheme 6: EPR spectra of nitroxide exchange reaction between TEMPO-alkoxyamine and TPM-NO before heating and after heating at 80°C for 15 min, 1 h, 2 h, 14 h, 48 h, 96 h. green: TPM-NO; red: TEMPO. [I. Wessely, V. Mugnaini, A. Bihlmeier, G. Jeschke, S. Bräse and M. Tsotsalas, RSC Adv., 2016, 6, 55715 Radical exchange reaction of multi-spin isoindoline nitroxides followed by EPR spectroscopy] - Published by The Royal Society of Chemistry.^[16]

The nitroxide exchange reaction has been successfully applied for synthesis and tailoring of polymers. Turro *et al.* reported in 2000 the end functionalization of monodisperse styrene chains with photo- and bioactive molecules using nitroxide exchange reaction.^[14] Schulte *et al.* demonstrated in 2010 the functionalization of dye-loaded Zeolith L crystals with alkoxyamine and nitroxide and their controlled alternating assembly.^[20]

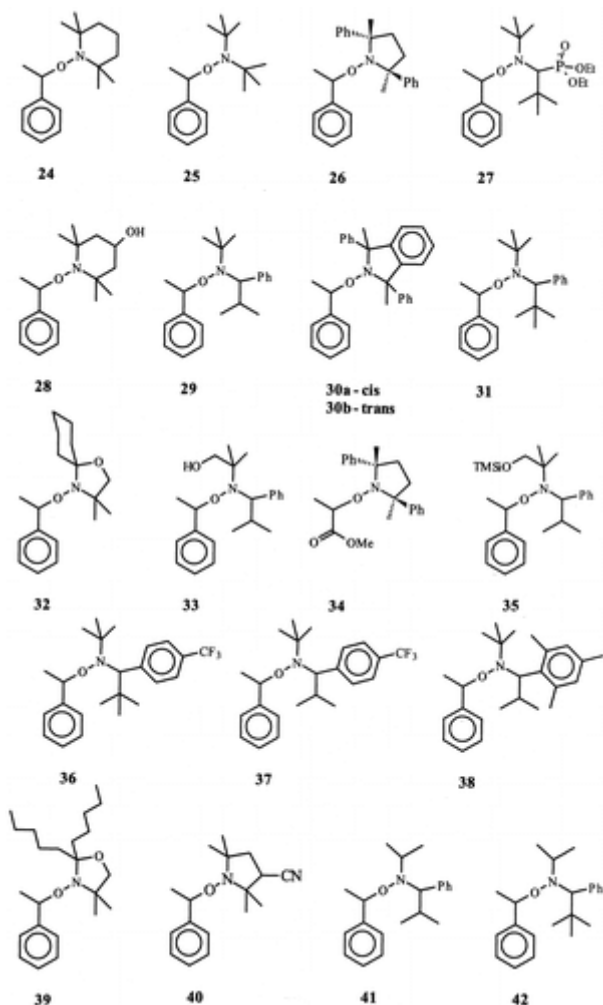
1.2.1 Alkoxyamines

Alkoxyamines, also called O-Alkyl hydroxylamines are derived from disubstituted (R_1 ; $R_2 \neq O$) hydroxylamines (Scheme 7).



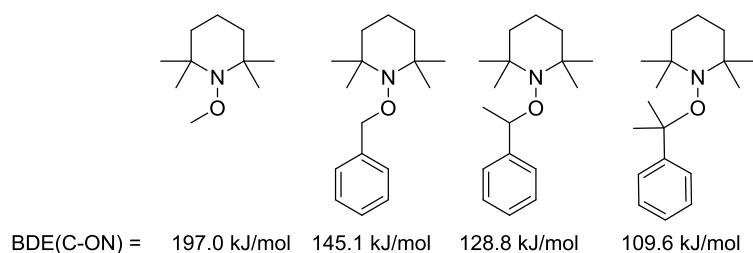
Scheme 7: Basic structure of an alkoxyamine.

As described before, the C-O bond of the alkoxyamine is weak towards thermal homolysis at elevated temperature. In 1985, Solomon *et al.*^[21] registered a patent for usage of different alkoxyamines as initiator of living radical polymerization. In Scheme 8, a library of alkoxyamine structure are shown, which are used to polymerize styrene and n-butyl acrylate via nitroxide mediated polymerization (abbreviated as NMP). Alkoxyamines can be synthesized with different methods. One method is using Grignard-reagent and TEMPO follow the route of Hawker and coworker.^[22] Another method is using the copper catalyzed reaction which reported by Matyjaszewski *et al.*^[23] in 1998.



Scheme 8: Library of alkoxyamine structures evaluated as initiators for the living free radical polymerization of styrene and *n*-butyl acrylate. [D. Benoit, V. Chaplinski, R. Braslau and C. J. Hawker, *J. Am. Chem. Soc.*, 1999, 121 (16), pp 3904–3920 Development of a Universal Alkoxyamine for “Living” Free Radical Polymerizations] – Published by Journal Of The American Chemical Society.^[24]

A very important property of alkoxyamines is the low bond dissociation energy (abbreviated as BDE) of the C-ON bond. This C-ON BDE depends on several factors, such as the steric demand around the C-O bond, polarity as well as the stability of the radical formed.^[25] For example in case of methyl-TEMPO, benzyl-TEMPO, (1-phenylethyl)TEMPO and cumyl-TEMPO, only the side group is changed (Scheme 9), leads to a significant change of the BDE. Most alkoxyamines are stable at room temperature, however in case of significant low BDE, the storage should be at lower temperatures for longer period of time.^[26]

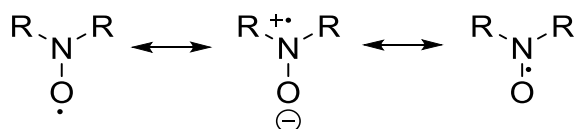


Scheme 9: BDE of Methyl-TEMPO, Benzyl-TEMPO, (1-phenylethyl)-TEMPO and Cumyl-TEMPO.

1.2.2 Nitroxides

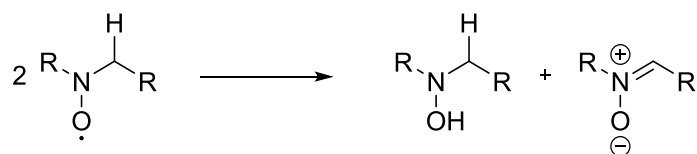
Nitroxides are compounds containing $R_2N-O\cdot$ functional groups. According to IUPAC, this type of compound should not be called as nitroxides but as aminoxyl radicals, as they erroneously suggest the presence of a nitro group.^[27] However, to be consistent with most of the references, this type of compound will be called nitroxide in this thesis.

Sterically hindered nitroxides such as (2,2,6,6-Tetramethylpiperidin-1-yl)oxyl (TEMPO) are persistent radicals with a delocalized electron between nitrogen and oxygen atom. (Scheme 10)



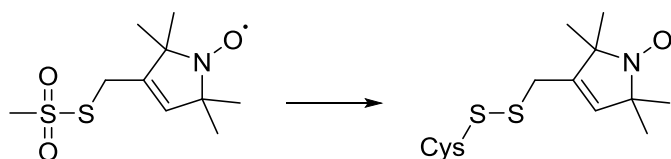
Scheme 10: Resonance structures of nitroxides. ^[28]

The alkyl-substituent on the nitrogen atom can be primary, secondary as well as tertiary. However, the nitroxide with primary and secondary substituents are in general less stable and inclined to decompose to hydroxylamine and nitron. (Scheme 11)



Scheme 11: Disproportionation of nitroxide with secondary alkyl-substituents.

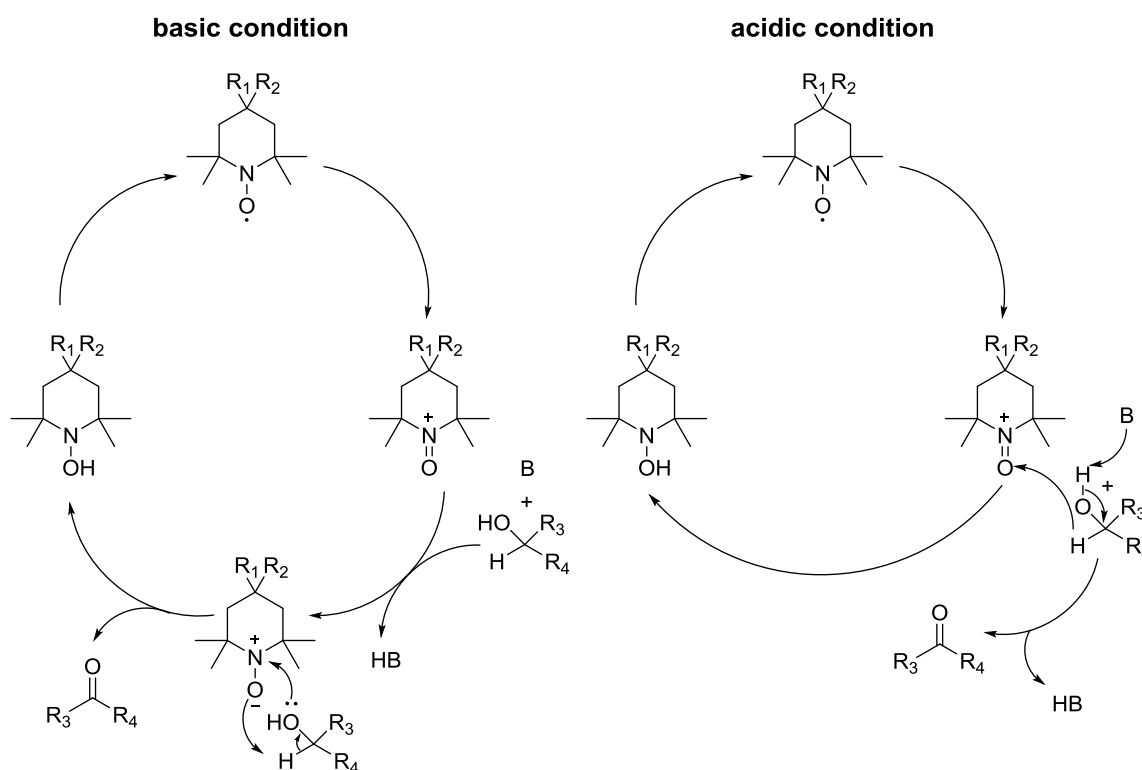
Nitroxides have a wide range of applications. One of the application is spin-label for biological macromolecules.^[29] The structural investigation of many biological macromolecules are of great interest, as insight into their structure allows to gain a better understanding on their function.



Scheme 12: Chemical structure of the spin label reagent ((1-Oxyl-2,2,5,5-tetramethylpyrroline-3-methyl) methanethiosulfonate) MTSSL and the disulfide bond adduct formed with a single cysteine.^[30]

Attachment of nitroxides via disulfide reaction is one of the most commonly used spin-label systems on proteins. The conjugation of MTSSL on a single cysteine is shown in Scheme 12.^[30] With the spin-label on a certain position, the biomacromolecules can be investigated with paramagnetic relaxation enhancement, an NMR technique. The introduced nitroxide causes an enhanced relaxation of the spins near the paramagnetic spin label, resulting in long range distance information.^[31]

The nitroxide can also be used for magnetic resonance imaging^[32] Paramagnetic metals e.g. gadolinium (Gd) chelate complexes are commonly used as positive contrast agent in magnetic resonance imaging by locally reducing the water ¹H longitudinal relaxation time (spin lattice T₁). However, due to the established toxicity in some patient population, the development of less toxic and metal-free imaging agent is of rising interest. H. V. Nguyen *et al.* developed in 2017 a nitroxide-based macromolecular MRI imaging agent. The macromolecule consists of a dense layer of nitroxide at the interface between a rigid poly(acetal) core and a hydrophilic PEG shell.^[33]



Scheme 13: Catalytic cycle of nitroxide radicals for oxidation of alcohols.^[34,35]

Nitroxides are further widely used as co-oxidation reagent for oxidation of alcohols. There are two ways to apply nitroxides for the oxidation of alcohols. The first way is the separate synthesis of an oxoammonium salt. However, due to its high reactivity, it is difficult to isolate. The second way is the oxidation of the radical *in situ*, which allows a catalytic cycle. The disproportionation of nitroxide radicals forms the oxidizing oxoammonium salt. The reaction is acid catalyzed by a pH below 2. After the usage of the catalytic amount of nitroxide radicals, it must be regenerated from the hydroxylamine in a one-electron reaction by a primary oxidant. Above pH of 3, rapid syn proportionation between the oxoammonium salt and the hydroxylamine proceeds to generate two nitroxide radicals.^[34,35] (Scheme 13)

As mentioned before, alkoxyamines are used as initiator for living radical polymerization. At elevated temperature, the cleavage of the alkoxyamine to a persistent nitroxide and a C-centered radical occurs, resulting in the polymerization of e.g. styrene with the C-centered radical. During the polymerization, the nitroxide reversibly scavenges the growing chain-end, thereby lowering the overall radical concentration at any given time. In this way, the probability of chain-termination via recombination is reduced and a controlled chain-growth is eased.^[36]

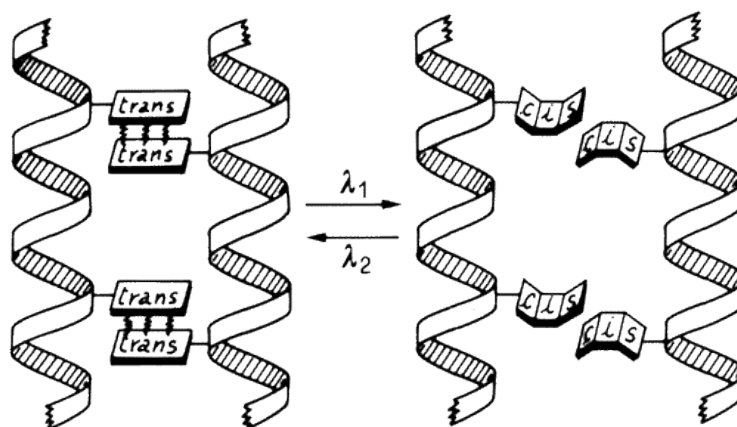
1.3 Stimuli responsive materials

In the last two decades, the development of stimuli responsive materials is of great interest. These materials undergo physical or chemical changes due to an external stimulus, which is directly applied to the molecular architecture due to reorganization or rearrangement of bonds.^[37] Example of external stimuli are temperature^[38,39], pH^[40], electric fields^[41] or light^[38]. There are many biological processes involving nucleic acid, proteins and polypeptides that can adopt conformations specific to their surroundings. Similar behavior is also observed by synthetic (co)polymers that exhibit changes in character (e.g. charge, polarity and solvency) in response to an external stimuli.^[42]

Stimuli responsive materials can be divided into subclasses through their external stimuli.

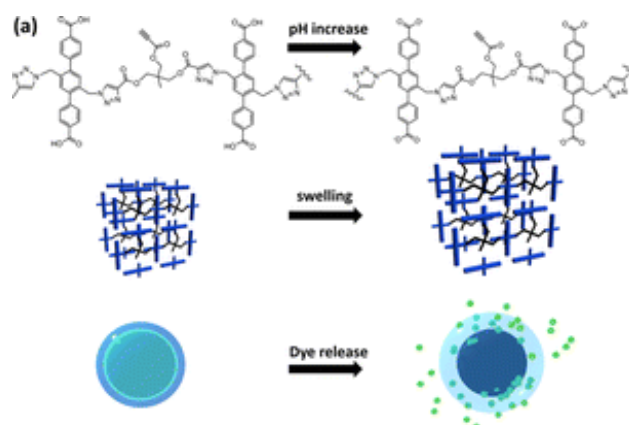
The most widely known subclass is the thermoresponsive materials. Recently, Appel *et al.* reported a thermo-sensitive supramolecular polymer hydrogel. The macrocyclic host molecule was used to facilitate the reversible crosslinking of multivalent copolymers containing either pendant methyl viologen units or naphthoxy moieties. While heating, the hydrogel undergoes a gel-sol transition, which can reform while cooling or adding the macrocyclic host molecule.^[43]

Another subclass of rising interest is photoresponsive materials. The photo-responsiveness is caused by photochromic molecules e.g. azobenzene derivatives, spiropyran compounds, diarylethenes, fulgides and triphenylmethane derivatives. Pieroni *et al.* discovered the reversible aggregation and disaggregation process of azo-modified polypeptide upon exposure to light or dark conditions.^[44] The schematic illustration is shown in Scheme 14.



Scheme 14: Schematic illustration of reversible aggregation and disaggregation among helical macromolecules with photoresponsive azobenzene units.^[45] [O. Pieroni, A. Fissi, N. Angelini, F. Lenci, *Acc. Chem. Res.*, 2001, 34, 1, 9–17. *Photoresponsive Polypeptides*] - Published by American Chemical Society

In case of chemoresponsive materials, any chemical that can weaken or break bonds will make the material be responsive to it. The easiest and the common way to implement the chemoresponsiveness of polymers is to change the solutions pH to break pH-sensitive bonds. Especially for medical purpose, pH-responsiveness enables the drug transport along certain pH environment and targeted release at another specific pH range. Schmitt *et al.* fabricated SURGEL capsules by growing SURMOF on magnetic nanoparticles, followed by crosslinking and EDTA treatment to remove the metal ions after dissolving the metal coordination used as a template (Scheme 15). As cargo molecule, dyes were loaded into the nano-capsules. Around pH 11, the SURGEL capsules started to swell and the dye molecules were slowly released by the capsules.^[46]



Scheme 15: pH triggered dye release from SURGEL capsules.^[46] [S. Schmitt, M. Silvestre, M. Tsotsalas, A. Winkler, A. Shahnas, S. Grosjean, F. Laye, H. Gliemann, J. Lahann, S. Bräse, M. Franzreb, C. Wöll, *ACS Nano*, 2015, 9, 4, 4219–4226. *Hierarchically Functionalized Magnetic Core/Multishell Particles and Their Postsynthetic Conversion to Polymer Capsules*] - Published by American Chemical Society

Besides previous mentioned subclasses, other stimuli e.g. mechano-responsiveness^[47] and electro-responsiveness^[41] are also of rising interest.

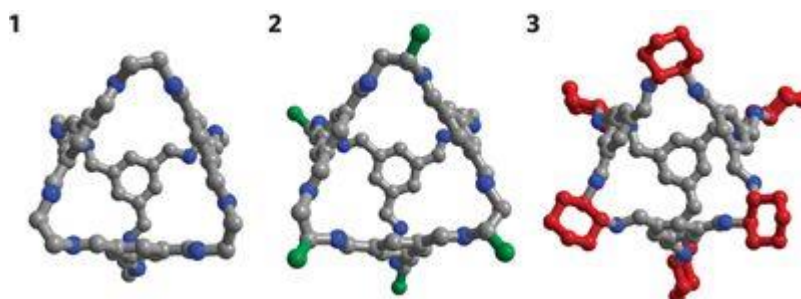
In recent years, many approaches have been investigated resulting in self-healing polymers.^[48] They can be classified in extrinsic and intrinsic self-healing polymers. In case of extrinsic self-healing polymers, healing agents are encapsulated inside the polymer.^[49] Damage to the polymer furthermore damages the capsuled resulting in the release of the healing agents. However, this approach is not repeatable in the same region, because of the exhaustion of the required healing agent. Besides the extrinsic self-healing polymers, intrinsic self-healing polymers have been intensively investigated in last decades. Unlike the extrinsic self-healing property, the intrinsic healing property is based on the presence of reversible building units and crosslinkers within the material. To trigger the healing process, heat is the most used method. Chen *et al.* developed the first thermally self-healable polymer based on [4+2] cycloaddition. By heating, retro Diels-Alder reaction occur, resulting in healing of cracks.^[50]

1.4 Porous organic materials

Porous organic materials are materials, which possess voids and consist of light weight elements. Due to the comprehensive area of applications such as catalysis^[51], energy storage^[52], gas separation^[53], proton conduction^[54], photocatalysis as well as photoluminescence^[55], porous organic materials emerged strongly in the past 10 years.

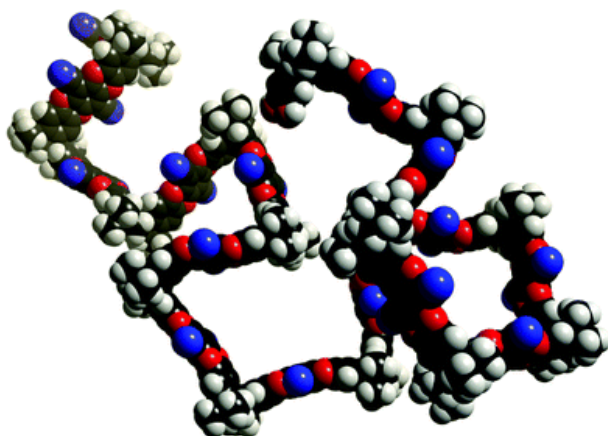
The porous organic materials may be categorized into two subclasses: non-framework compounds and framework compounds.

Porous organic cages can undoubtedly be assigned as non-framework compounds. Tozuwa *et al.* introduced the synthesis of porous organic cages via condensation reactions in 2009.^[56] (Scheme 16). The porosity of these materials is a consequence of both the molecular voids in the cages and the inefficient packing of the cages. The attachment of steric groups to the cages reveals to produce 1D channels between the cages.



Scheme 16: Tetrahedral imine-linked cage molecules synthesized by the [4 + 6] condensation of 1,3,5-triformylbenzene with three different vicinal diamines: 1,2-ethylenediamine (cage 1), 1,2-propylenediamine (cage 2) and (R,R)-1,2-diaminocyclohexane (cage 3). [T. Tozawa, J. T. A. Jones, S. I. Swamy, S. Jiang, D. J. Adams, S. Shakespeare, R. Clowes, D. Bradshaw, T. Hasell, S.Y. Chong, C. Tang, S. Thompson, J. Parker, A. Trewin, J. Bacsá, A. M. Z. Slawin, A. Steiner & A. I. Cooper, Nature Materials, 2009, 8, 973–978. Porous organic cages] - Published by Nature Materials.^[56]

Another material class which belongs non-framework compound as well as framework compound is the polymers of intrinsic microporosities (abbreviated as PIMs). PIMs are polymers with relatively rigid and “awkwardly shaped” backbones.^[57] This backbones resulting in inefficient packing in micropore range. In 2004, Budd *et al.* synthesized the first solution processable porous organic material, which formed from di-fold-catechol and fluorinated aromatics.^[58] The molecular model of PIM-1 is shown in Scheme 17.



Scheme 17: Molecular model of PIM-1, showing its rigid and contorted structure. [N. B. McKeown and P. M. Budd, Chem. Soc. Rev., 2006, 35, 675. Polymers of intrinsic microporosity (PIMs): organic materials for membrane separations, heterogeneous catalysis and hydrogen storage] - Published by Royal Society of Chemistry.^[57]

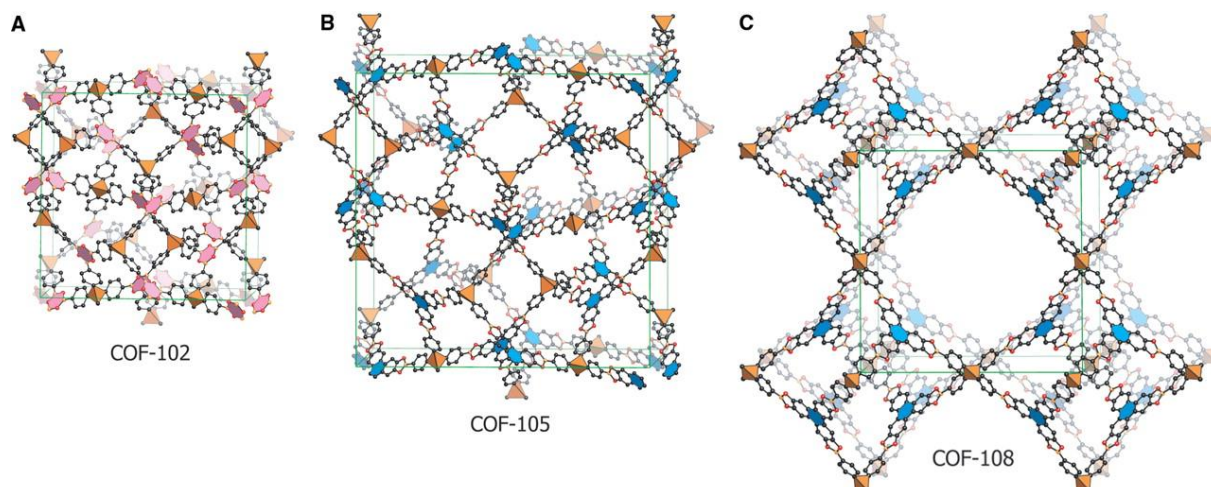
Beside the previous mentioned non-framework compound, porous framework compounds include crystalline covalent organic frameworks (COFs) and amorphous porous organic polymers (POPs). Due to the high permanent porosity as well as good chemical and thermal stability, this subclass experienced rapid development within the last decades.

As mentioned before, COFs are crystalline porous frameworks consisting of light-weight element building blocks linked via covalent bonds. The crystallinity of the COFs is ensured by a reversible polymerization reaction, which favors the formation of thermodynamically controlled polymers. Depending on the structure of the building blocks, COFs can be 2-dimensional (2D) or 3-dimensional (3D).

In 2005, Côte *et al.* presented the first 2D COF-1.^[59] The synthesis of the COF-1 is based on the condensation reaction of diboronic acid (BDDBA) molecules. Following the same procedure, COF-5 was synthesized from BDDBA and 2,3,6,7,10,11-hexahydroxytriphenylene (HHTP). In 2007, El-Kaderi *et al.* succeeded to synthesize 3D COF-102 using the rigid tetrahedral building block tetra(4-dihydroxyborylphenyl)methane (TBPM) which undergoes self-condensation.^[60]

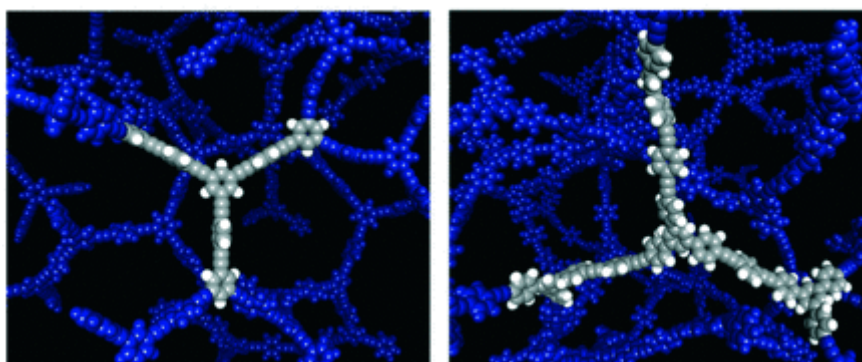
The COFs based on boroxine and boronic acid ester have high crystallinity, however the drawback is the lability in presence of water and protic solvents.^[61] The COFs based on imine-^[62], hydrazone-^[63],

triazine-^[64], phenazine-^[65] and azine^[66] bond have high stability, however they are less crystalline and less porous.



Scheme 18: Structure of COF-102, COF-105 and COF-108. Hydrogen atoms are omitted for clarity. Carbon (gray); Boron (orange spheres); Oxygen (red spheres). [H. M. El-Kaderi, J. R. Hunt, J. L. Mendoza-Cortés, A. P. Côte, R. E. Taylor, M. O’Keeffe, O. M. Yaghi, *Science*, 2007, 316 (5822), 268-272. *Designed Synthesis of 3D Covalent Organic Frameworks*] - Published by Science.^[60]

Distinct of the reversible reaction mechanism, POPs include CMPs, PAFs, HCPs are based on kinetically controlled irreversible reactions. In the past 10 years, researchers around the world reported a range of synthetic strategies to produce POPs, including Sonogashira-Hagihara cross-coupling reaction^[67], Gilch reaction^[68], alkyne-alkyne homocoupling^[69], Suzuki-Miyaura cross coupling^[70,71], Yamamoto reaction^[72] and oxidative thienyl coupling^[73,74]. In Scheme 19, the simulated network fragment of CMP-1 and CMP-3 by Jiang *et al.* are shown.



Scheme 19: Simulated network fragment of CMP-1 (left) and CMP-3 (right). [J. Jiang, F. Su, A. Trewin, C. D. Wood, N. L. Campbell, H. Niu, C. Dickinson, A. Y. Ganin, M. J. Rosseinsky, Y. Z. Khimyak, A. I. Cooper, *Angew. Chem. Int. Ed.*, 2007, 46, 8574-8578. *Conjugated Microporous Poly(aryleneethynylene) Networks*] - Published by Wiley-VCH.^[67]

The large π -system that is built upon the full conjugation of the polymers offers properties that are useful for electrical conductivity or in light harvesting^[71] applications, combining these with the porosity possible sensor devices are possible. However, the high rigidity and the low flexibility inhibit the processability of those materials.

In most of the cases, porous organic frameworks like CMPs or PIMs possess micropores as well as meso- or macro- pores. The micropores are usually intrinsic to the structure of the polymer scaffold or arises from the contorted shape and rigidity, which inhibits efficient packing of the macromolecules in solid state.^[67,73] Also, it is likely, that catenation and entanglement of the fragments in the polymer resulting in even more micropores.^[67] In contrast, meso- and macropores arise through the packing of the macromolecule's particles, which can be verified with scanning electron microscope.

The development of different types of porous organic materials occurs nearly simultaneously within the last two decades and so far, no official standard nomenclature was issued by IUPAC. Therefore, the definitions within this field are vague.

2. Methods

In this chapter, the techniques which are used for the characterization of the organic frameworks are introduced with theoretical background. Information about the instrumentation as well as specific measurement processes are also described. The relevant techniques include Electron Paramagnetic Resonance (EPR) Spectroscopy, Gas Adsorption, Fluorescence Spectroscopy, Fourier Transform Infrared (FTIR) Spectroscopy, X-ray Diffraction (XRD), Electrospray Ionization Mass Spectrometry (ESI-MS), Fast Atom Bombardment Mass spectrometry (FAB-MS), Gel Permeation Chromatography (GPC), Nuclear Magnetic Resonance (NMR) Spectroscopy, Thermogravimetric analysis (TGA), Differential Scanning Calorimetry (DSC), Spectroscopic Ellipsometry (SE), Atomic Force Microscopy (AFM), Time-of-Flight Secondary Ion Mass Spectrometry (ToF-SIMS) and Scanning Electron Microscopy (SEM).

2.1 Electron paramagnetic resonance (EPR)

2.1.1 Theoretical background

Electron paramagnetic resonance (EPR) or electron spin resonance (ESR) spectroscopy is a method for investigating paramagnetic materials, i.e. substances having a magnetic susceptibility $\chi > 0$.^[75] Unpaired electrons are responsible for the existence of paramagnetism in most substances. Every electron possesses a magnetic moment and spin quantum number of $s = \frac{1}{2}$, with magnetic components $m_s = +\frac{1}{2}$ and $m_s = -\frac{1}{2}$. With an external magnetic field B_0 , the magnetic moment of the electrons align itself parallel ($m_s = +\frac{1}{2}$) or antiparallel ($m_s = -\frac{1}{2}$) to the field. Due to the Zeeman effect, each alignment has a specific energy E .

$$E = m_s g_e \mu_B B_0 \quad (1)$$

Where, g_e is so-called g-factor of an electron. In case of an unbound "free" electron, the g factor is given by $g_e = 2.002319$. μ_B is the Bohr magneton.

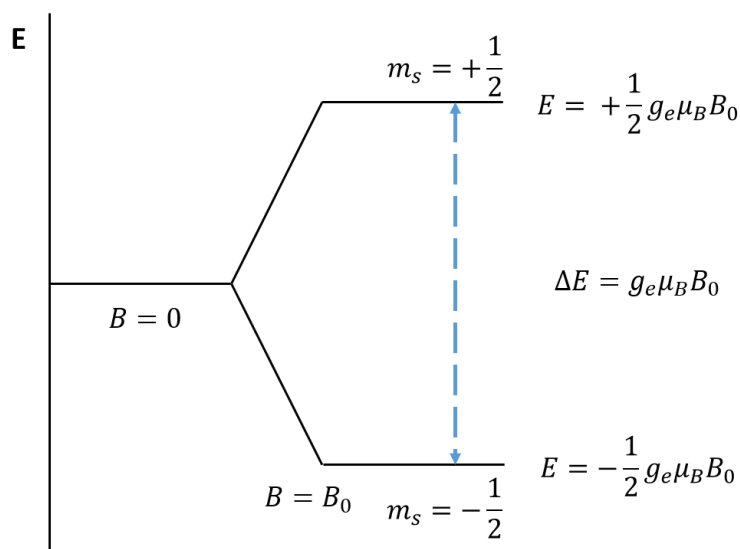
The splitting energy for unpaired free electron between lower and upper state is calculated with equation (2):

$$\Delta E = g_e \mu_B B_0 \quad (2)$$

According to the Planck's law, electromagnetic radiation will be absorbed if:

$$\Delta E = h\nu \quad (3)$$

Where h is Planck's constant and ν is the frequency of the radiation. By absorbing or emitting a photon of energy $h\nu$, an unpaired electron can move between the lower and upper state. By combining these two equations one obtains the fundamental equation of techniques based on magnetic resonance.



Scheme 20: Spin state energies as function of the magnetic field B_0 .

For unpaired electrons in free radical, the g value is modified by the spin-orbit interaction, which leads to a shift of g from g_e . This is comparable with the chemical shift in NMR spectroscopy and can provide information on the binding situation of the unpaired electron. Organic free radicals, with only H, O, C and N atoms create a small shift of g_e to g , because the spin orbit coupling contribution depends on the size of the nucleus containing the unpaired electron. Therefore, the shift of g_e to g from transition metals are significant.

Due to the fact, that Bohr's magneton μ_B and Planck's constant are known, the only values needed to determine are ν and B_0 . B_0 is the magnitude of the magnet in the EPR and ν is the radiation frequency used during the measurement. Therefore, using the equation (4), the g -factor can be calculated.

$$g = \frac{h\nu}{\mu_B B_0} \quad (4)$$

Another important factor in the EPR is the hyperfine interaction. The nuclei of atoms in a molecule usually have their own magnetic moment which can produce a local magnetic field to interact with the electron. This interaction is called hyperfine interaction. The energy of the electron applied by the magnetic field B_0 can be expressed then as:

$$E = m_s g \mu_B B_0 + a m_s m_I \quad (5)$$

Where a is the hyperfine couplings constant and m_i is the nuclear spin quantum number. The hyperfine interactions provide information about the number and identity of atoms in a compound and the distance from the unpaired electron. The rule for determine the hyperfine pattern is analogous to NMR. The number of lines from the hyperfine pattern can be calculated using the equation (6):

$$2NI + 1 \quad (6)$$

Where N is the number of equivalent nuclei and I is the nuclear spin. In case of the nitroxide radical 2,2,6,6-tetramethyl-1-piperidinyloxy (TEMPO), the number of equivalent nuclei is 1 and the number of spins is also 1. Because ^{16}O has a nuclear spin of 0, only ^{14}N contributes to the multiplicity. Therefore, the nitroxide radical TEMPO has three lines of equivalent intensity.

The major techniques used for EPR spectroscopy are continuous wave (CW) and pulsed EPR. The CW spectra are recorded by irradiating the sample with microwave of constant frequency ν and sweeping the external magnetic field B_0 until the resonance condition is fulfilled.

2.1.2 Instrumental information

Electron paramagnetic resonance (EPR) spectroscopy was performed on a Bruker EMXNano spectrometer. If not otherwise noted, all sample are measured in toluene at room temperature (23 °C). The following parameters were used for the measurement: Centre field: 3434 G; sweep width: 100 G; sweep time: 180 s; sample g-factor: 2.00; receiver gain: 40 dB; modulation amplitude: 0.452 G; number of scans: 1; microwave attenuation: 60 dB; number of points: 2212; modulation frequency: 100 kHz, modulation phase: 0; conversion time: 81.38 ms; time constant: 1.28 ms; points/modulation amplitude: 10.

2.2 Gas adsorption

2.2.1 Theoretical background

Gas adsorption is a well-established method to investigate the texture of a porous solids and powders. The adsorption is defined as the concentration of molecules or atoms in the vicinity of an interface. In case of gas/solid systems, the adsorption is proceeding on the solid surface and outside of the solid structure. The material/gas adsorbed on the surface are usually called adsorbate, while the material which take the adsorbate is called adsorbent. The adsorption can be physisorption or chemisorption. In the chemisorption, the adsorbate is in contact with the adsorbent and the chemical bonds are formed by intermolecular forces. In the case of physisorption, the fundamental intermolecular interactions are caused by the van der Waals force. Basically, all gases can be adsorbed by all material under their critical temperature. However, nitrogen, argon and krypton are the conventional gases

used for the determination of the porosity of a material. The inverse process of adsorption is desorption.

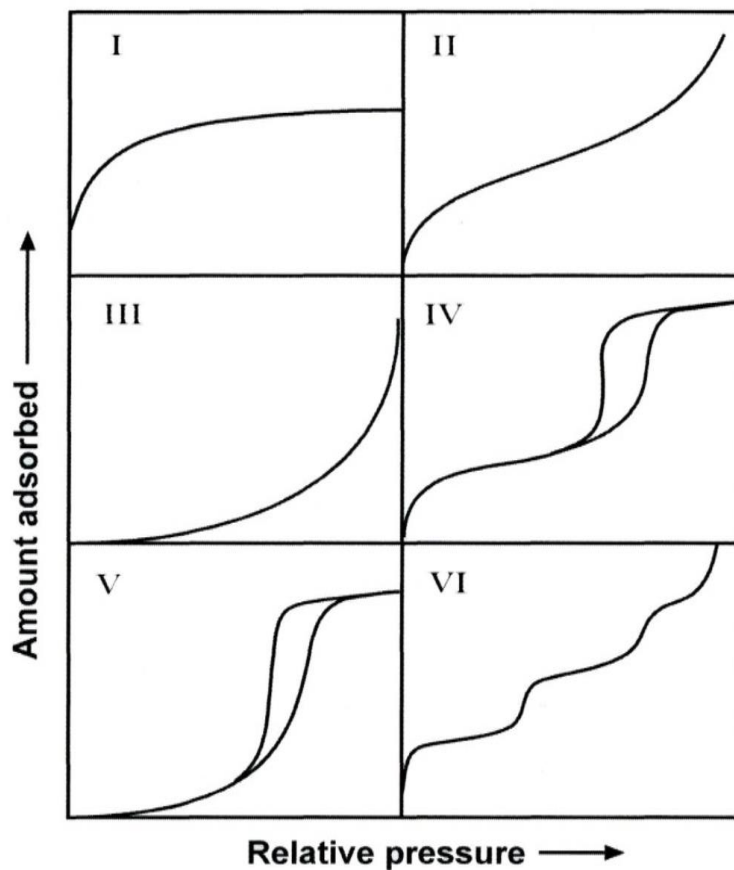
To determine the surface area, solid materials are pretreated by applying heat, vacuum or flowing gas to remove adsorbed contaminations such as water and carbon dioxide from atmospheric exposure. The material is then cooled under vacuum to 77 K or 87 K. The adsorbate, which can be nitrogen or argon is then dosed to the material in controlled increments at constant temperature. The pressure is allowed to equilibrate after each dose of gas and the amount of adsorbate is calculated. The amount of adsorbate at each pressure defines an adsorption isotherm.

The physisorption isotherms is classified in six major types.^[76]

Type I isotherms are given by microporous materials with small external surface. In this case, the uptake of the adsorbate is mostly taking place at very low P/P_0 resulting in micropore filling. Type I(a) isotherms are given by microporous materials with pore width under 1 nm. Whereby type I(b) are mostly given by materials with a slightly broader pore size distribution which also include narrow mesopores up to 2.5 nm. Type II isotherms are given by nonporous or macroporous adsorbents with an unrestricted monolayer-multilayer adsorption up to high P/P_0 . Point B (Scheme 21) usually corresponds to the implementation of the monolayer coverage.^[76]

In case of type III isotherm, the Point B doesn't exist anymore, which signifies no monolayer formation. This isotherm describes also nonporous or macroporous solid, where adsorbent and adsorbate interactions are comparative weak. The type IV isotherms are usually given by mesoporous materials. At lower P/P_0 , the monolayer-multilayer coverage taking place followed by pore condensation at higher P/P_0 . The type IV is also divided in type IV(a) and IV(b). In type IV(a), the pore condensation is accompanied with hysteresis, because the pore width exceeds than ~ 4 nm.^[77] By mesoporous material with smaller pore width, the type IV(b) are observed. The type V isotherm is comparatively like type III, except that molecular clustering is followed by pore filling at higher P/P_0 . The type VI isotherm are given by a layer-by-layer stepwise adsorption on a highly uniform nonporous surface. Each step represents an adsorbed layer, while temperature can affect the sharpness of the steps.

According to IUPAC recommendation, pores are classified in three types. (i) Macropores, with pore widths over 50 nm. (ii) Mesopores, with pore widths between 2 nm and 50 nm. (iii) Micropores, with pore widths under 2 nm.^[78]



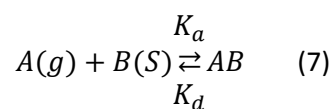
Scheme 21: Classification of physisorption isotherms. [Z.A. ALOthmann, *Materials*, 2012, 5 (12), 2874-2902. A review: *Fundamental Aspects of Silicate Mesoporous Materials*] - Published by MDPI AG under the CC BY-NC-SA 3.0 license.^[79]

To analyze experimental results of physisorption, over 15 different isotherm models were developed until today. This includes, the Langmuir-isotherm model and the BET-isotherm model.

Langmuir-isotherm model was developed by Irving Langmuir in 1916.^[80] This model explains the variation of adsorption with pressure. With his theory, a relationship between the number of active sites on the adsorbent that undergo adsorption and pressure was depicted.

The basic assumptions of this model are:

- 1) The adsorbent surface is perfectly flat and contains a fix number of adsorption site. Therefore, all places on the adsorbents are energetically homogenous.
- 2) Each adsorption site can hold maximum one gas molecule and the released energy during this process is constant.
- 3) There is a dynamic equilibrium between adsorbed gas molecule (AB) and the free gas molecule (A(g)). B(S) is the unoccupied adsorbent surface.



- 4) The adsorption is either a monolayer or an unilayer.

According to the kinetic theory, the adsorption equilibrium constant is depicted as K_a and the desorption equilibrium constant as K_d . At equilibrium, the adsorption rate is equal to the desorption rate.

$$K_a[A][B] = K_d[AB] \quad (8)$$

$$K = \frac{K_a}{K_d} \quad (9)$$

With the θ as occupancy for the adsorbate on the adsorbent, the unoccupied fraction of the adsorbent can be calculated as $(1-\theta)$. The adsorption rate depends on the number of free sites on the adsorbent as well as pressure P and the desorption rate depends only on the occupancy on the adsorbents. Therefore, the equation (10) can be written as:

$$K_a P(1 - \theta) = K_d \theta \quad (10)$$

The occupancy on the adsorbent θ can be solved with equation (11):

$$\theta = \frac{K_a P}{K_d + K_a P} \quad (11)$$

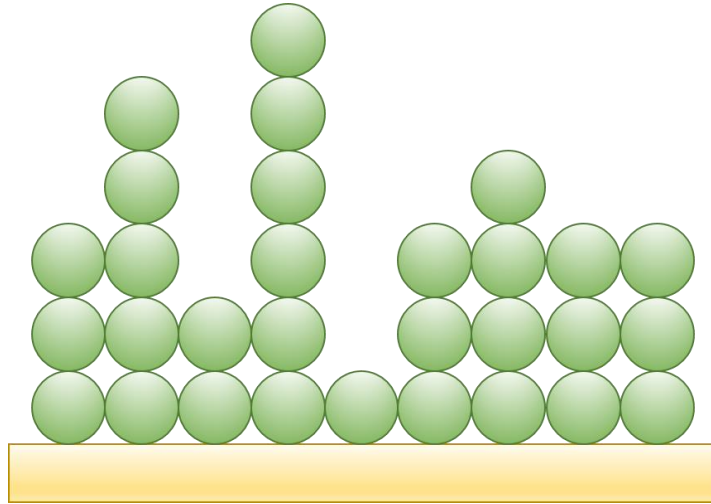
With the equation (12), the above equation (11) can be simplified in:

$$\theta = \frac{KP}{1+KP} \quad (12)$$

This is also known as the Langmuir adsorption equation.

However, the Langmuir model is only valid at low pressure condition. In the real condition, the adsorbed gas cannot behave ideally and interaction between the molecules are inevitable. Also, the surface of the adsorbent is anything but perfectly homogenous. Only at low pressure condition, the monolayer formation is possible, but at high pressure condition, the gas molecules start to interact with each other. Another model also includes the explanation that is needed for the multilayer adsorption process. This model is BET, invented by Brunauer, Emmett and Teller in 1938.^[81]

In the BET model, gas molecules physically adsorb on an adsorbent infinitely. And the molecules only interact with the bordering layer.



Scheme 22: Schematic illustration of multilayer adsorption with random distribution of the occupancy.

The BET equation is expressed by (13)

$$\frac{P/P_0}{n(1-P/P_0)} = \frac{1}{n_m C} + \frac{C-1}{n_m C} (P/P_0) \quad (13)$$

Where n is the adsorbed gas quantity at relative pressure P/P_0 and n_m is the specific monolayer capacity. C is the BET constant, which expressed by equation (14)

$$C = \exp\left(\frac{E_1 - E_V}{RT}\right) \quad (14)$$

E_1 is the enthalpy of desorption for the first monolayer, E_V is the enthalpy of vaporization of the adsorbate. The difference in energy between the various enthalpies governs the shape of the later isotherm. For values $C \ll 1$ the enthalpy of desorption for the first monolayer is smaller than the enthalpy of vaporization, resulting in low relative adsorption up to high pressures. In case the heat of desorption for the first layer is larger than the enthalpy of vaporization, high relative adsorption is observed at low pressures.

Brunauer, Emmett and Teller used two assumptions to simplify their model. The reason is to separate the various layers into two categories: the first layer that interacts with the substrate as well as higher layers that only interact with other adsorbates. They assumed that the enthalpy of desorption for all higher layers is the same as the enthalpy of vaporization of the adsorbate ($E_2 = E_3 = E_4 = \dots = E_i = E_V$). Further they assumed an equilibrium between adsorption and desorption for all higher layers.

The BET equation can be plotted as a straight line with $1/n[(P_0/P)-1]$ on the y-axis and P/P_0 on the x-axis. This plot is called a BET plot. The plot should be in the range of $0.05 < P/P_0 < 0.30$. With this plot, the slope A and the y-intercept I can be determined, which can be used for calculating the specific monolayer capacity n_m and the BET constant C .

$$n_m = \frac{1}{A+I} \quad (15)$$

$$C = 1 + \frac{A}{I} \quad (16)$$

The specific surface area S_{BET} can be calculated using the equation (17).

$$S_{BET} = \frac{n_m \cdot N_A \cdot s \cdot a}{V} \quad (17)$$

Where N_A is Avogadro's number, s is the adsorption cross section of the adsorbing species, V the molar volume of the adsorbate and a the mass of the adsorbent.

2.2.2 Instrumental information

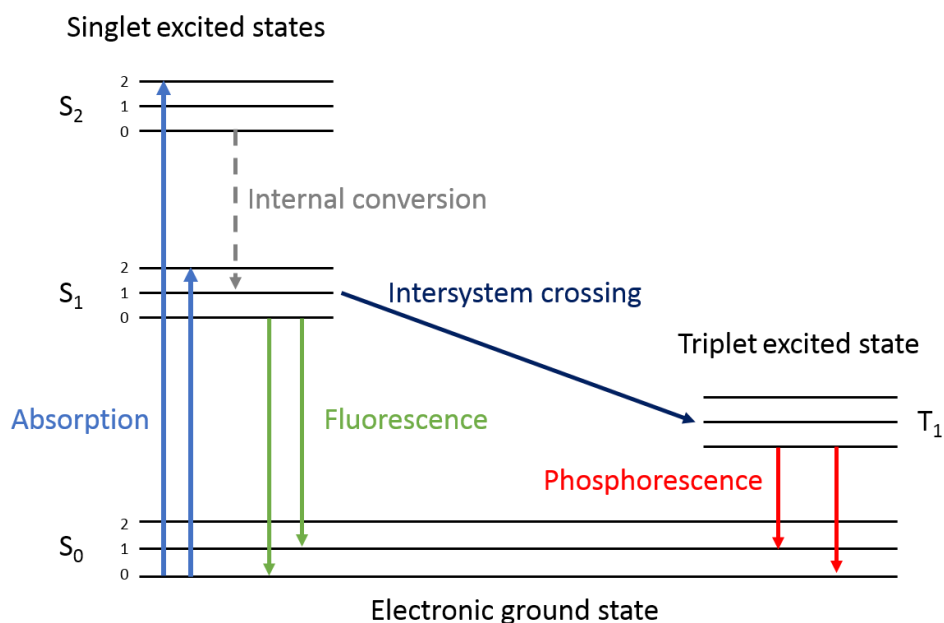
Gas adsorption measurements are performed on a Quantachrome Autosorb-1 and Quantachrome Autosorb iQ with Argon at 87 K. Sample tubes of known weight were loaded with sample. Samples were degassed at 25 °C for 120 h and measured by submerging the sample in a liquid argon bath.

2.3 Fluorescence Spectroscopy

2.3.1 Theoretical background

Fluorescence spectroscopy is an electromagnetic spectroscopy that analyses fluorescence of a sample. It is based on the excitation of electrons in molecules, which cause them to emit light. Without excitation, most molecules occupy the lowest vibrational level of the electronic ground state. Upon excitation, molecules access an electronic excited state. Due to the fact, that the electronic ground state is a singlet state, the excited state is also a singlet state, because optical transitions only occur within the same multiplicity.

After the excitation, molecules rapidly lose their excess of vibrational energy by collision and fall to the lowest excited state, by internal conversion. After few nanoseconds, the fluorescence emission occurs from the lowest singlet excited state to the electronic ground state.



Scheme 23: Schematic illustration of Jablonski diagram.

2.3.2 Instrumental information

Fluorescence measurement was performed on a Perkin Elmer EnSpire 2300 Multimode Reader. The excitation wavelength is 320 nm and the emission wavelength are recorded from 340 nm – 1000 nm.

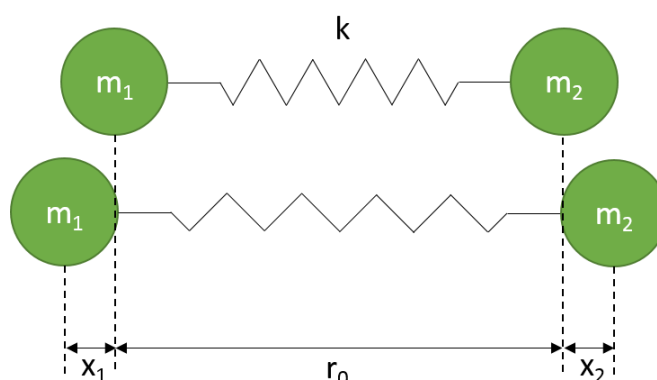
2.4 Infrared Spectroscopy (IR)

2.4.1 Theoretical background

One of the most used spectroscopic method to investigate samples in all aggregation states is the infrared (IR) spectroscopy.^[82] IR spectroscopy is based on the absorption of infrared light to study the unique molecular vibrations enabling the identification of an unknown substance. Infrared light is generally divided into three regions based on their frequency and therefore the kind of vibration that can be investigated by them. Near infrared (NIR; wavenumber: 14300 cm^{-1} – 4000 cm^{-1} ; wavelength: 0.7 – $2.5\text{ }\mu\text{m}$) is next to the visible spectra and can be used to investigate combination vibrations as well as overtones consisting of several fundamental vibrations. The middle infrared (MIR; wavenumber: 4000 cm^{-1} – 400 cm^{-1} ; wavelength: 2.5 – $25\text{ }\mu\text{m}$) is the most used region as it is used to study the fundamental and unique vibrations of molecules. The far infrared (FIR; wavenumber: 400 cm^{-1} – 20 cm^{-1} ; wavelength: 25 – $500\text{ }\mu\text{m}$) can be found at the lower end of the spectral region and can be used to probe rotation of whole molecules.

Interaction of a molecule with electromagnetic radiation leads to absorption of the energy $h\nu$ resulting in an excitation of a bond vibration. For the excitation to occur a dipole moment is necessary, this

dipole moment can either be permanent or be induced by a vibration or local symmetry distortion. Different chemical bonds exhibit characteristic frequencies that are required for excitation, enabling the identification and quantification of specific chemical groups. The vibration of the atoms can be described by various masses connected by springs. The simplest model to describe the vibration of a two atomic molecule is the harmonic oscillator. In this case, there are two mass, m_1 and m_2 which are connected through a spring with a force constant k and a distance r . The reduced mass μ ($\mu = \frac{m_1 \cdot m_2}{m_1 + m_2}$) is given by the m_1 and m_2 .



Scheme 24: Model of a two atomic molecule during vibration.

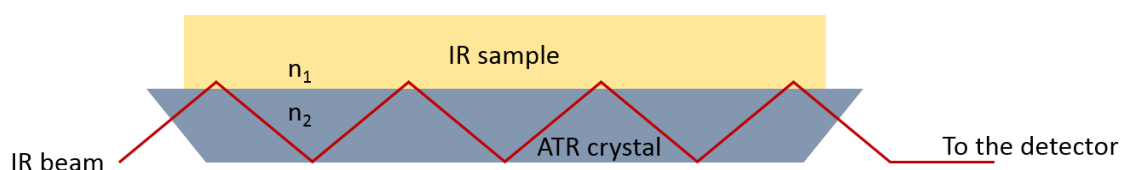
The total energy of the harmonic oscillator is given by the sum of the kinetic and potential energy. The kinetic energy is calculated by the mass and the current velocity of the different atoms. The potential energy ($V(x) = \frac{1}{2} \cdot k \cdot \Delta r^2$) depends on the force constant k and the displacement Δr . The force constant k is the bond strength between the molecules. During the vibration of the molecule, the distance of both mass changes from r_0 by $\Delta r = x_1 + x_2$. However, the force constant k is inversely related to the displacement and leads to contraction as well as prolongation after all kinetic energy is converted into potential energy. The vibration frequency of the oscillator is dependent on the reduced mass μ and the force constant k . A stronger bond as well as smaller m_1 and m_2 lead to higher vibrational frequencies ν and therefore higher energy is required for excitation of this specific vibration.

The principle setup of a FTIR-spectrometer consists of a broad band radiation source, an interferometer, a sample cell and a detector. The incident light is separated into two beams of equal amplitude by a beam splitter in the interferometer. One beam is directed to a fixed mirror, while the other beam is directed to a movable mirror. The position of the movable mirror gives rise to a path way difference between the beam of the fixed and the movable mirror. The overlap of both beams is then guided towards the sample cell and detected afterwards. With the Fourier transformation, the interferogram depending on the mirror position can be converted to frequency-dependent spectra.^[83]

In the following subchapter, attenuated total reflection infrared spectroscopy and infrared reflection adsorption spectroscopy will be introduced.

2.4.2 Attenuated Total Reflection (ATR)

Attenuated total reflection (ATR) is a technique used in conjunction with IR spectroscopy to examine samples directly in solid or liquid state without extensive sample preparation. The IR beam is conducted through a high refractive crystal. During the measurement, the beam is reflected at the interface between the ATR crystal and the sample.

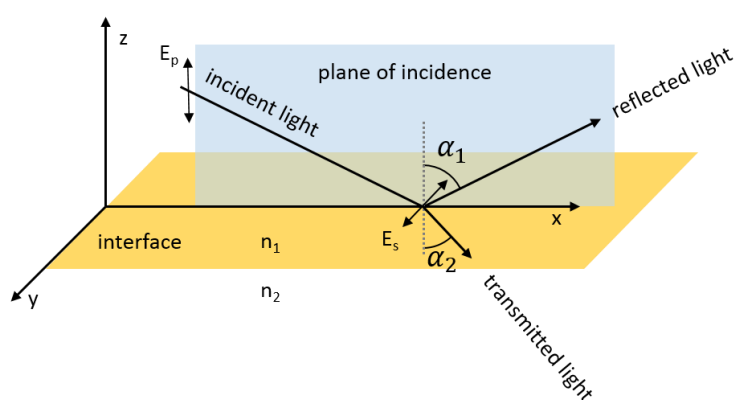


Scheme 25: Schematic illustration of the ATR setup ($n_2 > n_1$)

The requirement for the total reflection at the interface is that the sample must have a smaller refractive index than the ATR crystal.

2.4.3 Infrared reflection adsorption spectroscopy (IRRAS)

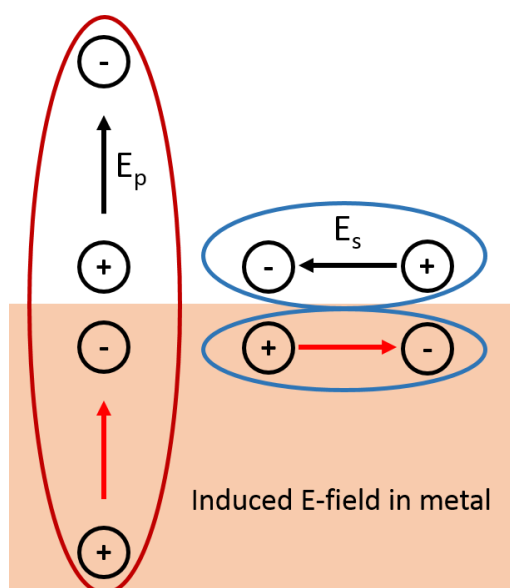
Unlike ATR, IRRAS is a technique to examine thin films on metal surfaces. In this case, the reflection of the incident beam from the sample surface as well as the excitation of the molecules through the incident beam occurs simultaneously. Due to the high sensitivity of this technique, even thin films like molecular monolayers can be detected. The beam is deflected by a mirror towards the sample, which penetrates the thin film and gets reflected by IR-reflecting metal before deflecting towards the detector.



Scheme 26: Schematic illustration of an incident light reflected at the interface of two optically different materials.

The sensitivity of the IRRAS depends strongly on the optical constants of the thin film and the substrate, the angle of incidence and the polarization of the incident light. The incident light is divided into

p-polarized as well as the s-polarized part to the plane of incidence. The reflected light is detected at an angle equal to the angle of incidence, shown in Scheme 26. The p-polarized light goes through a maximum at 88° , which can be called as grazing incidence. Metal substrates are usually preferred due to the high reflectivity of the metal surface itself. An external electromagnetic field can lead to local charge separations of the immobile nuclei and the mobile electrons. During a vibration a transition dipole moment (TDM) is induced, this induced charge separation is annihilated by the mirrored charge of the metal. This behavior leads to the findings that the vibrations with TDM perpendicular to the surface are enhanced, while vibrations parallel to the surface are suppressed, shown in Scheme 27.



Scheme 27: Schematic explanation of the surface selection rule.

2.4.4 Instrumental information

Attenuated total reflection Fourier transform infrared spectroscopy (ATR-FT-IR) was recorded on a Bruker model Tensor-27 at ambient temperature. The absorption band positions are given in wave numbers $\tilde{\nu}$ (cm^{-1}).

Infrared reflection absorption spectroscopy (IRRAS) was recorded on a Bruker model Vertex 80 purged with dried air. The IRRAS accessory (A518) has a fixed angle of incidence of 80° . The data were collected on a middle band liquid nitrogen cooled MCT detector. Perdeuterated hexadecanethiol-SAMs on Au/Ti/Si were used for reference measurements. The absorption band positions are given in wave numbers $\tilde{\nu}$ (cm^{-1}).

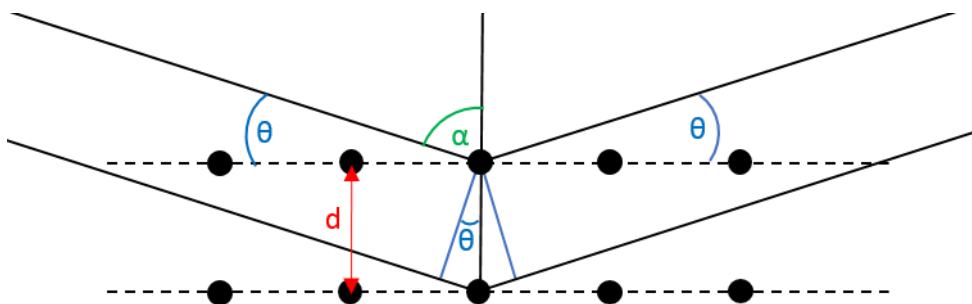
2.5 X-Ray Diffraction (XRD)

2.5.1 Theoretical background

X-Ray diffraction (XRD) is a technique which uses the constructive interference of X-rays to determine the distance between crystalline planes within a material. Upon radiation of crystals, the most radiation penetrates the material, while some gets diverted. The X-rays interact with electrons of the atoms at different positions, resulting in diffraction of the X-rays in various directions. The diffracted X-rays interfere with X-rays diffracted by other atoms within the material. In case the path way difference between two beams is within a specific range constructive interference occurs and the beam is enhanced, while for the case that this condition is not met destructive interference occurs and the beams cancel each other out. William Lawrence Bragg and his father William Henry Bragg developed in 1913 the Bragg equation, which explains the distance required for constructive interference.

$$n \cdot \lambda = 2 \cdot d \cdot \sin(\theta) \quad (18)$$

In this equation, n describes the diffraction order, λ the of the X-ray, d the distance between two planes and θ the angle between the X-ray and the lattice plane.



Scheme 28: Schematic illustration of constructive interference on periodic lattice planes.

The X-ray diffractometer consist generally of three parts: An X-ray source, a goniometer and a detector. As X-ray source, a hot tungsten filament produces electrons, which are accelerated towards the opposite charged anode. As anode, different metals can be used, e.g. Cu, Mo or Ag, which emit a wide range of different photons after the collisions. Due to the wide range of emitted X-rays, monochromators are used to filter out the unwanted part of the radiation. The beam is then diffracted by the sample, the detector records the incoming X-rays and converts them to signals which can be seen on the computer.

2.5.2 Instrumental information

XRD measurements were performed using a Bruker D8-Advance diffractometer (IFG) and a Bruker D8-Discover diffractometer (ITG). Both are in θ - θ geometry and equipped with a PSD Lynxeye®. For the

D8-Advance, Cu-anodes (Cu K α 1,2-radiation with $\lambda = 1.5418 \text{ \AA}$) was used. For the D8-Discover, Mo-anodes (Mo K α 1,2-radiation with $\lambda = 0.7109 \text{ \AA}$) was used.

2.6 Mass Spectrometry

2.6.1 Theoretical background

Mass spectrometry is an analytic technique that measures the mass of different molecules within a sample. In general, mass spectrometry based on the ionization of solid, liquid or gas with electrons or low charged cations (H⁺ or Na⁺). Ionizations occurs in the ion source. Ionization are usually divided in hard- and soft ionization. Hard ionization leads to high degree of fragmentation resulting in highly detailed spectra. A common example for hard ionization is the electron ionization (EI). Unlike hard ionization, soft ionization transfers less energy to the analyzed molecule resulting in less fragmentation. Example are fast atom bombardment (FAB), electrospray ionization (ESI) and matrix-assisted laser desorption/ionization (MALDI). After the ionization, the fragments go through a mass analyzer, which separate the ions according to their mass-to-charge ratio. The analyzers are divided into many types, using either static, dynamic, magnetic or electric field. The final part of the mass spectrometer is the detector, which records the ions/fragments that passed by or hits the surface, resulting in a mass spectrum.

2.6.2 Electrospray Ionization Mass Spectrometry (ESI-MS)

ESI (Electrospray Ionization) mass spectra was obtained using X500R QTOF mass spectrometer. The sample was measured in TOFMS positive mode. The indication of the molecular weight was carried out as mass to charge m/z .

2.6.3 Fast Atom Bombardment Mass Spectrometry (FAB-MS)

FAB (Fast Atom Bombardment) mass spectra were obtained using a FINNIGAN *MAT* 95 mass spectrometer. The indication of the molecular fragments was carried out as the ratio of mass to charge m/z ; the intensity of the signals was expressed in percent relative to the intensity of the base signal (100%).

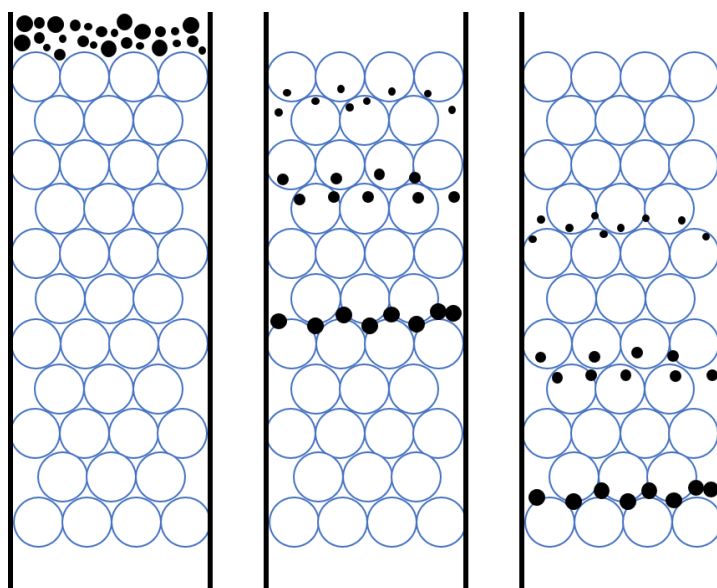
2.6.4 Time of Flight Secondary Ion Mass Spectrometry (ToF-SIMS)

ToF-SIMS measurement was performed on a TOF.SIMS5 instrument from ION-TOF GmbH. This spectrometer is equipped with a Bi cluster primary ion source and a reflection type time of flight analyzer.

2.7 Gel Permeation Chromatography (GPC)

2.7.1 Theoretical background

Gel permeation chromatography (GPC) is a type of size exclusion chromatography (SEC), which separates analytes based on size. This technique is usually used to analyze the size of polymers. GPC employs a stagnant liquid present in the pores of beads (column) as the stationary phase, and a flowing liquid as the mobile phase (analyte). The dissolved polymer in the mobile phase flows between the beads and in and out of the pores in the beads. If the dissolved polymer coils are much larger than the biggest pores in the beads, they will directly pass by the mobile phase. If the dissolved polymer coils are a little smaller than the biggest pores, they will enter the larger but not the smaller pores when they pass by. If the dissolved polymer coils are smaller than the smallest pores in the beads, they will enter any of the pores when they pass by. As a result, smaller polymer that can enter many pores in the beads take longer time to pass through the column and therefore exit the column slowly. In contrast to the smaller polymer, the larger polymer cannot enter some pores, which take less time to leave the column. The schematic illustration of the GPC column is shown in Scheme 29.



Scheme 29: Schematic illustration of GPC column.

2.7.2 Instrumental information

The gel permeation chromatography measurements were performed on a PL-GPC 50 Plus from Agilent Technologies. This device is equipped with RI, UV detector and TOSOH TSK (G4000HXL, G3000HXL and G2000HXL) gel columns. All measurements were performed in tetrahydrofuran (THF) (1 mL/min) with trichlorobenzene as flow marker.

2.8 Nuclear Magnetic Resonance Spectroscopy (NMR)

2.8.1 Theoretical background

Nuclear magnetic resonance spectroscopy (NMR) is an analytical technique that can determine the content, purity as well as the molecular structure of a material. It is based on the investigation of materials through the measurement of nuclear magnetic interactions. When a molecule is exposed to an external magnetic field, each atom will feel a slightly different effect. This modified field depends on the magnetic shielding, which is induced by neighboring nuclei and electrons. Many atomic nuclei e.g. ^1H , ^{13}C , ^{15}N , ^{31}P etc. possess a physical property known as nuclear spin. While moving, the electrons generate a magnetic moment that affects the nuclei. Nuclear magnetic moments can be aligned during the exposure to a sufficiently strong magnetic field. In an NMR spectrometer, the sample is placed in a small coil. The rotating magnetic moments induce a voltage signal in the coil which results in the NMR signal. After Fourier transformation, the NMR signal is transformed to the NMR spectrum, in which the characteristic frequencies of the processing nuclear magnetic moments are shown as distinct peaks.

2.8.2 Instrumental information

NMR spectra were recorded on a BRUKER *Avance* 400 (^1H : 400 MHz) of solutions in CDCl_3 , CD_2Cl_2 and. Chemical shifts (δ) are expressed in parts per million (ppm) and are referenced to CHCl_3 (^1H : 7.26 ppm) respectively as internal standard. All coupling constants (J) are absolute values and J values are expressed in Hertz (Hz). The description of signals includes: s = singlet, bs = broad singlet, d = doublet, dd = doublet of doublets, hept = heptet, m = multiplet, kb = complex area and AA'BB' for a more complex system (no first order). The spectra were analyzed according to first order.

2.9 Thermogravimetric analysis (TGA)

2.9.1 Theoretical background

Thermogravimetric analysis is a technique that measures the mass of a sample while it is heated, cooled or held isothermally in a defined atmosphere. During the measurement, the TGA shows the mass loss steps relating to the loss of volatile components e.g. moisture, solvent or monomers, polymer decomposition, combustion of carbon and final residues. This technique reveals the decomposition of materials and using this information, the materials individual constituents can be investigated.

2.9.2 Instrumental information

Thermogravimetric analysis was made on a NETZSCH STA 449 C in the temperature range 35 °C to 1000 °C with a heating rate of 5 K/min and was carried out under an argon atmosphere.

2.10 Differential Scanning Calorimetry (DSC)

2.10.1 Theoretical background

Differential scanning calorimetry (DSC) is a technique, that measures the heat flow of samples as a function of temperature over time. It measures the amount of energy absorbed or released by a sample when it is heated or cooled. The measurement provides quantitative and qualitative information on exothermic and endothermic processes.

Upon cooling, some amorphous materials become brittle like glass, which becomes soft during heating. This reversible transition is called glass transition, which can be characterized by the glass transition temperature T_g . At a specific temperature, a material undergoes a phase transition from solid to liquid state, which is called melting. This process is endothermic and occurs at a specific temperature for specific pure substances. Exothermic phase transitions are usually caused by crystallization. Upon cooling, some materials undergo phase transition from liquid to ordered solid. Thermoplastic material possesses inherent crystallinity, whereby amorphous material undergoes usually a cold crystallization.

2.10.2 Instrumental information

Differential scanning calorimetry (DSC) experiments were carried out with DSC821e calorimeter from METTLER TOLEDO in nitrogen atmosphere, employing a sample mass of approximately 3 mg. The glass transition temperature T_g is reported as the curves inflection point (first derivative equals zero). Heating and cooling rate of 25 °C pro minute were used in all measurements. All values were recorded on the second heating cycle to ensure equal thermal history for all samples.

2.11 Spectroscopic Ellipsometry (SE)

2.11.1 Theoretical background

Ellipsometry is a highly sensitive optical technique, which uses polarized light to determine the thickness and dielectric properties of thin film samples, by measuring the change of polarization of the light reflected off a sample. This even allows to yield information about layers that are thinner than the wavelength of the incident light itself.^[84]

2.11.2 Instrumental information

Ellipsometry analysis were performed on M-44 ellipsometer from J. A. Woollam Co., An arc lamp with a high pressure Xe discharge point source was used. The modeling, fitting and regression analysis of the ellipsometric data were performed using the software WVASE™.

2.12 Microscopy

2.12.1 Atomic Force Microscopy (AFM)

AFM-imaging was performed using an Asylum Research Atomic Force Microscope, MFP-3D BIO. The AFM was operated at 25 °C in an isolated chamber in alternating current mode (AC mode). AFM cantilevers were purchased from Ultrasharp™ MikroMasch. Three types of AFM-cantilevers were used, an NSC-35 (resonance frequency 315 kHz; spring constant 14 N/m), an NSC-36 (resonance frequency: 105 kHz; spring constant: 0.95 N/m) and an NSC-18 (resonance frequency: 75 kHz; spring constant: 3.5 N/m)

2.12.2 Scanning Electron Microscopy (SEM).

SEM images were recorded using a FEI Philips XL30 (FEI Co., Eindhoven, NL), a field emission gun environmental scanning electron microscope (FEG-ESEM), Samples have been coated with a thin layer (about 5 nm) of gold/palladium film in order to avoid charging and improve sample conductivity. Subsequently, all specimen imaged under high vacuum condition (1.0 Torr), using acceleration voltage 20 keV.

3. Material and Experiment

3.1 Material

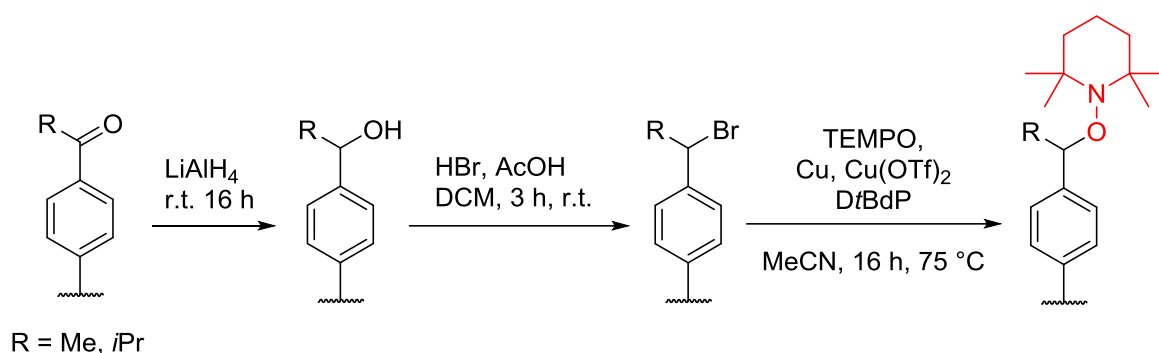
All chemicals were purchased from commercial sources and used without further purification if not stated otherwise. All solvents were degassed three times via freeze-pump-thaw prior to use.

Table 1: Source of supply for the utilized chemicals.

Chemicals	Supplier
Toluene	Merck Millipore
Methanol	Merck Millipore
<i>N,N</i> -diethylformamide (DEF)	Merck Millipore
Cyclohexane	Merck Millipore
Dichloromethane (DCM)	Merck Millipore
Tetrahydrofuran (THF)	VWR Chemicals
Poly(methyl methacrylate) (PMMA) Mw~120.000	Sigma-Aldrich
Polystyrene (PS) Mw~170.000	Sigma-Aldrich
Anisole	Merck Millipore
1,4-Dioxane	Merck Millipore
Mesitylene	Merck Millipore
Acetone	VWR Chemicals
4-amino-TEMPO	Sigma-Aldrich
1,4,5,8-Naphthalenetetracarboxylic dianhydride	Sigma-Aldrich

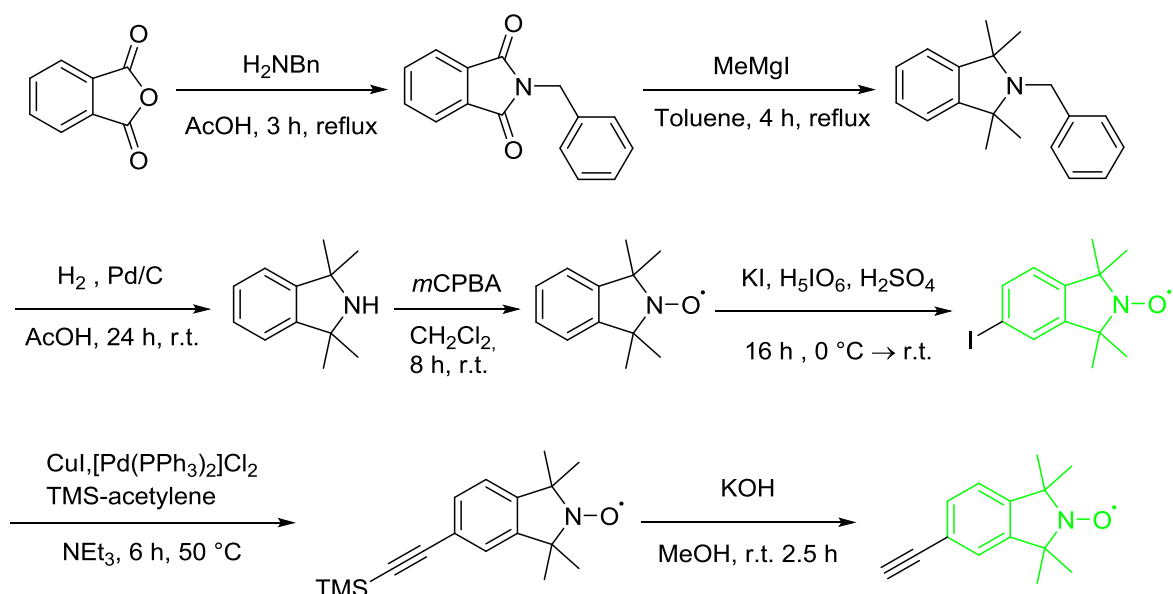
3.2 Synthesis of the building blocks for Nitroxide exchange reaction

The building blocks used in this thesis are not commercially available. The synthesis of all building blocks with exception of Di-NO (Scheme 35) were performed and provided by Dr. Isabelle Wessely and Yannick Matt from the group of Prof. Stefan Bräse (IOC/KIT) if not stated otherwise.



Scheme 30: Synthesis procedure of multifold alkoxyamines.

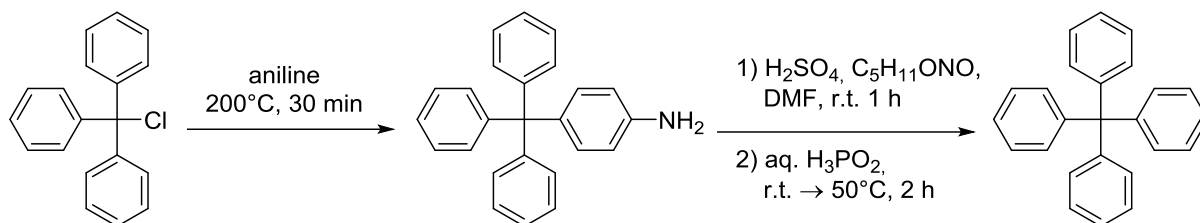
For this study, mono-, di-, tri- and tetra-fold alkoxyamines were synthesized. Regardless of the later number of functional groups, para-functionalized ketones are used as starting materials. In the next step, the ketone functional group is reduced with LiAlH_4 to secondary alcohols. Using nucleophile substitution ($\text{S}_{\text{N}}1$), the alcohol group was transformed into bromide. In the last step, using a copper complex as catalyst, TEMPO was introduced by substituting the bromide resulting in mono or multifold alkoxyamine.^[23]



Scheme 31: Synthesis procedure for Iodo-Tetramethyl-Isoindoline-NO and Alkyne-Tetramethyl-Isoindoline-NO.

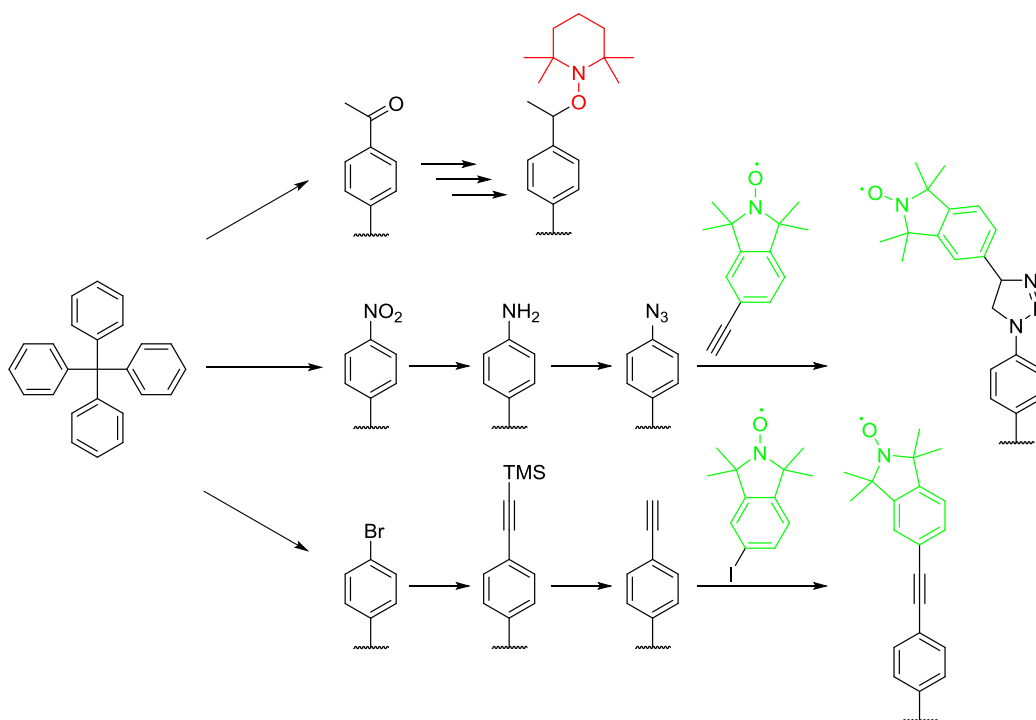
Also, multifold nitroxides (abbreviated as NO) used in this study were synthesized. For the synthesis of Tri-[S]-NO, Tetra-[S]-NO and Tetra-[C]-NO, functionalized tetramethyl-isoindoline nitroxide were synthesized. In the first step, the nitrogen is introduced through benzylamine into phthalic anhydride.^[85] To prevent hydrogen abstraction in the later exchange reaction, the four fold- Grignard-reaction was performed. With hydrogen and Pd/C, the amine-group was deprotected to tetramethyl-isoindoline.^[86] After oxidation with *m*CPBA, the bare tetramethyl-isoindoline-NO was synthesized.^[87] To link this nitroxide to different cores, iodide functionalized tetramethyl-isoindoline-NO was synthesized. This can be used for synthesis of multifold nitroxides using Sonogashira-Hagihara reaction.

It can also be further functionalized to alkyne-tetramethyl-isoindoline-NO via TMS-protection.^[88] The alkyne-functionalized nitroxide can be used to prepare multifold nitroxides via Copper(I)-catalyzed Azide-Alkyne Cycloaddition.



Scheme 32: Synthesis route of tetraphenylmethane.

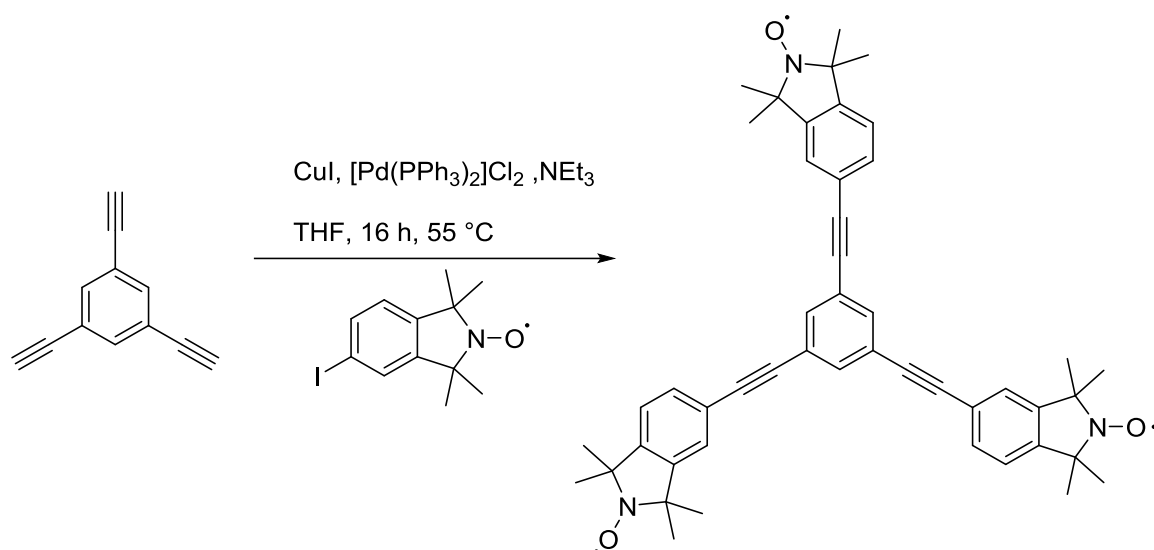
The core of the tetra-fold linkers is based on the tetraphenylmethane (TPM), the synthesis starts with an Friedel-Crafts-Alkylation of trityl chloride with aniline. The resulting amino-TPM is then transformed into a diazotated species by pentyl nitrite that can be reduced to the bare TPM by hypophosphorous acid.^[89]



Scheme 33: Synthesis procedure of alkoxyamine and nitroxide based on TPM core.

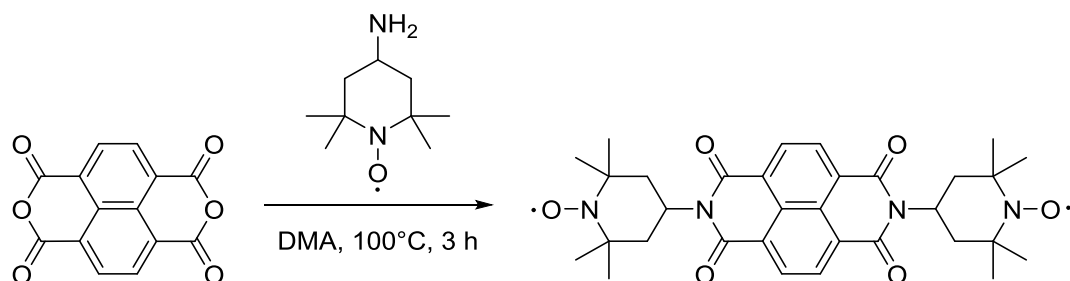
The TPM core can be used for the synthesis of tetra-fold alkoxyamine as well as tetra-fold nitroxide. In this study, two types of tetra-fold nitroxide are used. The Tetra-[C]-NO are synthesized based on the tetra para-functionalized TPM-NO₂. The nitro-group was first reduced via hydrogenation to TPM-NH₂. Afterwards, diazotization was implemented to introduce the azide group to the TPM core.^[89] Via Copper(I)-catalyzed Azide-Alkyne Cycloaddition (CuAAC) of TPM-N₃ and alkyne functionalized tetramethyl-isoindoline-NO, Tetra-[C]-NO was synthesized.

For the synthesis of Tetra-[S]-NO, the TPM undergo first a bromination with elemental bromine and later substituted with alkyne via TMS protection.^[89] Via Sonogashira-Hagihara cross-coupling of TPM-alkyne and iodo-tetramethyl-isoindoline-NO, Tetra-[S]-NO is synthesized.



Scheme 34: Synthesis of Tri-[S]-NO.

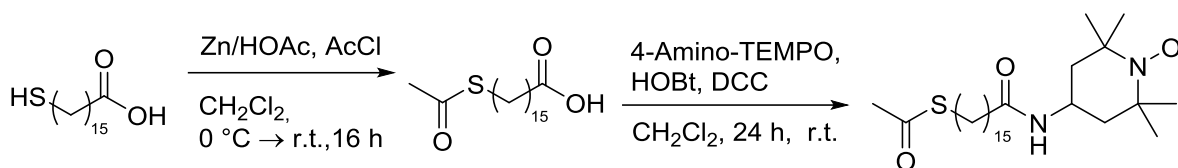
The synthesis of Tri-[S]-NO proceed analog to the synthesis of Tetra-[S]-NO, where only the core molecule is change to 1,3,5-triethynylbenzene.^[90]



Scheme 35: Synthesis of Di-NO.

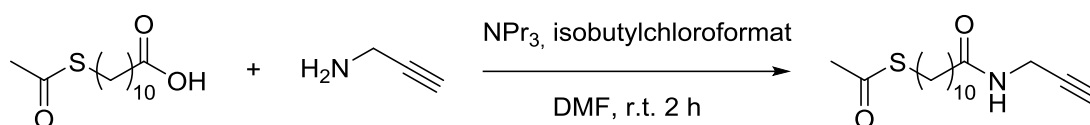
For the synthesis of dinitroxide, naphthalenetetracarboxylic dianhydride was used as core. The Di-NO was produced via condensation reaction of Amino-TEMPO with the dianhydride.

3.3 Synthesis of self-assembled monolayer for the thin-film preparation



Scheme 36: Synthesis of thiolacetyl-C₁₆-TEMPO.

To synthesize the TEMPO functionalized SAM, 16-mercaptohexadecanoic acid (abbreviated as MHDA) was used as precursor. Glacial acid was used to oxidized Zn to Zn²⁺, which activated the acetylchloride for the protection of the thiol group. The acetyl-protected thiol was then transformed to acetylthiol-C₁₆-TEMPO using 4-amino-TEMPO, which undergone an amid linkage with the carboxylic acid group of the acetyl-protected thiol.

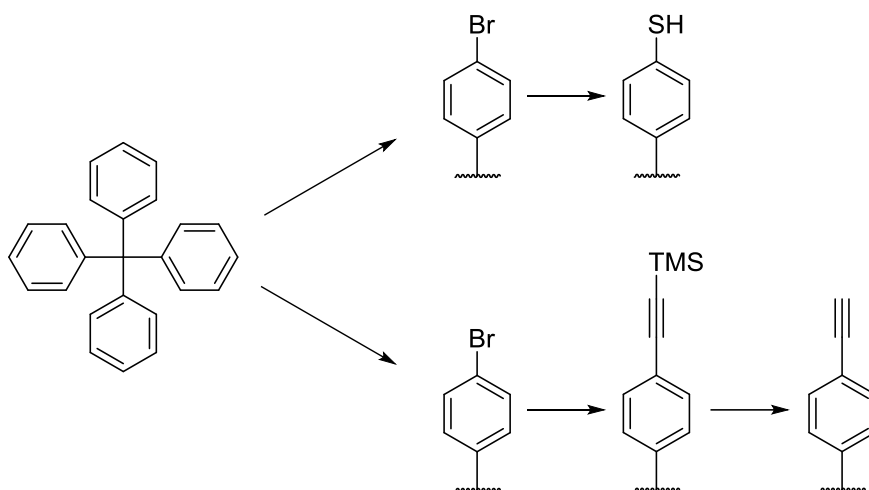


Scheme 37: Synthesis of 11-thiolacetyl-undecanic propargylamide.

The alkyne functionalized SAM was synthesized by Dr. Peter Lindemann at IFG/KIT. 11-thiacetyl-undecanoic acid was functionalized via condensation reaction with propargyl amine.^[91]

3.4 Synthesis of building blocks for thiol-yne coupling thin films

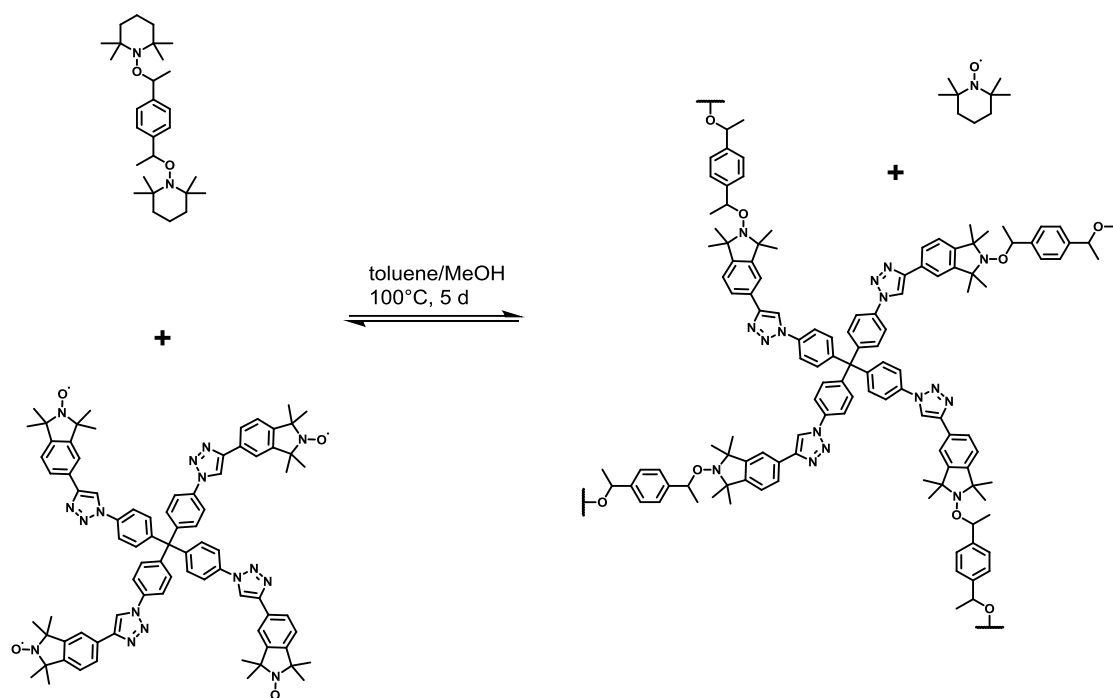
The organic building blocks for the thiol-yne coupling thin film are synthesized and provided by Dr. Mathias Lang from the group of Prof. Stefan Bräse (IOC/KIT).



Scheme 38: Synthesis procedure of TPM-SH and TPM-alkyne for the CMP membrane production.

The synthesis of TPM-SH and TPM-alkyne are both based on the TPM core, which already introduced in the previous chapter. For the synthesis of TPM-SH, the TPM was first brominated using elemental bromine and later substituted via nucleophilic aromatic substitution (S_NAr) to TPM-SH. The synthesis of TPM-alkyne was already introduced in the previous chapter as an intermediate product.^[92]

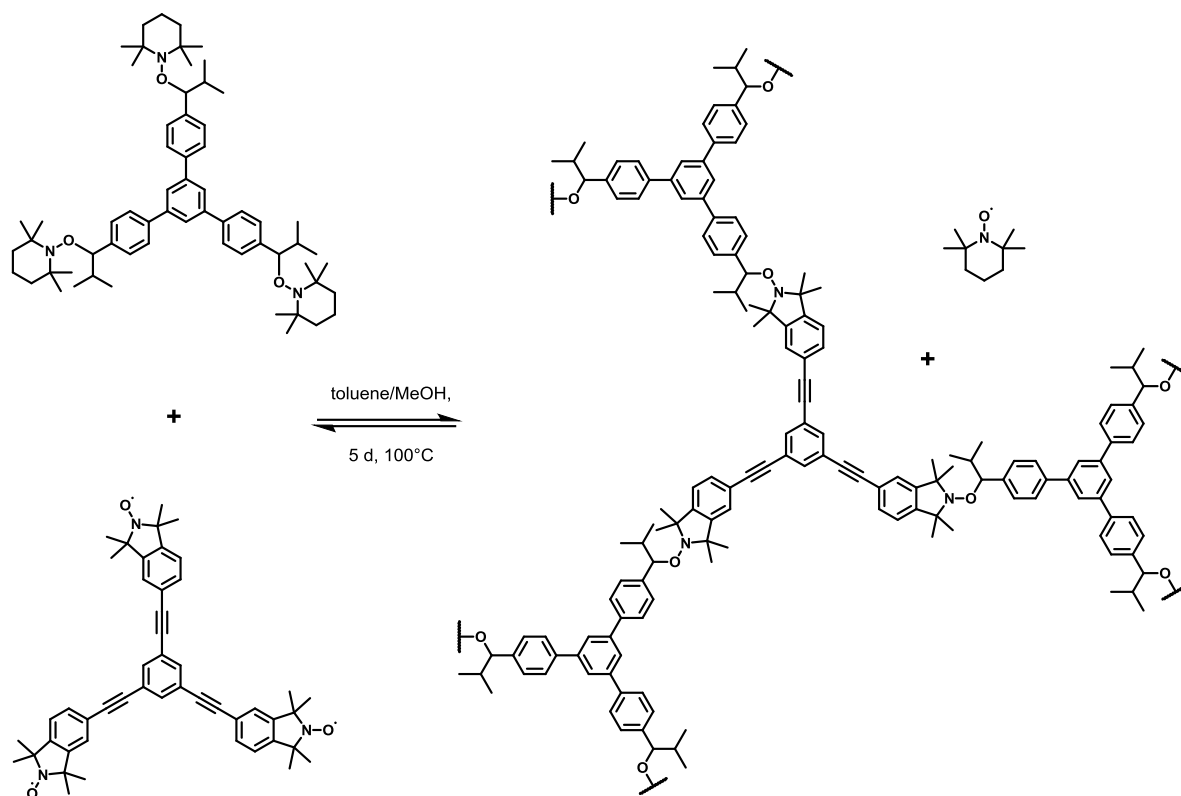
3.5 Synthesis of dynamic covalent polymer framework



Scheme 39: Synthesis of [2+4C] framework.

Synthesis of [2+4C] NER polymer framework: The porous polymer framework was prepared by multiple nitroxide exchange reaction of the Tetra-[C]-NO (1.00 equiv., 0.044 mmol) and the Di-AA (2.00 equiv., 0.088 mmol) in 0.9 mL of a toluene/methanol-mixture (9/1). The solvent mixture was freeze-dried before use and added to the starting materials under oxygen free conditions in a glovebox. The vial was sealed and placed in an oven for 24 h at 100 °C. The crude product was washed five times with toluene to remove the in-situ released TEMPO product during thermolysis/nitroxide exchange of alkoxyamines. The reaction progress and notably, the TEMPO obtained by the cleavage of alkoxyamine during network formation was evaluated quantitatively using electron paramagnetic resonance (EPR) measurements. After washing, the polymer framework was dried with a critical point dryer using supercritical CO₂ to give 33.1 mg (0.02 mmol) of a pale beige product. – Yield: 47%

IR: $\nu_{\max}/\text{cm}^{-1}$ 2975 (asym. aliphatic-CH₃), 2929, 2863 (sym. aliphatic-CH₃), 2360, 2336, 1606, 1513(CONH), 1482, 1440, 1361 (NO), 1226, 1164 (C-C), 1122 (1,4 aryl-CH), 1065, 97, 877, 824. – $\text{SA}_{\text{BET}} = 378 \text{ m}^2/\text{g}$ – $\text{SA}_{\text{L}} = 619 \text{ m}^2/\text{g}$ – $V_{\text{Total,pore}} = 0.576 \text{ cm}^3/\text{g}$



Scheme 40: Synthesis of [3+3] framework.

Synthesis of [3+3] NER polymer framework: The organic framework was prepared by multiple nitroxide exchange reaction of the Tri-NO (1.00 equiv., 0.063 mmol) and the Tri-AA (1.00 equiv., 0.063 mmol) in 0.9 mL of a toluene/methanol-mixture (9/1). The toluene/methanol bi-solvent system proved as the most effective among the solvents evaluated. The solvent mixture was freeze-dried before use and added to the starting materials under oxygen free conditions in a glovebox. The vial was sealed with a cap and placed in an oven for 24 h at 100 °C. The crude network was washed five times with toluene to remove the released TEMPO byproduct. After washing, the network was dried with a critical point dryer using supercritical CO₂ to give 71.1 mg (0.06 mmol) of a slightly yellow product. – Yield: 95%

IR: $\nu_{\max}/\text{cm}^{-1}$ 2971 (asym. aliphatic-CH₃), 2929, 2871 (sym. aliphatic-CH₃), 2361, 2339, 1685, 1578 (CONH), 1360 (NO), 1262, 1162 (C-C), 1119 (1,4 aryl-CH), 1004 (1,3 aryl-CH), 977 (1,3,5 aryl-CH), 877, 824 (1,3,5 aryl-CH); Raman: $\nu_{\max}/\text{cm}^{-1}$ 3061 (aryl-CH), 2934 (aliphatic-CH), 2210 (alkyne), 1613, 1578 (CONH), 1348 (NO), 1169 (aryl-CH), 1062 (aryl-CH), 993 (aryl-CH); S_{BET} (Ar, 87 K): 90 m²/g; EA: (C₈₄H₈₇N₃O₃, 1186.64): calcd.: C 85.02, H 7.39, N 3.54; found: C 83.27, H 7.38, N 3.64; TGA: T(5% weight lost): 292°C.

Investigation of the reaction process with EPR spectroscopy: The samples were prepared by nitroxide exchange reaction of the three-fold nitroxide radical (1.00 equiv., 0.063 mmol) and the three-fold alkoxyamine species (1.00 equiv., 0.063 mmol) in 0.9 mL of a toluene/methanol-mixture (9/1) in

different sealed vials. The vials were taken out of the oven after 1 h, 2 h and 5 h. 0.01 mL of the sample were abstracted and diluted with 1.0 mL DEF (diethylformamide) to proceed for EPR measurements.

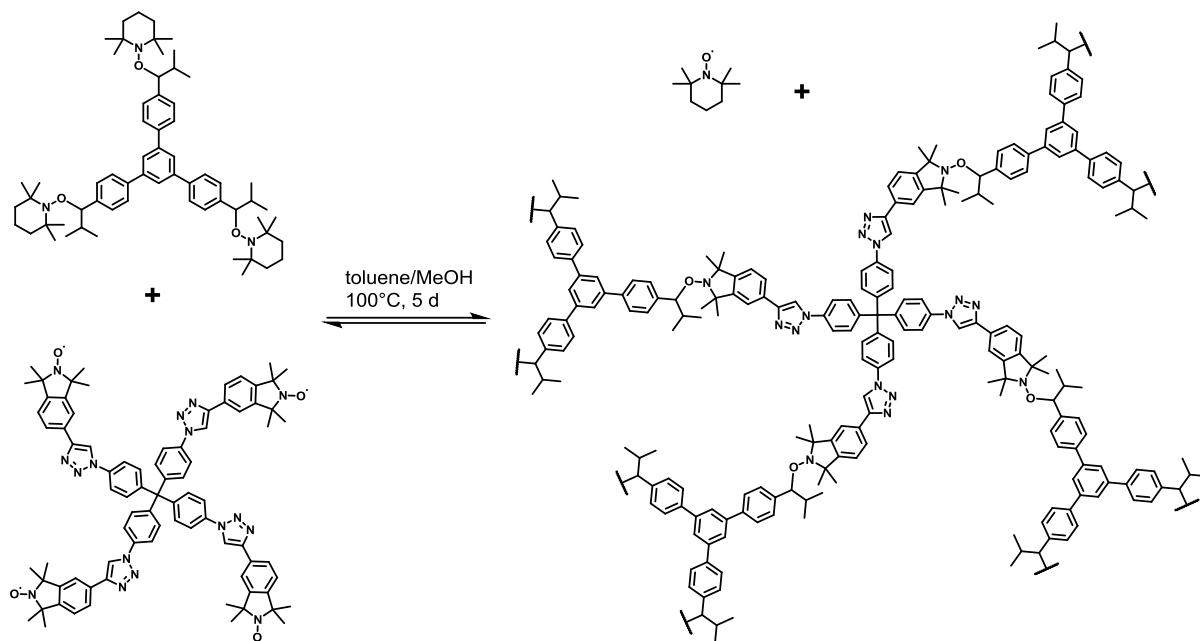
Investigation of the reaction process via fluorescence spectroscopy: The samples were prepared by nitroxide exchange reaction of the three-fold nitroxide radical (1.00 equiv., 0.063 mmol) and the three-fold alkoxyamine species (1.00 equiv., 0.063 mmol) in 0.9 mL of a toluene/methanol-mixture (9/1) in a sealed vial. 100 μ L aliquot were taken out of the vial after 1 h, 2 h, 5 h respectively. The organic framework was observed after 8 h. A piece (10 mg) of the network was cut and washed five times. After that, the fluorescence was investigated at 320 nm excitation wavelength.

Swelling experiments: First, the organic framework was washed with toluene constantly, until TEMPO in the washing solution is not measurable anymore in EPR. Afterwards, the organic framework was dried with the critical point dryer using supercritical CO₂. The swelling behavior was successively investigated with toluene, at pristine, annealed and softened state at 25 °C. For this purpose, the dried organic framework was placed in pure solvent at room temperature. After 15 min, 30 min, 1 h, 2 h, 6 h, 12 h, 24 h, 36 h, and 48 h, the solvent was removed, and the weight of the network was measured to determine the swelling degree (Q). After that, the organic framework was annealed at 100°C for 24 h and dried again with the critical point dryer. The swelling degree (Q) was investigated using the same conditions as before. Afterwards, the organic framework was de-crosslinked with 5 equiv. TEMPO (0.026 mmol) at 100 °C for 24 h and dried again with the critical point dryer. The swelling degree (Q) was investigated using the same conditions as before.

Disassembly (decrosslinking) experiment: For the disassembly experiment, 0.492 g of TEMPO (18 equiv., 3.15 mmol) in 2 mL toluene was added to the organic framework in a Schlenk tube. The solvent was freeze-dried before use. The Schlenk tube was heated for 24 h at 100 °C. The gel-sol transition was checked after 3 h, 6 h and 24 h. For further investigation with mass spectrometry, the excess amount of TEMPO was removed via sublimation and the reaction mixture was investigated with FAB-MS. Three-fold nitroxide radical as well as three-fold alkoxyamine and their fragmentations were detected. m/z (%): 784 [TriAA – TEMPO+H⁺], 716 [TriNO + 2 × H⁺], 702 [TriNO – CH₃ + 2 × H⁺], 686 [TriNO – 2 × CH₃], 670 [TriNO – 3 × CH₃ + H⁺], 654 [TriNO – 4 × CH₃], 471 [TriAA – 3 × TEMPO], 156 [TEMPO], 140 [C₉H₁₈N⁺]. Since the mass at 471 can also be a fragment of TriNO, this mass was investigated again with HR-MS. In the HR-MS, $m/z = 471.3052$ was found which confirmed the presence of fragment from TriAA. After investigation with ESI-TOFMS, the mass of TriNO was detected as m/z (%): 715,3595 [TriNO + H⁺].

Self-healing experiment: First, the polymer gel was washed with toluene, until no TEMPO was detected in the washing solution anymore during EPR analysis. Afterwards, the organic framework was cut in two pieces with a scalpel and placed in a vial with 2 mL toluene under oxygen free condition. The vial

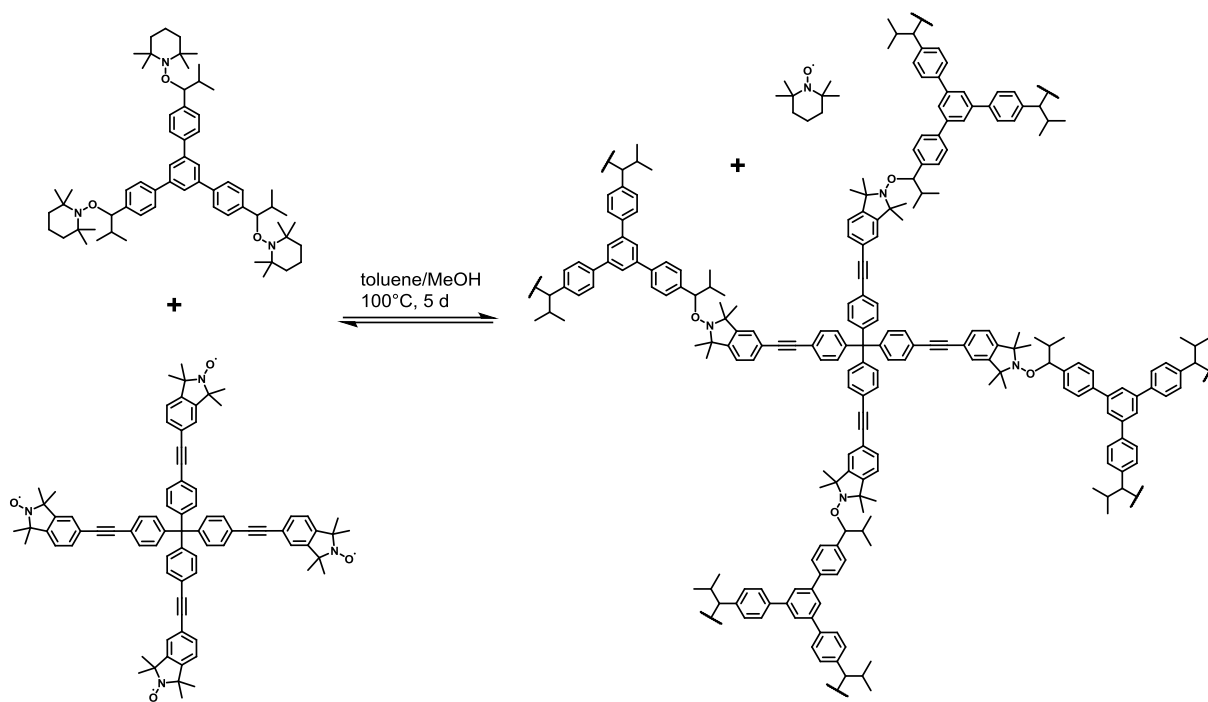
was then filled with 3 mm glass beads to fix the position of the organic framework. The self-healing property was observed after 24 h.



Scheme 41: Synthesis of [3+4C] framework.

Synthesis of [3+4C] NER polymer framework: The porous polymer framework was prepared by multiple nitroxide exchange reaction of the Tetra-[C]-NO (1.00 equiv., 0.022 mmol) and the Tri-AA (1.33 equiv., 0.029 mmol) in 0.9 mL of a toluene/methanol-mixture (9/1). The solvent mixture was freeze-dried before use and added to the starting materials under oxygen free conditions in a glovebox. The vial was sealed with a cap and placed in an oven for 5 d at 100 °C. The crude product was washed five times with toluene to remove the in-situ released TEMPO product during thermolysis/nitroxide exchange of alkoxyamines. After washing, the polymer framework was dried with a critical point dryer using supercritical CO₂ to give 8.88 mg (0.005 mmol) of a pale beige product. – Yield: 20%

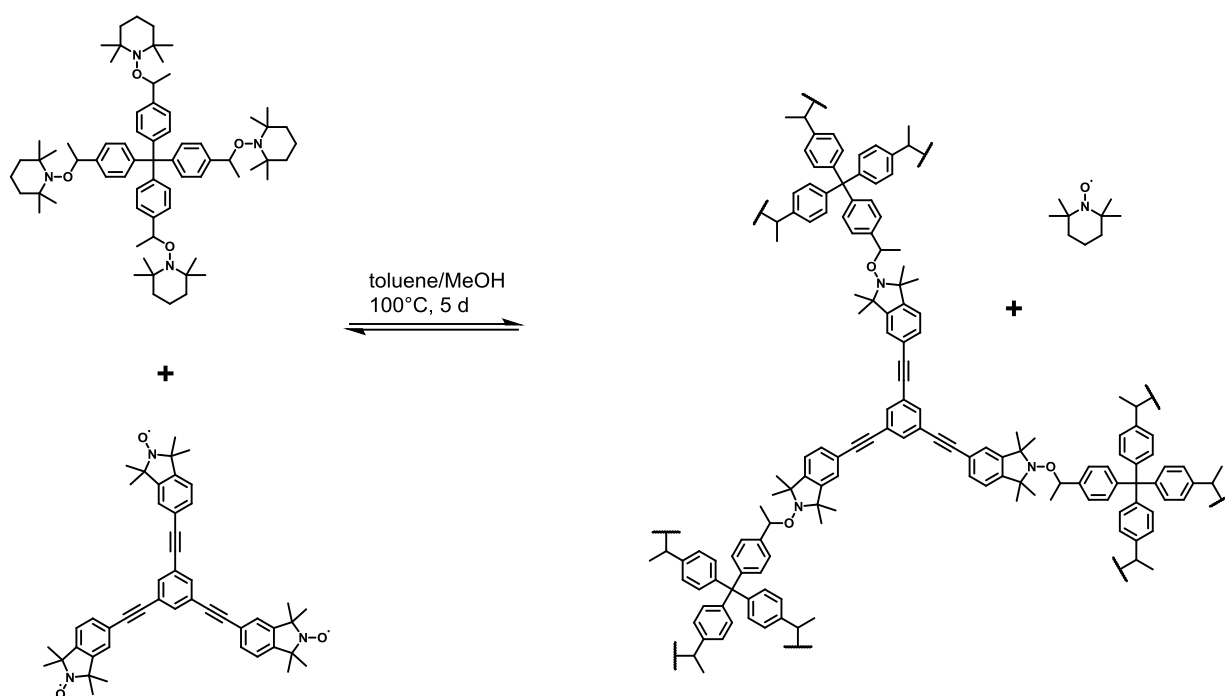
IR: $\nu_{\max}/\text{cm}^{-1}$ 2967 (asym. aliphatic-CH₃), 2925, 2870 (sym. aliphatic-CH₃), 2362, 2335, 1684, 1602 (CONH), 1510, 1360 (NO), 1221, 1162 (C-C), 1119 (1,4 aryl-CH), 1028 (1,3 aryl-CH), 990 (1,3,5 aryl-CH), 824 (1,3,5 aryl-CH). – $S_{\text{BET}} = 1200 \text{ m}^2/\text{g}$ – $S_{\text{L}} = 1950 \text{ m}^2/\text{g}$ – $V_{\text{Total,pore}} = 2.614 \text{ cm}^3/\text{g}$



Scheme 42: Synthesis of [3+4S] framework.

Synthesis of [3+4S] NER polymer framework: The porous polymer framework was prepared by multiple nitroxide exchange reaction of the Tetra-[S]-NO (1.00 equiv., 0.022 mmol) and the Tri-AA (1.33 equiv., 0.029 mmol) in 0.9 mL of a toluene/methanol-mixture (9/1). The solvent mixture was freeze-dried before use and added to the starting materials under oxygen free conditions in a glovebox. The vial was sealed and placed in an oven for 24 h at 100 °C. The crude product was washed five times with toluene to remove the in-situ released TEMPO product during thermolysis/nitroxide exchange of alkoxyamines. After washing, the polymer framework was dried with a critical point dryer using supercritical CO₂ to give 13.0 mg (0.007 mmol) of a pale beige product. – Yield: 25%

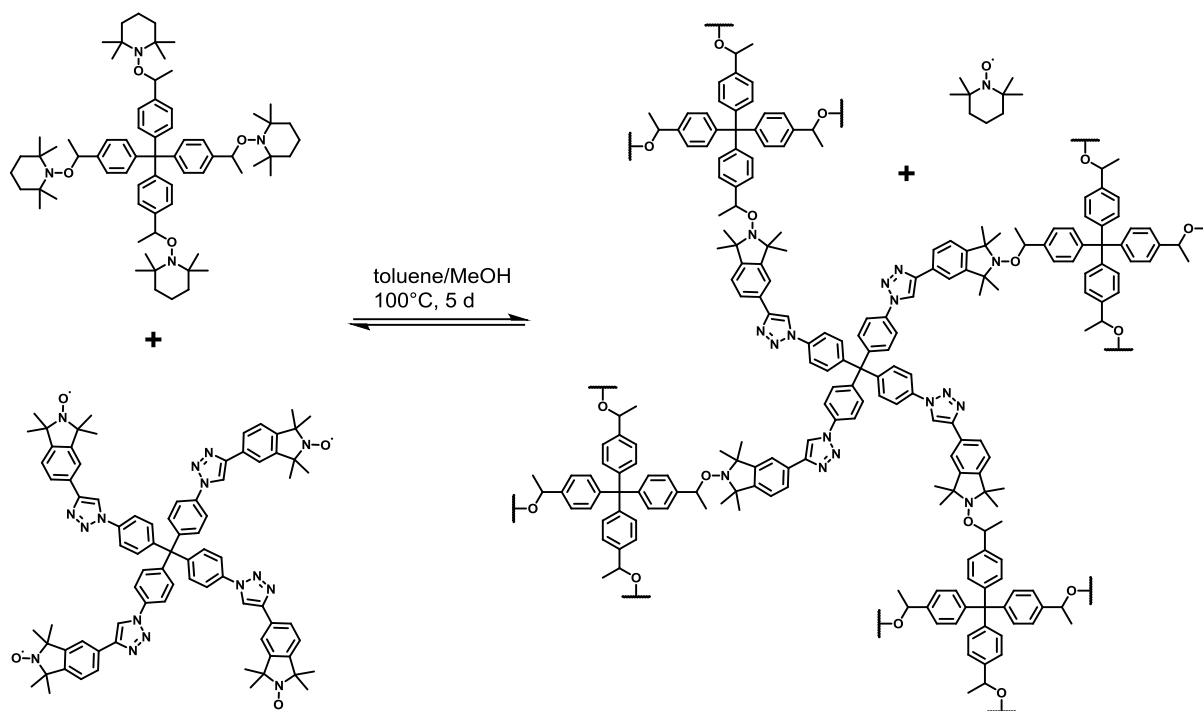
IR: $\nu_{\max}/\text{cm}^{-1}$ 2972 (asym. aliphatic-CH₃), 2927, 2858 (sym. aliphatic-CH₃), 2361, 2339, 1685, 1503 (CONH), 1360 (NO), 1270, 1162 (C-C), 1118 (1,4 aryl-CH), 1065 (1,3 aryl-CH), 977 (1,3,5 aryl-CH), 830 (1,3,5 aryl-CH). – $S_{\text{ABET}} = 179 \text{ m}^2/\text{g}$ – $S_{\text{AL}} = 289 \text{ m}^2/\text{g}$ – $V_{\text{Total,pore}} = 0.390 \text{ cm}^3/\text{g}$



Scheme 43: Synthesis of [4+3] framework.

Synthesis of [4+3] NER polymer framework: The porous polymer framework was prepared by multiple nitroxide exchange reaction of the Tri-NO (1.00 equiv., 0.038 mmol) and the Tetra-AA (0.75 equiv., 0.028 mmol) in 0.9 mL of a toluene/methanol-mixture (9/1). The solvent mixture was freeze-dried before use and added to the starting materials under oxygen free conditions in a glovebox. The vial was sealed and placed in an oven for 24 h at 100 °C. The crude product was washed five times with toluene to remove the *in-situ* released TEMPO product during thermolysis/nitroxide exchange of alkoxyamines. After washing, the polymer framework was dried with a critical point dryer using supercritical CO₂ to give 13.0 mg (0.008 mmol) of a pale beige product. – Yield: 29%

IR: $\nu_{\max}/\text{cm}^{-1}$ 2970 (asym. aliphatic-CH₃), 2927, 2871 (sym. aliphatic-CH₃), 2363, 2362, 1685, 1577 (CONH), 1359 (NO), 1267, 1162 (C-C), 1119 (1,4 aryl-CH), 1065, 1002 (1,3 aryl-CH), 977 (1,3,5 aryl-CH), 878, 824 (1,3,5 aryl-CH). – $S_{\text{BET}} = 116 \text{ m}^2/\text{g}$ – $S_{\text{L}} = 205 \text{ m}^2/\text{g}$ – $V_{\text{Total,pore}} = 0.224 \text{ cm}^3/\text{g}$

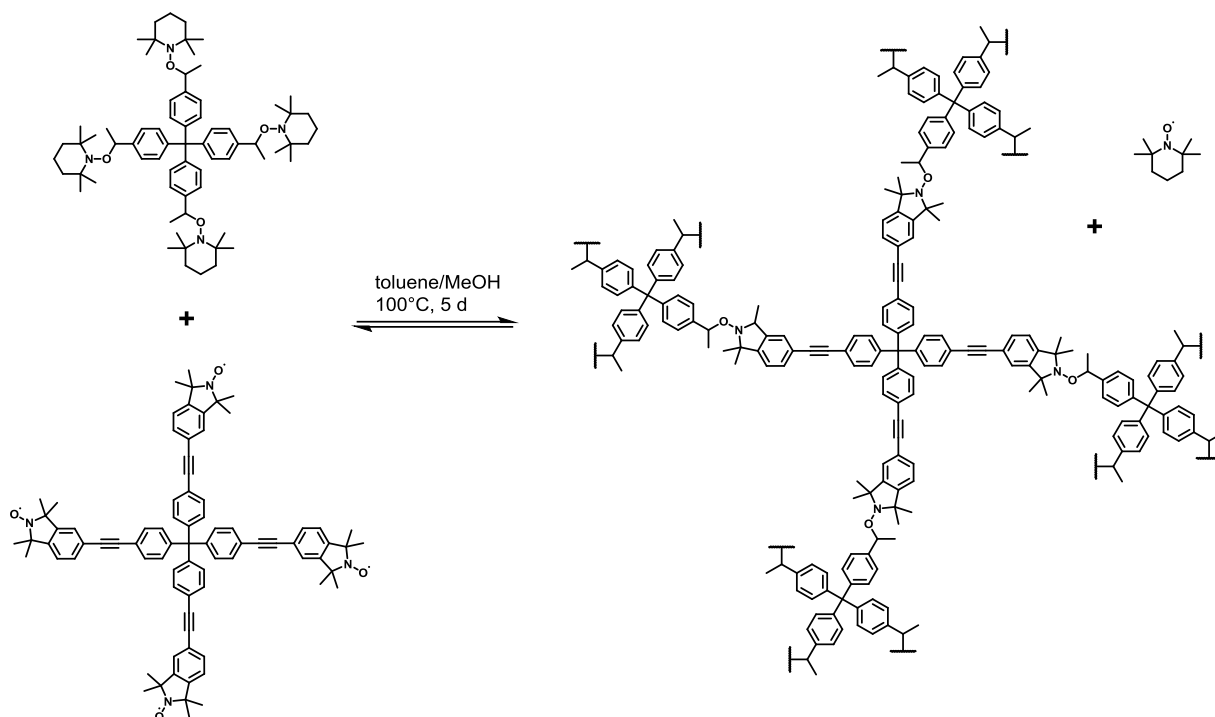


Scheme 44: Synthesis of [4+4C] framework.

Synthesis of [4+4C] NER polymer framework: The porous polymer framework was prepared by multiple nitroxide exchange reaction of the Tetra-[C]-NO (1.00 equiv., 0.028 mmol) and the Tetra-AA (1.00 equiv., 0.028 mmol) in 0.9 mL of a toluene/methanol-mixture (9/1). The solvent mixture was freeze-dried before use and added to the starting materials under oxygen free conditions in a glovebox. The vial was sealed and placed in an oven for 24 h at 100 °C. The crude product was washed five times with toluene to remove the *in-situ* released TEMPO product during thermolysis/nitroxide exchange of alkoxyamines. After washing, the polymer framework was dried with a critical point dryer using supercritical CO₂ to give 20.2 mg (0.01 mmol) of a pale beige product. – Yield: 41%

IR: $\nu_{\max}/\text{cm}^{-1}$ 2975 (asym. aliphatic-CH₃), 2929, 2863 (sym. aliphatic-CH₃), 2122, 2089, 1684, 1604 (CONH), 1360 (NO), 1270, 1188 (C-C), 1122 (1,4 aryl-CH), 1004 (1,3 aryl-CH), 877, 824 (1,3,5 aryl-CH).

– $SA_{\text{BET}} = 923 \text{ m}^2/\text{g}$ – $SA_{\text{L}} = 1114 \text{ m}^2/\text{g}$ – $V_{\text{Total,pore}} = 1.603 \text{ cm}^3/\text{g}$



Scheme 45: Synthesis of [4+4S] framework.

Synthesis of [4+4S] NER polymer framework: The porous polymer framework was prepared by multiple nitroxide exchange reaction of the Tetra-[S]-NO (1.00 equiv., 0.028 mmol) and the Tetra-AA (1.00 equiv., 0.028 mmol) in 0.9 mL of a toluene/methanol-mixture (9/1). The toluene/methanol bi-solvent system proved as the most effective among the solvents evaluated. The solvent mixture was freeze-dried before use and added to the starting materials under oxygen free conditions in a glovebox. The vial was sealed and placed in an oven for 24 h at 100 °C. The crude product was washed five times with toluene to remove the *in-situ* released TEMPO product during thermolysis/nitroxide exchange of alkoxyamines. After washing, the polymer framework was dried with a critical point dryer using supercritical CO₂ to give 14.8 mg (0.009 mmol) of a slightly yellow product. – Yield: 33%

IR: $\nu_{\max}/\text{cm}^{-1}$ 2974 (asym. aliphatic-CH₃), 2926, 2864 (sym. aliphatic-CH₃), 2361, 2339, 1685, 1578 (CONH), 1360 (NO), 1266, 1162 (C-C), 1067 (1,4 aryl-CH), 1017, 887, 824; – $S_{\text{ABET}} = 1150 \text{ m}^2/\text{g}$ – $S_{\text{AL}} = 1868 \text{ m}^2/\text{g}$ – $V_{\text{Total,pore}} = 4.002 \text{ cm}^3/\text{g}$

3.6 Synthesis of thiol-yne coupling thin film

Self-assembled monolayer (SAM) preparation: For SAM formation, a clean gold substrate (2.2 cm × 2.2 cm) was rinsed with absolute ethanol and then immersed in a solution of 11-thioacetyl undecanic-propargyl amide (with a concentration of 1 mmol/L) in ethanol for 18 h. Afterwards the substrate was taken out, rinsed thoroughly with ethanol and dried in a nitrogen stream.

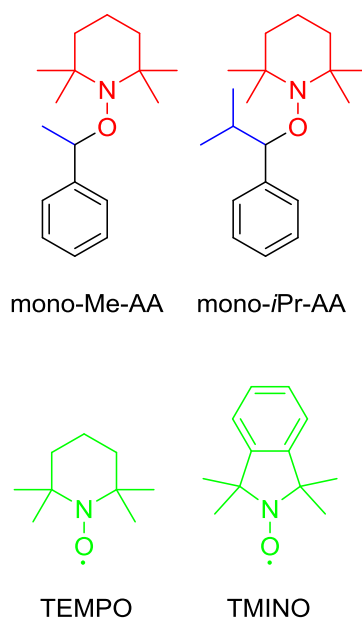
Synthesis of Conjugated Microporous Polymer (CMP) films: 6.7 mg of tetrakis(4-thiolphenyl)-methane (TPM-thiol) (15.0 μmol, 1.00 equiv.), 6.3 mg of tetrakis(4-ethynyl-phenyl)methane (TPM-alkyne) (15.0 μmol, 1.00 equiv.) and 1.1 mg of 2-hydroxy-4'-(2-hydroxyethoxy)-2-methylpropanone (5 μmol, 0.333 equiv.) as photoinitiator were separately dissolved in 20 mL abs. THF. The synthesis was carried out under inert conditions using an argon atmosphere. At first, 1 mL of TPM-thiol solution and 0.5 mL of the photoinitiator solution were added to the SAM coated substrate and stirred gently to ensure proper mixing. Then the mixture was exposed to 365 nm UV-light for 3 minutes. Afterwards, the substrate was rinsed with dry THF. Subsequently, 1 mL of TPM-alkyne solution and 0.5 mL of the photoinitiator solution were added to the substrate and stirred gently to ensure proper mixing. Then the mixture was exposed to 365 nm UV-light for 3 minutes. Then, the substrate was again rinsed with dry THF. The procedure was then repeated for the next reagent 20 times each. After the cycles were completed, the wafer was taken out of the inert environment, washed thoroughly with dry THF and ethanol and then dried using a nitrogen stream.

Transfer of CMP nanomembranes: To obtain freestanding nanomembranes, the CMP-films were grown on sacrificial substrates using the above described procedure. The membrane was then obtained by following a procedure described in literature.^[93] First PMMA was spin coated as a supporting layer. Then, the mica was removed by floating in solutions of I₂/KI/H₂O; KI/H₂O and in the last step by immersing the substrate in H₂O. The retaining gold film was etched in a solution of I₂/KI/H₂O. The membrane was washed 3 times with water.^[93] Then the membrane was transferred to Cu-TEM grids. The obtained membrane size was 0.3 cm × 0.3 cm.

Preparation of freestanding nanomembranes: To obtain freestanding nanomembranes, the CMP-films were grown on sacrificial substrates using the above described procedure. The membrane was then obtained by following a procedure described in literature^[94]: First PMMA/PS was spin coated as a supporting layer and afterwards rinsed overnight in cyclohexane to remove the polystyrene. Then, the mica was removed by floating in solutions of I₂/KI/H₂O; KI/H₂O and in the last step by immersing the substrate in H₂O. The retaining gold film was etched in a solution of I₂/KI/H₂O. The membrane was washed 3 times with water.^[93] Afterwards the membrane was transferred to either a glass slide or a gold coated Si-wafer. The obtained membrane^[93] size was 2 cm × 2 cm.

3.7 Investigation of side group effect from alkoxyamine via EPR spectroscopy

For the side group investigation, mono-Me-alkoxyamine and mono-*i*Pr-alkoxyamine were used for the exchange reaction with tetramethyl isoindoline nitroxide (abbreviated as TMINO). Except TEMPO nitroxide, all three compounds were synthesized and provided by Yannick Matt, from the group of Prof. Stefan Bräse (IOC/KIT).

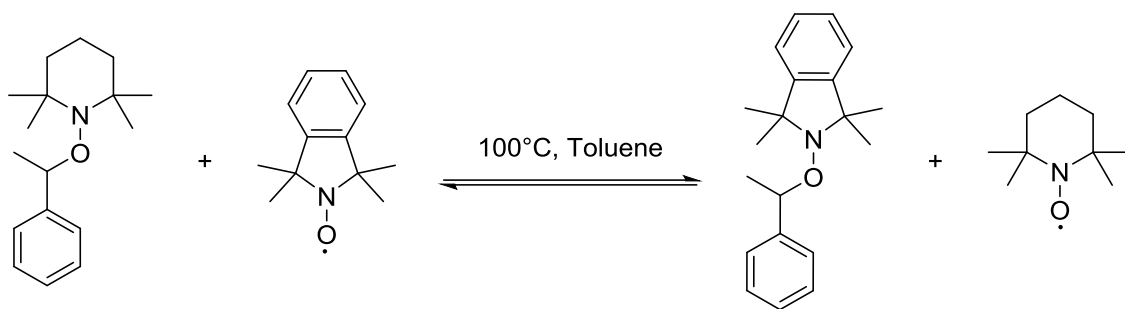


Scheme 46: Alkoxyamines and Nitroxides used in the nitroxide exchange library.

50 mL of stock solutions from each alkoxyamines and nitroxides were prepared in oxygen free toluene with concentration of 1 mM. The oxygen free toluene was degassed by freeze pump thaw prior use. All sample preparation prior heating was proceeding in the glovebox to prevent the presence of oxygen in the reaction mixture.

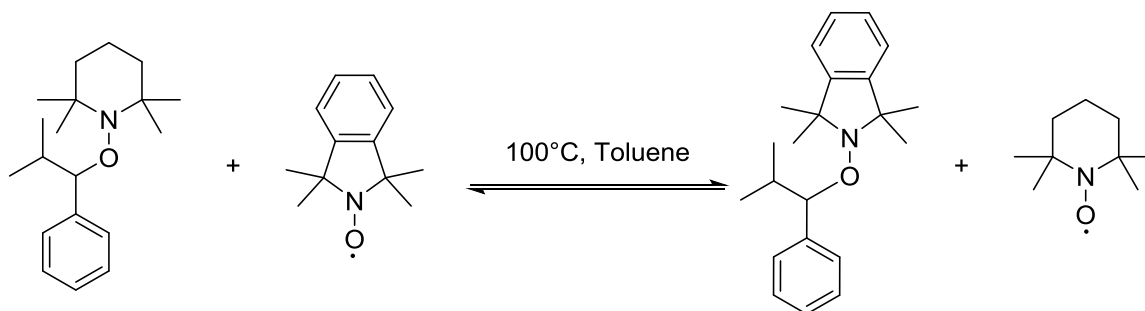
Table 2: List of all used alkoxyamine and nitroxide

	M [g/mol]	n [mmol]	m [g]
mono-Me-AA	261.41	0.05	0.01307
mono-<i>i</i>Pr-AA	289.46	0.05	0.01447
TEMPO	156.25	0.05	0.00781
TMINO	190.27	0.05	0.00951



Scheme 47: Exchange reaction between mono-Me-AA and TMINO.

1 mL of a 1 mM mono-Me-AA solution was mixed together in a glass vial with 1 mL of a 1 mM TMINO solution and sealed under inert atmosphere. Several of these mixtures were then put into the oven at elevated temperature for following times: 15 min, 1 h, 2 h, 17 h, 48 h, 96 h, 144 h. After reaching the required time for the respective vial it was removed from the oven and EPR was measured immediately.



Scheme 48: Exchange reaction between mono-iPr-AA and TMINO.

1 mL of a 1 mM mono-iPr-AA solution was mixed together in a glass vial with 1 mL of a 1 mM TMINO solution and sealed under inert atmosphere. Several of these mixtures were then put into the oven at elevated temperature for following times: 15 min, 1 h, 2 h, 17 h, 48 h, 96 h, 144 h. After reaching the required time for the respective vial it was removed from the oven and EPR was measured immediately.

3.8 Synthesis of crosslinked polystyrene via nitroxide exchange reaction

Synthesis of Di-PS: 5.52 mL styrene (200.00 equiv., 48.0 mmol, 5.00 g) were given to a Schlenk tube with 0.106 g di-fold-alkoxyamine (1.00 equiv., 0.24 mmol). The mixture was stirred at 130°C for 30 h. The crude product was dissolved with 10 mL THF and precipitated into 100 mL MeOH. The precipitate was then collected and dried to give the desired di-poly(n-styrene) as a white solid. (3.34 g, 66.8 % yield) $M_n = 18230$ g/mol; PDI=1.11.

^1H – NMR (400 MHz, CDCl_3): δ (ppm) = 1.23 - 1.54 (m, CH_3), 1.68 – 2.02 (m, CH_2), 6.32 – 6.71 (m, CH_{Ar}), 6.85 – 7.24 (m, CH_{Ar}). ATR-IR: $\tilde{\nu}$ (cm^{-1}) = 3082 (aromatic C-H), 3060 (aromatic C-H), 3025 (aromatic C-H), 2921 (asymmetric aliphatic CH_2), 2850 (symmetric aliphatic CH_2), 1600 , 1492 (aromatic C-C), 1451 (aromatic C-C), 1373 (deformation C-H), 1069 (in-place aromatic C-H), 1027 (in-plane aromatic C-H), 905 (out-of-plane deformation C-H), 754 (out of plane aromatic C-H), 695(out-of-plane ring deformation), 538 (out-of-plane ring deformation).

Synthesis of Di-PS: 3.21 mL styrene (800.00 equiv., 28.0 mmol, 2.91 g) were given to a Schlenk tube with 0.016 g di-fold-alkoxyamine (1.00 equiv., 0.035 mmol). The mixture was stirred at 130°C for 30 h. The crude product was dissolved with 10 mL THF and precipitated into 100 mL MeOH. The precipitate was then collected and dried to give the desired di-poly(n-styrene) as a white solid. (2.05 g, 70.4 % yield) $M_n = 39670$ g/mol; PDI=1.15.

^1H – NMR (400 MHz, CDCl_3): δ (ppm) = 1.27 - 1.54 (m, CH_3), 1.74 – 2.03 (m, CH_2), 6.35 – 6.76 (m, CH_{Ar}), 6.89 – 7.20 (m, CH_{Ar}). ATR-IR: $\tilde{\nu}$ (cm^{-1}) = 3082 (aromatic C-H), 3060 (aromatic C-H), 3025 (aromatic C-H), 2921 (asymmetric aliphatic CH_2), 2850 (symmetric aliphatic CH_2), 1600 , 1492 (aromatic C-C), 1451 (aromatic C-C), 1373 (deformation C-H), 1069 (in-place aromatic C-H), 1027 (in-plane aromatic C-H), 905 (out-of-plane deformation C-H), 754 (out of plane aromatic C-H), 695(out-of-plane ring deformation), 538 (out-of-plane ring deformation).

Synthesis of Tri-PS: 5.52 mL styrene (300.00 equiv., 48.0 mmol, 5.00 g) were given to a Schlenk tube with 0.150 g tri-fold-alkoxyamine (1.00 equiv., 0.16 mmol). The mixture was stirred at 130°C for 30 h. The crude product was dissolved with 10 mL THF and precipitated into 100 mL MeOH. The precipitate was then collected and dried to give the desired di-poly(n-styrene) as a white solid. (3.74 g, 74.8 % yield) $M_n = 19360$ g/mol; PDI=1.09.

^1H – NMR (400 MHz, CDCl_3): δ (ppm) = 1.27 - 1.53 (m, CH_3), 1.75 – 2.04 (m, CH_2), 6.32 – 6.76 (m, CH_{Ar}), 6.89 – 7.24 (m, CH_{Ar}). ATR-IR: $\tilde{\nu}$ (cm^{-1}) = 3082 (aromatic C-H), 3060 (aromatic C-H), 3025 (aromatic C-H), 2921 (asymmetric aliphatic CH_2), 2850 (symmetric aliphatic CH_2), 1600 , 1492 (aromatic C-C), 1451

(aromatic C-C), 1373 (deformation C-H), 1069 (in-plane aromatic C-H), 1027 (in-plane aromatic C-H), 905 (out-of-plane deformation C-H), 754 (out of plane aromatic C-H), 695(out-of-plane ring deformation), 538 (out-of-plane ring deformation).

Synthesis of Tri-PS: 2.41 mL styrene (600.00 equiv., 21.0 mmol, 2.18 g) were given to a Schlenk tube with 0.033 g tri-fold-alkoxyamine (1.00 equiv., 0.035 mmol). The mixture was stirred at 130°C for 30 h. The crude product was dissolved with 10 mL THF and precipitated into 100 mL MeOH. The precipitate was then collected and dried to give the desired di-poly(n-styrene) as a white solid. (1.81 g, 83.2 % yield) $M_n = 15120$ g/mol; PDI=1.30.

^1H – NMR (400 MHz, CDCl_3): δ (ppm) = 1.25 - 1.55 (m, CH_3), 1.74 – 2.06 (m, CH_2), 6.30 – 6.72 (m, CH_{Ar}), 6.87 – 7.22 (m, CH_{Ar}). ATR-IR: $\tilde{\nu}$ (cm^{-1}) = 3082 (aromatic C-H), 3060 (aromatic C-H), 3025 (aromatic C-H), 2921 (asymmetric aliphatic CH_2), 2850 (symmetric aliphatic CH_2), 1600, 1492 (aromatic C-C), 1451 (aromatic C-C), 1373 (deformation C-H), 1069 (in-plane aromatic C-H), 1027 (in-plane aromatic C-H), 905 (out-of-plane deformation C-H), 754 (out of plane aromatic C-H), 695(out-of-plane ring deformation), 538 (out-of-plane ring deformation).

Crosslinking of Di-PS with Tetra-[C]-NO: 0.15 g Di-PS (2.00 equiv., 0.0095 mmol) and 0.0064 g Tetra-[C]-NO (1.00 equiv., 0.0047 mmol) were given to a Schlenk tube with toluene. The mixture was stirred at 130°C for 48 h. The crude product was dissolved in 10 mL THF to remove the unreacted Di-PS. After centrifugation, the precipitate was collected and dried as a black powder. (0.03 g, 19.7 % yield)

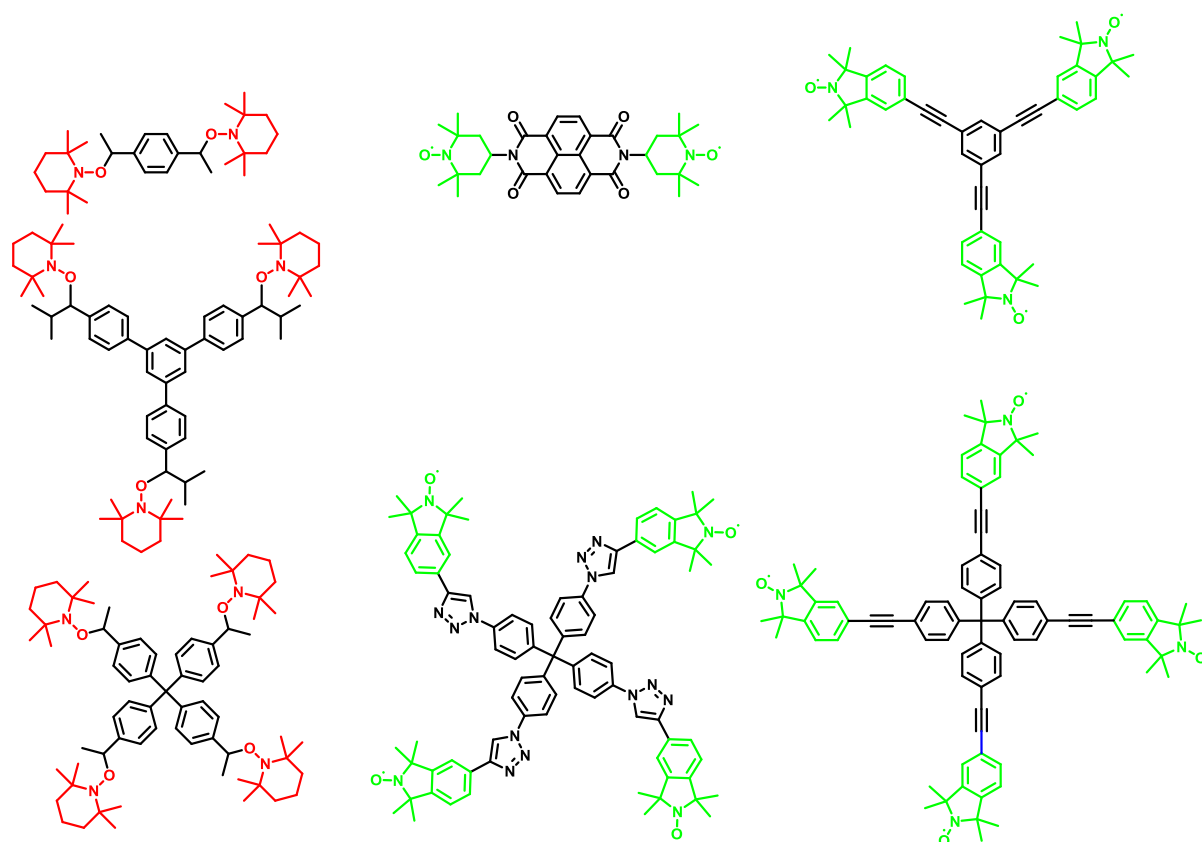
ATR-IR: $\tilde{\nu}$ (cm^{-1}) = 3082 (aromatic C-H), 3060 (aromatic C-H), 3025 (aromatic C-H), 2921 (asymmetric aliphatic CH_2), 2850 (symmetric aliphatic CH_2), 1600, 1510, 1492 (aromatic C-C), 1451 (aromatic C-C), 1373 (deformation C-H), 1065 (in-plane aromatic C-H), 1015 (in-plane aromatic C-H), 905 (out-of-plane deformation C-H), 833, 754 (out of plane aromatic C-H), 695(out-of-plane ring deformation), 668 (out of plane triazole ring deformation), 538 (out-of-plane ring deformation), 465 (out-of-plane triazole ring deformation).

4. Result

The purpose of this thesis was to investigate the nitroxide exchange reaction (NER) for the synthesis of dynamic organic frameworks. The reason for choosing this reaction is due to their fully reversible nature, where bond breaking and reformation happens concurrently. At elevated temperature, the alkoxyamine cleaves reversibly to a persistent nitroxide radical and a C-centered radical, which can easily recombine again. However, in presence of an additional nitroxide, the recombination occurs not only with the cleaved persistent nitroxide and the C-centered radical, but also with the additional nitroxide. By using multi-fold alkoxyamine and nitroxides, the NER enables the synthesis of a new type of dynamic covalent frameworks. By precise addition or removal of modulating mono-nitroxide (TEMPO), the reaction equilibrium can be precisely controlled. The reaction process as well as the crosslinking degree can be monitored by EPR spectroscopy. Due to the different hyper fine coupling constants, EPR spectroscopy allow the quantitative determination of the ratio between two different nitroxide in solution. By using the solid state EPR, the amount of spins can be quantitatively determined, which can be used for the calculation of the NER framework crosslinking degrees.

In chapter 4.1, the optimization of the reaction conditions for synthesis of NER framework are discussed. In the following chapter 4.2 and 4.3, the synthesized organic frameworks are investigated for their stimuli-responsive behavior at various crosslinking degrees. In chapter 4.4, nitroxide mediated polymerization is combined with NER for further crosslinking of macromolecules. To achieve a better understanding on the reaction kinetic, the exchange reaction between mono isoindoline nitroxide and mono alkoxyamines with Me-, and *i*Pr- side groups were investigated with EPR spectroscopy, described in chapter 4.5. In the following chapter 4.6, the nitroxide exchange reaction employing layer-by-layer method to synthesize organic thin film will be discussed. In chapter 4.7, the development of fast and efficient light induced layer-by-layer was investigated with thiol-yne coupling (TYC) reaction as model system.

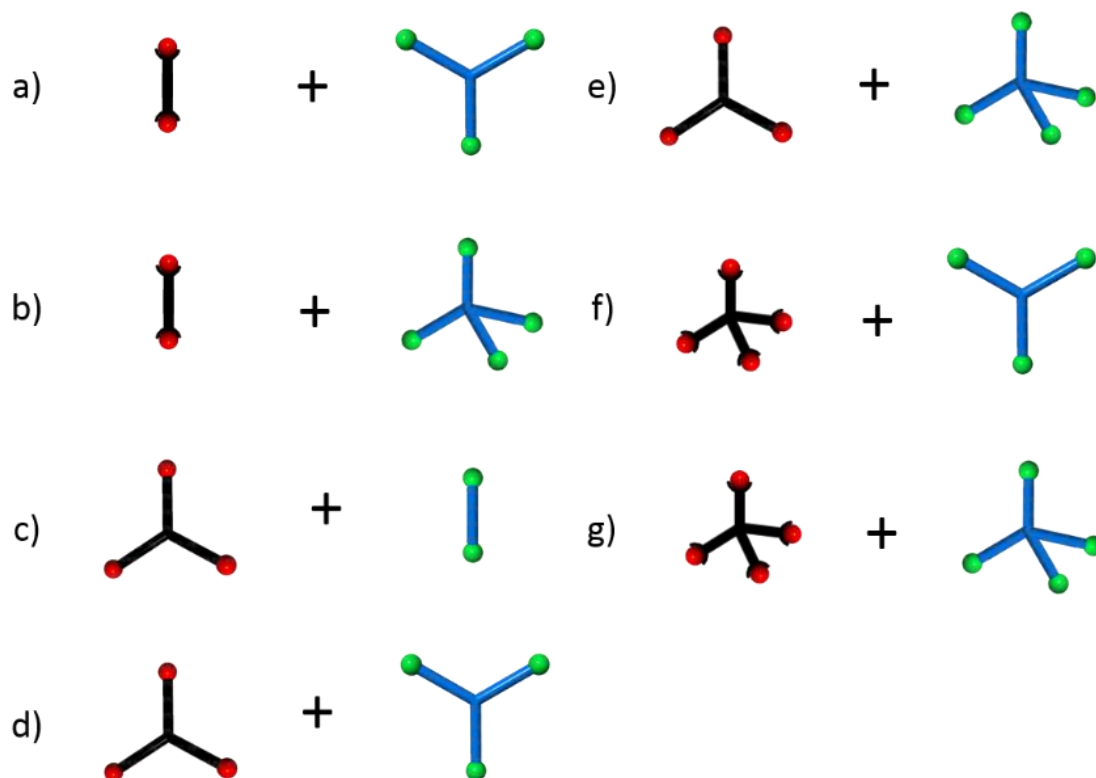
4.1 Optimization of the reaction condition for the synthesis of organic framework via nitroxide exchange reaction



Scheme 49: Multifold alkoxyamines and multifold nitroxides used for the synthesis of nitroxide exchange framework.

Based on the in Scheme 49 listed molecular building blocks, various combinations of different molecular building blocks for the synthesis of organic frameworks were screened. To simplify the nomenclature, alkoxyamines are abbreviated as AA and based on the number of the active functional group specified as Di-, Tri- and Tetra-AA. The nitroxides are treated in the same way, with NO being used as abbreviation. Overall nine different combinations of multivalent nitroxide and multivalent alkoxyamines are investigated. For the optimization of the reaction condition, most systems are screened with different solvent mixtures and concentrations (Scheme 50).

In Scheme 50, all alkoxyamines are drawn in black with the nitroxide functionalities as red balls. All multivalent nitroxide building blocks are drawn in blue, with the nitroxide functionalities drawn in green. Schematically the red nitroxides are exchanged by the green nitroxides during the NER. There are two types of Tetra-NO, the first one is synthesized via CuAAC and is abbreviated as Tetra-[C]-NO, while the second one is synthesized via Sonogashira cross coupling and abbreviated as Tetra-[S]-NO.



Scheme 50: Combination of different molecular building blocks used in the synthesis of nitroxide exchange frameworks.

The solvent mixture shown in Table 3 was chosen due to their different relative polarity, relatively high boiling point and solubility. Due to the low boiling point of acetone and methanol in comparison to anisole, dioxane, mesitylene and toluene, they were only used as 10% volume ratio in the solvent mixture. All solvent mixtures were degassed over freeze-pump-thaw to prevent side reaction with oxygen. For a theoretically fully crosslinked framework, all combinations were in a 1:1 ratio regarding the active functional group.

First, the combination of Di-AA and Tri-NO was tested. Since this combination did not precipitate in all solvent mixtures at a concentration of 0.042 mol/L for Tri-NO in the reaction mixture. Therefore, the concentration was increased to 0.42 mol/L for Tri-NO. However, even at higher concentration, no precipitation was observed after 5 days at 100°C. The combination of Tri-AA and Di-NO as well did not precipitate at the previous chosen reaction conditions.

It is assumed, that the reason for the absence of precipitation is caused by the specific geometry of the reacting building blocks. In theory, the combination of Di-AA with Tri-NO and Tri-AA with Di-NO should form sheet-like structures analog to 2D-COFs. However, due to the fact, that the organic building blocks are not planar, no adequate π - π stacking can occur.

Therefore, the strategy was changed and the reaction of divalent alkoxyamine with tetravalent nitroxide was tested. After 5 days at 100°C, we could obtain in all eight solvent mixtures precipitation

which were insoluble in all tested solvents. The different solvent mixtures differed only by their yield of precipitated solid. Among all solvent mixtures, toluene/MeOH (9/1) gave the highest yield of 47 %, while the rest yielded less than 15 %.

Table 3: Solvent screening. Coloring: Red no precipitation, Green precipitation, yellow not yet tested.

	Di-AA + Tri-NO	Di-AA + Tetra-[C]-NO	Tri-AA + Di-NO	Tri-AA + Tri-NO	Tri-AA + Tetra-[C]-NO	Tri-AA + Tetra-[S]-NO	Tetra-AA + Tetra-[C]-NO	Tetra-AA + Tetra-[S]-NO
mesitylene/dioxane 1:1	No	Yes	No	-	Yes	-	-	-
anisole/dioxane 1:1	No	Yes	No	-	Yes	-	-	-
toluene/dioxane 1:1	No	Yes	No	-	Yes	-	-	-
mesitylene/MeOH 9:1	No	Yes	No	-	Yes	-	-	-
mesitylene/acetone 9:1	No	Yes	No	-	Yes	-	-	-
anisole/dioxane 9:1	No	Yes	No	-	Yes	-	-	-
anisole/acetone 9:1	No	Yes	No	-	Yes	-	-	-
toluene/MeOH 9:1	No	Yes	No	Yes	Yes	Yes	Yes	Yes

Using same solvent mixtures, the combination of Tri-AA and Tetra-[C]-NO was also investigated. After 5 days at 100°C, precipitation could be obtained in all eight solvent mixtures. The yield of the insoluble precipitation varied also in this case. In Table 3, all yields which are above 40 % are shown. Among all eight solvent mixtures, toluene/MeOH (9/1) was optimized to gave the highest yield of 63 %. The solvent mixture, which are not listed in Table 4 have all the yield below 20%.

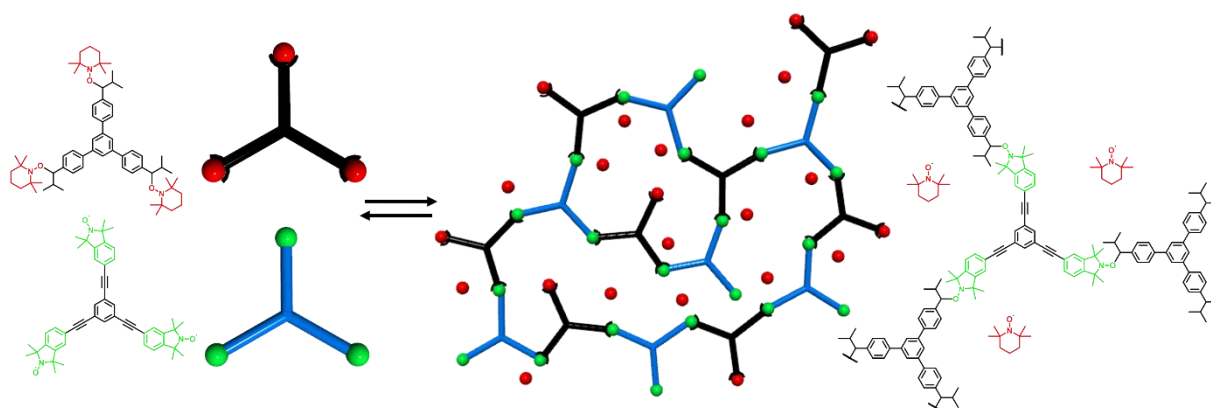
Table 4: Yield of nitroxide exchange frameworks from Tri-AA with Tetra-[C]-NO.

	mesitylene/dioxane 1:1	anisole/dioxane 1:1	toluene/dioxane 1:1	toluene/MeOH 9:1
Yield [%]	41	50	47	63

Due to the limited amount of remaining building blocks, the toluene/MeOH 9:1 mixture was chosen for the remaining combinations. The organic frameworks yielded applying the reaction conditions as mentioned in d), f) and e) with Tetra-[S]-NO form gels. In chapter 4.2, detailed investigation of the stimuli responsive and self-healing properties of those gels are described. The organic frameworks obtained from the reaction conditions b), e) with Tetra-[C]-NO and g) with Tetra-[C]-NO as well as Tetra-[S]-NO formed porous organic polymers with high BET surface areas of up to 1200 m²/g, which is described in 4.3 in detail.

4.2 Synthesis of stimuli responsive self-healable organic framework

For the synthesis of dynamic covalent frameworks, Tri-AA and Tri-NO were dissolved in a toluene/methanol-mixture (9/1). Heating of the mixture induces a reversible cleavage of the C–O bond from Tri-AA and leads to generate persistent nitroxide radicals (TEMPO) and transient C-centered radicals. Transient C-centered radicals spontaneously form new bonds with the Tri-NO, which enables the formation of polymeric network structures (Scheme 51).



Scheme 51: Molecular structures and schematic representation of the [3+3] organic framework via nitroxide exchange reaction.^[95] Reproduced from Ref. 95 with permission from The Royal Society of Chemistry.

The radical character of this reaction mechanism allows the investigation of the reaction process through EPR spectroscopy, due to the different hyperfine coupling constants of the involved nitroxides. The samples were taken during the reaction after certain time intervals and analyzed by EPR spectroscopy. As a reference, the EPR spectra of the pure Tri-NO and of TEMPO (2,2,6,6-tetramethylpiperidinyloxy radical) were measured, which have a hyperfine coupling constant of 14.1 G and 15.5 G (Figure 1 a and e), respectively.

In Figure 1, the EPR spectra of the reaction mixture after heating at 100 °C for 1 h, 2 h and 5 h, 8 h and the two references are shown. The progress of the exchange reaction was clearly shown due to the decrease of the relative intensity of Tri-NO and the increase of the relative intensity of the liberated TEMPO.

Table 5: Ratio of TEMPO and TriNO at 1 h, 2 h and 5 h.

	Tri-[S]-NO	1 h	2 h	5 h	TEMPO
TEMPO [%]	0	37.1	60.0	76.0	100
Tri-[S]-NO [%]	100	62.9	40.0	24.0	0

By fitting of the spectra with the program Xenon, we could obtain the different relative intensities of the two species as depicted in the bar chart of Figure 1 with the red bar representing TEMPO and the green bar representing Tri-NO. The reaction process reaches after 1 h 37% and after 2 h 60% of exchanged TEMPO. After 5 h, 76 % of TEMPO are exchanged, which prove a successful homolysis of the C–O-bond of the Tri-AA, followed by formation of a new C–O-bond between the Tri-NO and the C-centered radical formed by the Tri-AA. The ratio of both nitroxides is shown listed in Table 5. After further heating, the reaction mixture converted into a gel. Due to the low mobility of the nitroxide moieties within the organic framework, the EPR spectrum of the gel after 8 h (Figure 1 f) does not show a hyper fine coupling anymore. The reaction mixture was further heated up to 24 h to ensure the reaction equilibrium. After washing and drying of the sample we obtained the final organic framework with a yield of 95%.

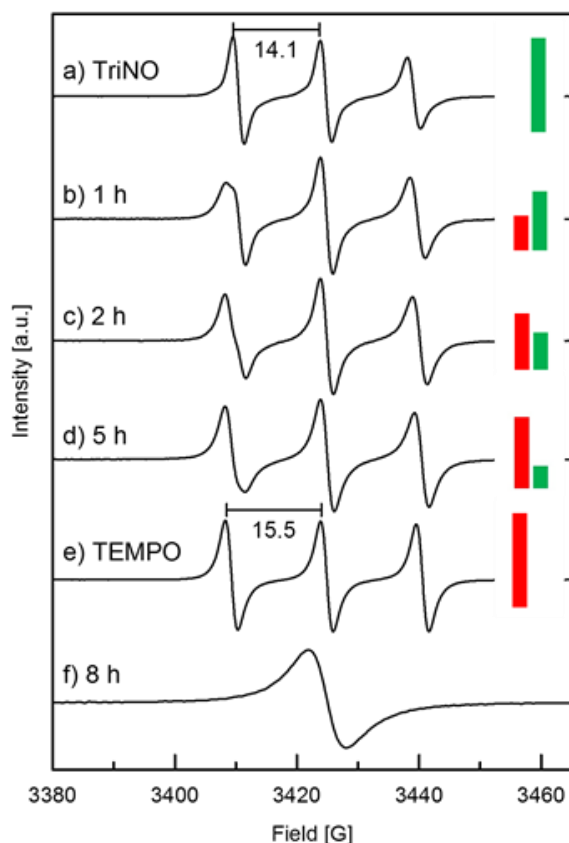


Figure 1: Investigation of the reaction process via EPR spectroscopy; a) reference spectrum of the Tri-NO 4; EPR spectra of the reaction mixture after b) 1 h, c) 2 h, d) 5 h; e) reference spectrum of the by-product TEMPO and f) solid EPR spectrum of the network product.^[95] Reproduced from Ref. 95 with permission from The Royal Society of Chemistry.

As described in chapter 1.2, the by-product (TEMPO nitroxide) obtained during the reaction, is in competition with the nitroxide moieties of the Tri-NO to trap the *in situ* formed C-centered radicals. Even if the equilibrium is reached, the organic framework still bears unreacted functional groups. By washing the network repetitively, TEMPO can be removed selectively from the reaction mixture.

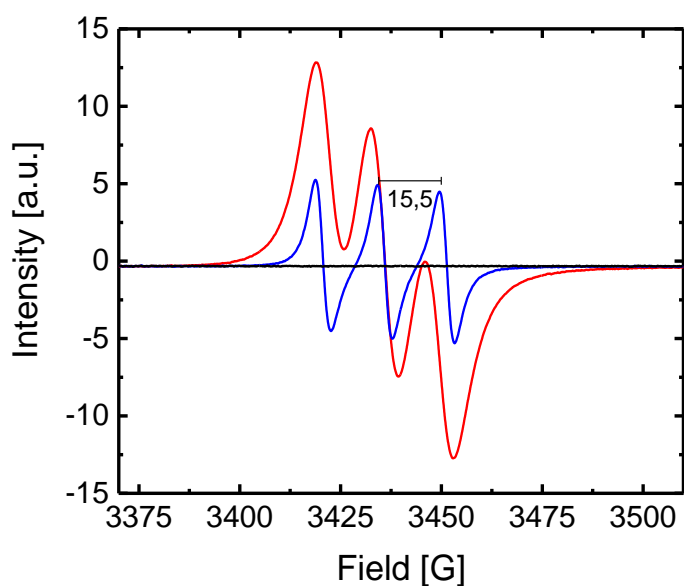


Figure 2: EPR spectra of the washing solution from pristine organic framework: first washing (red), second washing (blue) and fifth washing (black).^[95] Reproduced from Ref. 95 with permission from The Royal Society of Chemistry.

The presence of TEMPO in the washing solution was monitored by EPR. After five washing cycles the amount of TEMPO went below the measurable quantity (Figure 2).

The synthesized organic framework then was investigated with ATR-FT-IR. In the region around 2971 cm^{-1} , and 2871 cm^{-1} , asymmetric and symmetric vibration of aliphatic- CH_3 bond are observed, which originates from the methyl group on the Tri-NO. In the finger print area, the vibration of 1,4 aryl-CH and 1,3,5 aryl-CH can also be identified. Due to the high polarizability of the alkyne group in Tri-NO, this peak can be observed in Raman spectroscopy with high intensity. The peak of N-O at around 1578 cm^{-1} can be observed in IR as well as the Raman spectrum.

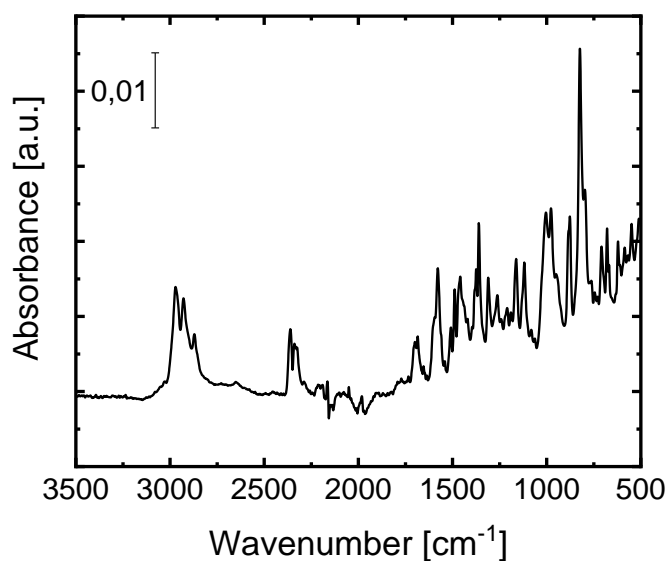


Figure 3: IR spectra of the organic framework from the combination of Tri-AA and Tri-NO.^[95] Reproduced from Ref. 95 with permission from The Royal Society of Chemistry.

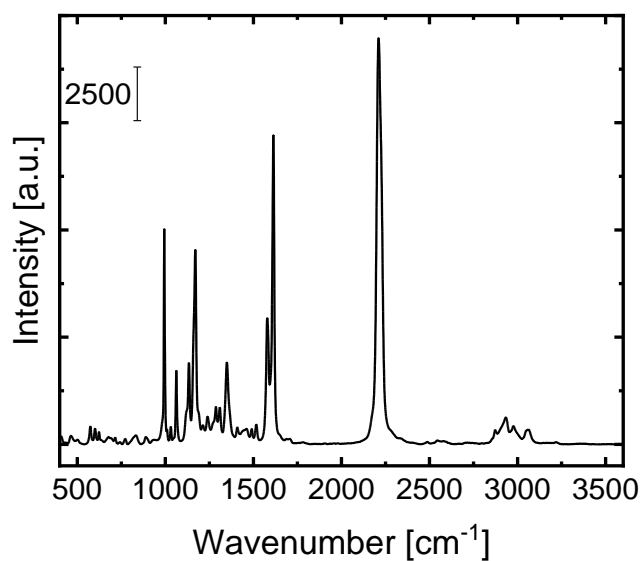


Figure 4: Raman spectra of the organic framework from the combination of Tri-AA and Tri-NO.^[95] Reproduced from Ref. 95 with permission from The Royal Society of Chemistry.

With thermal gravimetric analysis, the thermal stability of this organic framework was investigated. The organic framework was heated from 40 °C to 1000 °C with heating rate of 20 °C per minute. The organic framework is stable until 200 °C, with only a weight loss of around 0.8 %. At around 292 °C the polymer lost 5 % of its initial weight and the thermal decomposition start to take place.

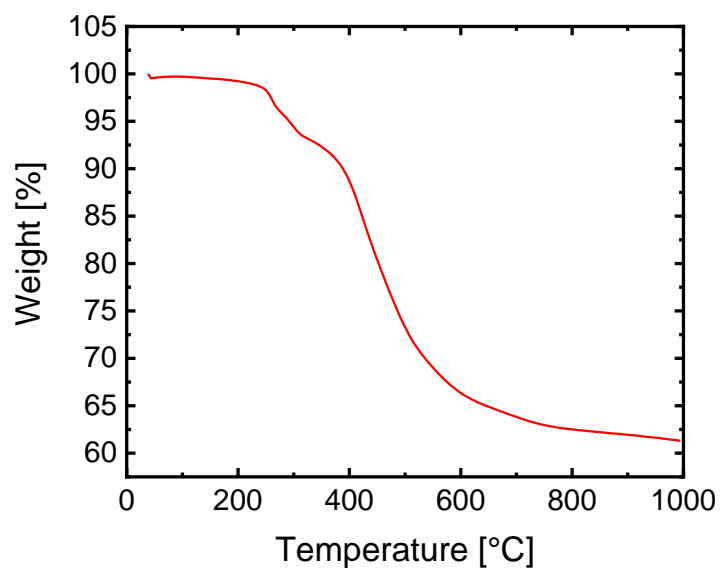


Figure 5: Thermal gravimetric analysis curve of the organic framework.^[95] Reproduced from Ref. 93 with permission from The Royal Society of Chemistry.

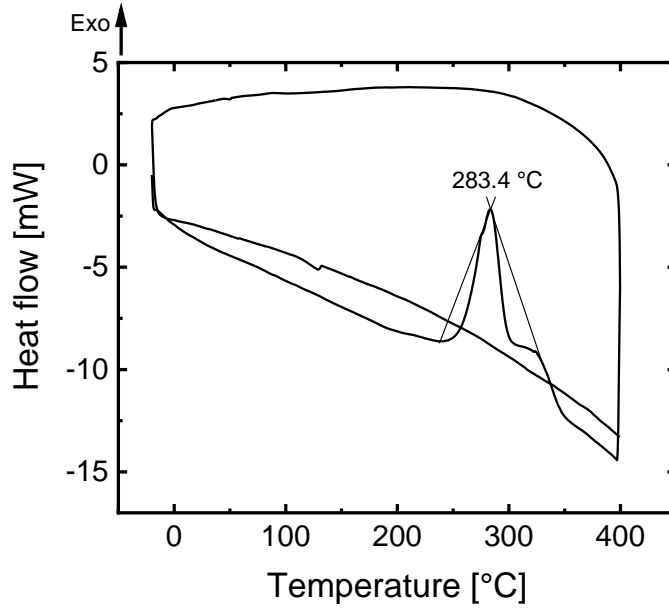


Figure 6: Differential scanning calorimetry curve of the organic framework.

The differential scanning calorimetry (DSC) curve of the organic framework shows while heating cycle a sharp exothermic peak at 283.4 °C, which indicate a cold crystallization procedure. The exothermic peak is followed by a steeply decrease of the heat flow, which indicate a melting of the organic framework. However, while the cooling cycle, no changes was observed. Also, a glass transition point for this organic framework was not observed.

Using EPR spectroscopy, the defect density can be determined. From the defect density, the crosslinking degree (CLD) can be calculated by assuming that a spin density = 0 corresponds to a crosslinking degree of 100%. On the other hand, the spin density of a one-to-one mixture of the starting materials corresponds to a crosslinking degree of 0%.

$$N_s(0\%CL) = \frac{m_p}{M_s} \cdot N_A \cdot 3 \quad (19)$$

$$CLD = 100 - ((N_s(0\%CL) - N_s(x\%CL)) \cdot 100) \quad (20)$$

$N_s(0\%CL)$ is the spin count of the one-to-one mixture of starting material with 0% crosslinking and can be calculated from the employed total mass of the measured polymer m_p , the total molecular weight of employed starting materials M_s and the Avogadro's number N_A . Since the three-fold-nitroxide has three spins, it needs to be multiplied by 3 (equation (19)). $N_s(x\%CL)$ is given through the spin count of the EPR measurement of the measured organic framework. The crosslinking degree CLD is given in percent and can be calculated using the equation (20).

To monitor the crosslinking degree, EPR was used. In the synthesized organic framework, only the leftover isoindoline nitroxide moieties in the defect sites are EPR active, since the by-product (TEMPO) nitroxide were already removed by washing and all alkoxyamine are EPR silent. Therefore, with the determined spin density of the prepared organic framework, we directly know the defect density of the organic framework.

Following the principle of Le Chatelier, removal of one compound changes the state of equilibrium. By this after TEMPO removal, annealing of the washed polymer in fresh toluene at elevated temperature should enable additional crosslinking. Because further reaction between the leftover isoindoline nitroxide moieties with the fresh cleaved C-centered radicals takes place.

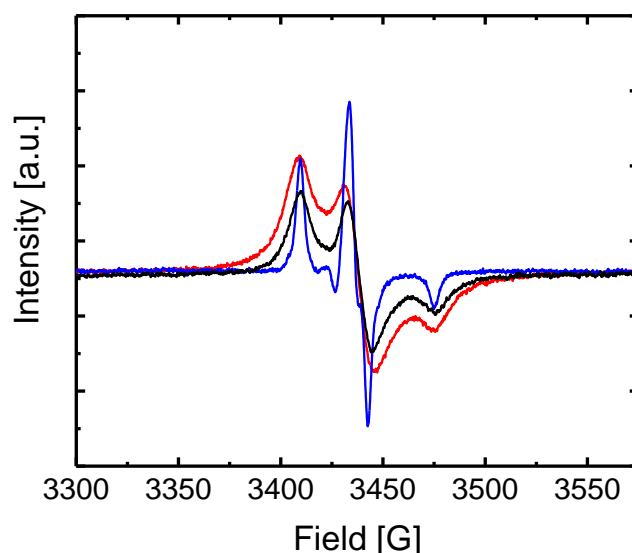


Figure 7: EPR spectra of the initial polymer gel (red), after increasing (blue) and again decreasing (black) the crosslinking degree.^[95] Reproduced from Ref. 95 with permission from The Royal Society of Chemistry.

The EPR spectrum of the pristine organic framework is shown in Figure 7 (red). Compared to the EPR spectrum of Figure 1 f, more defined structure arose from the removal of TEMPO nitroxide from the organic framework during washing. This is because of less spin-spin interactions. Using the equation (20), the crosslinking degree (CLD) of the pristine organic framework was determined to be $95.20 \pm 0.04\%$.

In a first step to tune the crosslinking degree, the washed organic framework was annealed in fresh toluene at 100 °C overnight. Due to the fact, that all free TEMPO units were removed from the solution

before heating, the equilibrium of the system leads to an additional cleavage of the remaining TEMPO units from the organic framework.

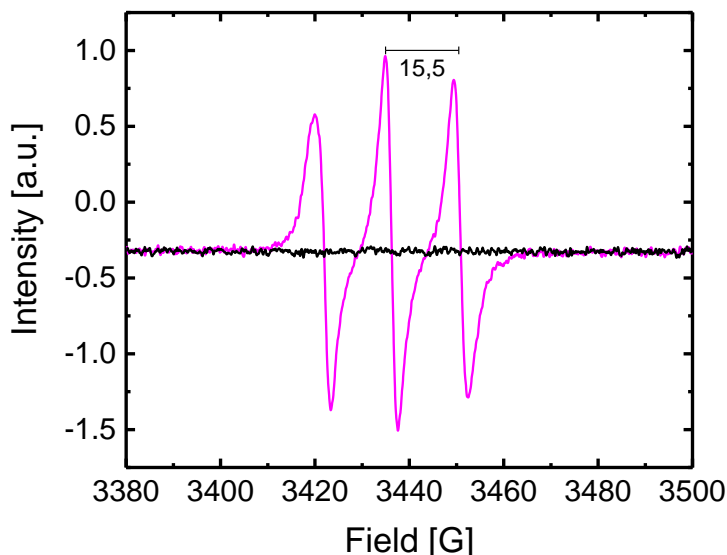


Figure 8: EPR spectra of the solution before annealing (black) and solution after annealing at 100°C (magenta).^[95] Reproduced from Ref. 95 with permission from The Royal Society of Chemistry.

Since all free TEMPO units in solution were removed before heating, the equilibrium of the system leads to an additional displacement of remaining TEMPO units from the organic framework. As expected, the EPR spectrum of the solution after annealing (Figure 8 magenta line), where the annealing of the organic framework took place show a strong TEMPO signal with the characteristic hyperfine coupling constant of 15.5 G. This confirms that remaining TEMPO units were liberated after annealing (Figure 8 black line). The solid state EPR spectra of the organic framework before (Figure 7 red line) and after (Figure 7 blue line) annealing provides the possibilities to investigate the crosslinking degree. The EPR spectrum of the organic framework after annealing (blue in Figure 7) shows a more defined shape as the broadened EPR spectrum of the pristine network (red in Figure 7), indicating a lower local concentration of nitroxide moieties. The crosslinking degree of the annealed organic framework is also calculated using the equation (20) and show an increased from $95.20 \pm 0.04\%$ to $98.94 \pm 0.04\%$.

In the next step, we investigated the possibility to tune the crosslinking degree again by addition of free TEMPO radicals to the organic framework in toluene at 100 °C overnight. The solid state EPR spectrum after this step is shown in Figure 7 (black). The shape of the spectrum was as expected broadened again, which indicates a higher local spin density. Calculated from the spin density, the crosslinking degree was decreased from $98.94 \pm 0.04\%$ to $96.7 \pm 0.02\%$. In Table 6, all crosslinking degrees of the organic framework are listed with corresponding spin density.

Table 6: Calculation of CLD for the organic framework.

	m_p [mg]	M_s [g/mol]	N_s (0%CL)	N_s (x%CL)	CLD [%]
TriNO+TriAA	10.2	1655.39	$1.11 \cdot 10^{19}$	-	0
pristine	2.0	1655.39	$2.18 \cdot 10^{18}$	$1.05 \cdot 10^{17}$	95.20 ± 0.04
annealed	3.1	1655.39	$3.38 \cdot 10^{18}$	$3.57 \cdot 10^{16}$	98.94 ± 0.04
de-crosslinked	5.0	1655.39	$5.46 \cdot 10^{18}$	$1.82 \cdot 10^{17}$	96.7 ± 0.02

In contrast to the EPR investigation, where only the free nitroxide species are EPR active, fluorescence spectroscopy of the network structure presents complementary information, caused by the locally quenched fluorescence by the free nitroxide species. Therefore, a higher crosslinking degree with a lower defect density leads to an increased fluorescence, where a lower crosslinking degree with a higher defect density leads to a decreased fluorescence. In agreement with the EPR investigation, also the fluorescence spectroscopy indicates a reversible tuning of the crosslinking degree.

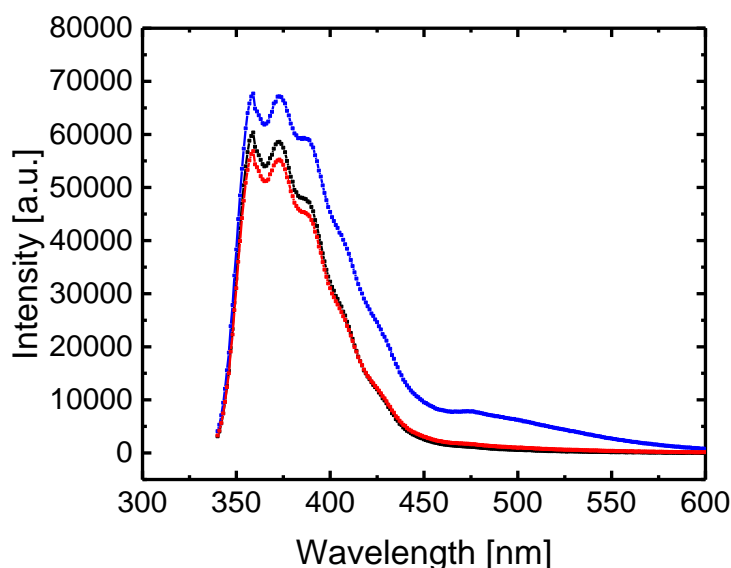


Figure 9: Fluorescence emission spectra of the initial polymer gel (red), after increasing (blue) and again decreasing (black) the crosslinking degree; Bottom.^[95] Reproduced from Ref. 95 with permission from The Royal Society of Chemistry.

Figure 9 shows the fluorescence spectra of the pristine, annealed and de-crosslinked organic framework. All sample were excited at 320 nm. The red curve is the emission spectrum of the pristine polymer gel, which have the lowest fluorescence intensity, followed by a significant increase in fluorescence after annealing (blue) and after de-crosslinking (black) a significant decrease in intensity.

Due to the strong influences of the crosslinking degree on the properties of the organic framework, it is assumed that the mechanical properties or the swelling behavior upon solvent impregnation can be controlled by the reaction equilibrium. To quantify the swelling behavior of the organic framework in

response to the tuned crosslinking degree, the change in swelling degree Q of the pristine, annealed and de-crosslinked organic framework are monitored upon solvent impregnation.

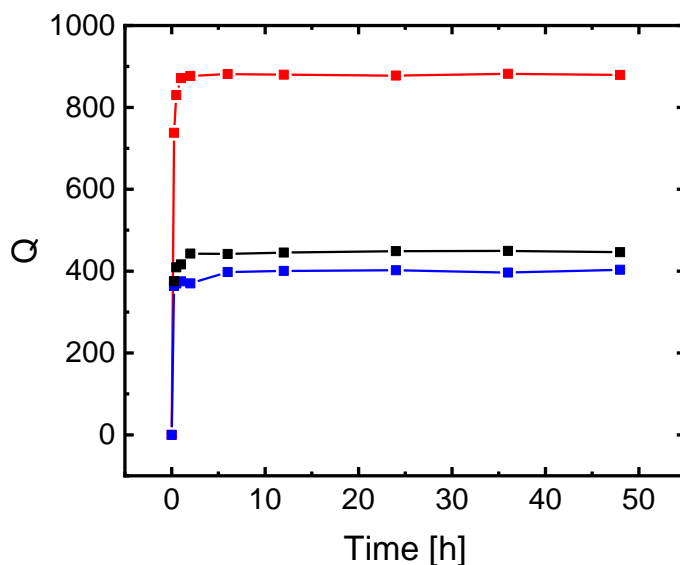


Figure 10: Swelling degree Q in toluene of the initial polymer gel (red), after increasing (blue) and again decreasing (black) the crosslinking degree. The line between the points was added to guide the eye.^[95] Reproduced from Ref. 95 with permission from The Royal Society of Chemistry.

In Figure 10, changes in swelling degree Q for the pristine organic framework (red), after annealing (blue) and after de-crosslinking (black) are shown. In all cases, the swelling degree increase steeply within the first 3 hours and stay nearly constant afterwards. However, the final swelling degree after 48 h of all three states differ strongly from each other. The pristine organic framework shows the highest swelling degree Q of 880. After annealing, the swelling degree decrease strongly to about 400 and increase to 450 after de-crosslinking.

The porosity of the organic framework at pristine, annealed and de-crosslinked states was also investigated via argon adsorption. However, it was proven, that this organic framework has a very low porosity of only $30 \text{ m}^2/\text{g}$. The porosity remains nearly the same and doesn't change significantly after annealing or de-crosslinking. All three states were also investigated with XRD, however it turned out to be not crystalline.

In Table 7, the EPR, fluorescence spectroscopy and swelling degree investigation are summarized. It was shown, that the EPR spectroscopy allows the calculation of the crosslinking degree through the spin count of the sample quantitatively. The determined crosslinking degree via EPR correlates well to the changes in fluorescence intensity during the modification of the equilibrium in the current systems. However, the fluorescence spectroscopy in current system cannot use as a quantitative tool to investigate the crosslinking degree without prior calibration. The modification of the crosslinking

degree and fluorescence intensity agree well with the changes in the physical properties of the organic frameworks. The swelling degree follows the same trend as the defect density and inversely follows the trend of the crosslinking degree.

Table 7: Summary of spin density, crosslinking degree, fluorescence intensity and swelling degree of the organic framework after modulating the equilibrium of the exchange reaction.

	Pristine sample	After annealing	After de-crosslinking
Crosslinking degree [%]	95.20 ± 0.04%	98.94 ± 0.04%	96.67 ± 0.02%
Normalized spin density [a.u.]	1	0.16	0.65
Normalized fluorescence intensity [a.u.]	1	1.22	1.06
Normalized swelling degree (48 h) [Q]	1	0.4	0.5

According to the above described investigations, addition or removal of TEMPO nitroxide to the organic framework can cause a shift of the equilibrium, resulting in changes of the crosslinking degree. By adding an excess amount of TEMPO to the organic framework, the equilibrium should be shifted completely to the side of the starting components resulting to a dissolution of the organic framework.

Indeed, after addition of an excess amount of TEMPO and heating up to 100 °C, the polymer network softened after 3 h. After 6 h, only small pieces remained in the reaction vessel. And the organic framework was completely disassembled into a solution form after 24 h of heating. Figure 11 shows the image of the initial monomer solution (top), the synthesized organic framework (bottom, middle) and the dissolved network (bottom, right). The obtained solution was further analyzed by mass spectrometry. Corresponding masses of the starting precursors could be found during the measurement, which show a successfully recovery of the starting materials.

Due to the reversible and dynamic feature of the nitroxide exchange reaction, it was assumed that this feature will provide the network with self-healing properties. To investigate the self-healing property, the pristine organic framework was cut into two pieces and placed both in contact to each other and heated in toluene for 24 h at 100°C. The first try was not successful, as both pieces moved away from each other during the experiment in the reaction vessel.

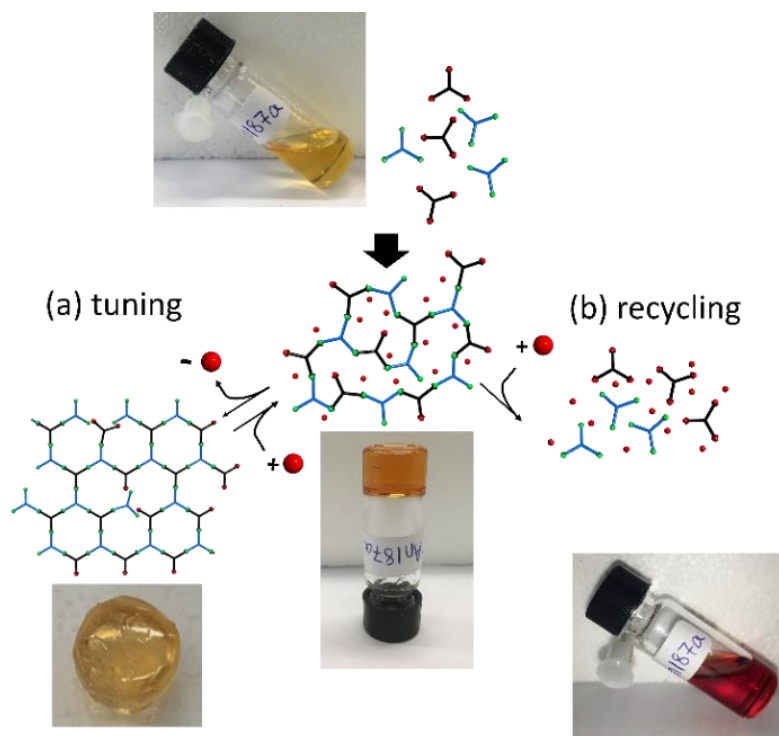


Figure 11: Equilibrium control of the nitroxide exchange reaction. (a) Tuning of the crosslinking degree via addition or removal of TEMPO (red balls); (b) Recycling of the molecular components via addition of a large excess of TEMPO. Images show the initial solution before reaction (top), after gel transition (bottom middle), after annealing (bottom left) and after recycling/dissolving (bottom right).^[95] Reproduced from Ref. 95 with permission from The Royal Society of Chemistry.

In the second experiment, 3 mm glass beads were added around and on top to fix the position of the two pieces and ensure the contact during the experiment, while other reaction condition stay the same. However, with the help of the glass beads contact between the interfaces could be ensured, but the organic framework was only lightly joined to each other. We assume, that both pieces start to anneal in the reaction vessel and the contact interfaces are slightly modified during the annealing, that's why the contact was not strong enough.

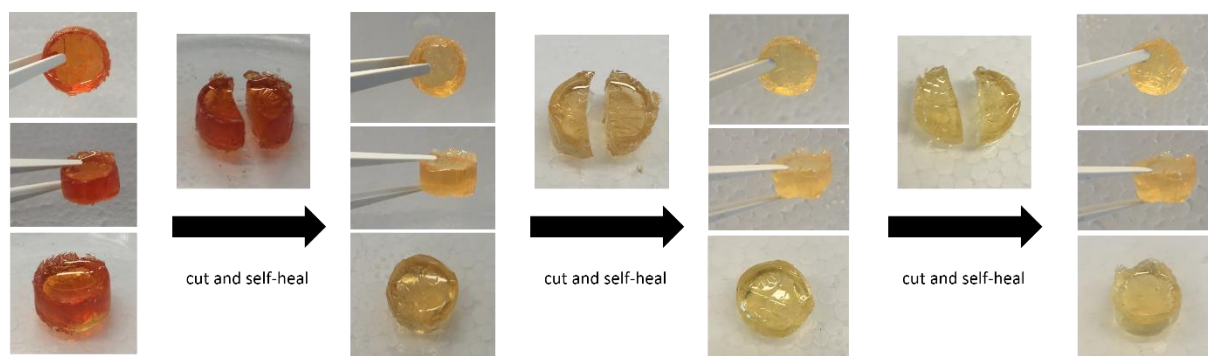


Figure 12: Self-healing of the organic framework. Left: organic framework after synthesis; Middle: organic framework cut in two pieces; Right: organic framework after self-healing. Repeated for 3 cycles.^[95] Reproduced from Ref. 95 with permission from The Royal Society of Chemistry.

In the next experiment, a freshly synthesized organic framework without any washing was used. Like the previous experiments, the organic framework was cut in two pieces and placed in contact to each

other. Also, in this case, 3 mm glass beads were added to fix the position of the two pieces while heating. This time, the contact interfaces disappeared, and the two pieces were strongly joined together. Figure 12 shows the organic framework 1) before cutting, 2) after cutting and 3) after self-healing. The color change of the organic framework is attributed to the diffusion of the TEMPO molecules into the solvent during the experiment. The same experiment was repeated for additional two times, the contact interfaces still disappeared after every self-healing step and the pieces are strongly joined to each other.

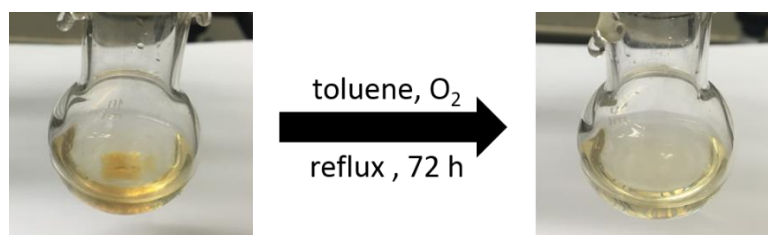


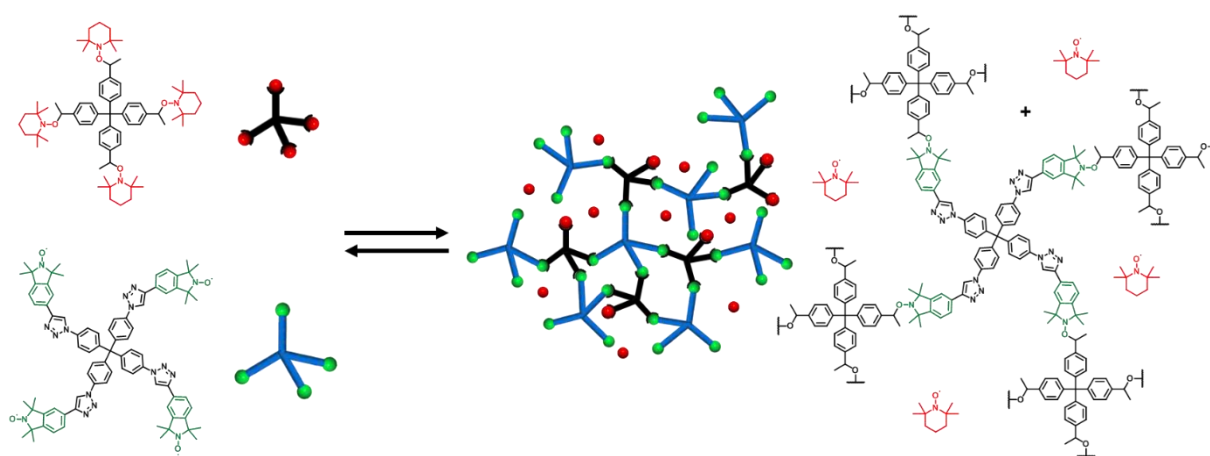
Figure 13: Irreversible destruction of the organic framework by ambient air at elevated temperature.^[95] Reproduced from Ref. 95 with permission from The Royal Society of Chemistry.

As described before, the nitroxide exchange reaction is oxygen sensitive, as the C-centered radical can react with oxygen in the air resulting in an irreversible destruction of the framework. To demonstrate this behavior, two experiments were done. In the first experiment, the framework synthesis was performed in ambient air. By using the same reaction time, no framework was formed. In the second experiment, the organic framework was first synthesized under inert conditions and later heated at elevated temperature under ambient conditions. After three days, the organic framework was completely irreversibly destroyed (Figure 13).

In summary, nitroxide exchange reaction was introduced for the first time to synthesize dynamic covalent linked organic frameworks directly from multifold nitroxide and alkoxyamines. The resulting polymer framework is self-healable and possesses a tunable crosslinking degree and can easily be recycled by modulating the reaction equilibrium. Due to the different hyperfine coupling constants of the involved nitroxide species, EPR spectroscopy has been discovered as a suitable method to *in situ* follow the reaction progress. In addition, solid state EPR spectroscopy further allows the quantitative determination of the defect density in the organic framework, which directly reflects the crosslinking degree.

4.3 Synthesis of porous organic framework with tunable porosity

In the previous chapter, the [3+3] organic framework produced via reversible nitroxide exchange reaction was introduced. It exhibits outstanding stimuli responsive properties and can be controlled precisely by tuning the crosslinking degree with the addition or removal of the byproduct TEMPO nitroxide. However, the [3+3] organic framework has been proven to be barely porous with a BET surface area around only 30 m²/g. Therefore, rigid 3D alkoxyamines and nitroxides have been considered for the synthesis of porous organic framework via nitroxide exchange reaction.



Scheme 52: Synthesis of the [4+4C] organic framework via nitroxide exchange reaction.

For the synthesis of the [4+4C] organic framework, Tetra-AA and Tetra-[C]-NO are dissolved in a toluene/methanol-mixture (9/1). The heat induces the reversible cleavage of C–O from Tetra-AA and leads to persistent nitroxide radicals (TEMPO) and transient C-centered radicals. Transient C-centered radicals spontaneously form new bonds with the Tetra-[C]-NO, which enable the formation of a polymeric framework structures (Scheme 52). The reaction mixture was heated to 100°C analog to the synthesis of [3+3] organic framework, but with a reaction time of 5 days. After washing and drying of the sample we obtained the final organic framework with a yield of 41%.

After each washing step, the washing solution was investigated by EPR spectroscopy. TEMPO nitroxide was proven to be cleaved also in this case as a byproduct from the framework synthesis. It could be shown, that also in this case, the amount of TEMPO nitroxide went below the measurable quantity after five washing cycles.

Analog to [3+3] organic framework, EPR spectroscopy was also used here to investigate the crosslinking degree of the pristine [4+4C] framework. The spin count of 8 mg of [4+4C] framework was determined to be $4.35 \cdot 10^{17}$. The crosslinking degree of the pristine framework was calculated using the equation (19) and (20).

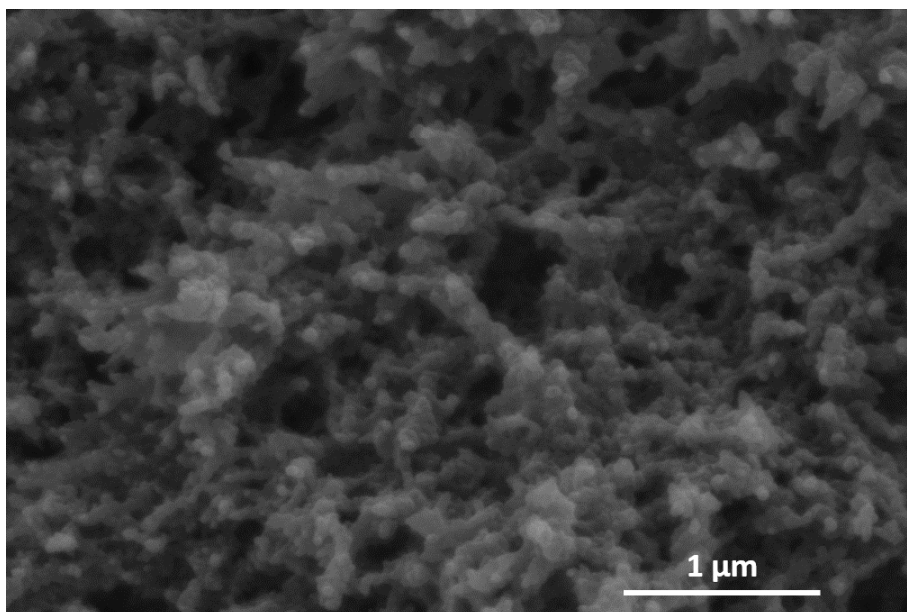


Figure 14: SEM image of pristine [4+4C] framework.

The SEM analysis shown in Figure 14 revealed a mix topology of packed particles and coral-like growth. The particle size varied between 40 nm to 70 nm. Free spaces of 5 to 300 nm between the particles were also observed.

The synthesized organic framework then was investigated with ATR-FT-IR. In the region around 2971 cm^{-1} , and 2871 cm^{-1} , asymmetric and symmetric vibration of aliphatic- CH_3 bond are observed, which origins from the methyl group on the Tetra-AA. In the finger print area, the vibration of aryl-CH can also be identified.

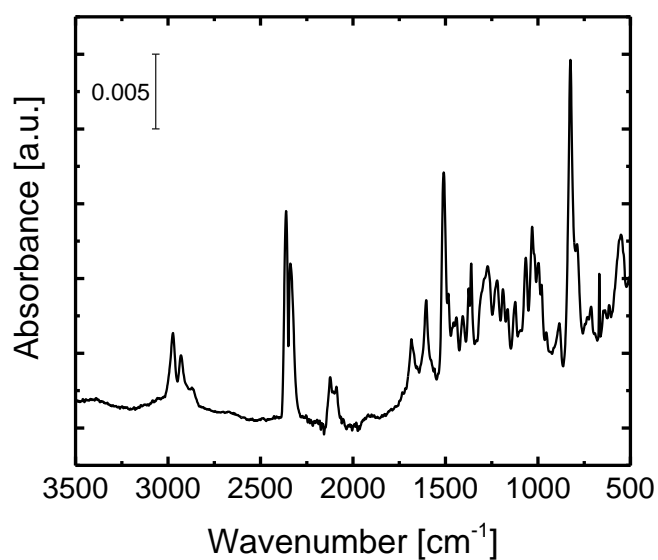


Figure 15: IR spectra of the [4+4C] framework.

Table 8: Crosslinking degree and BET surface area of [4+4C] framework at pristine, annealed and de-crosslinked states.

	Pristine sample	After annealing	After de-crosslinking
CLD [%]	92.8	94.8	88.9
SA _{BET} [m ² /g]	923	675	207

Analog to the equilibrium shift in the previous chapter, this organic framework was also investigated by removal as well as addition of the TEMPO nitroxide to the organic framework at elevated temperature. The crosslinking degree of the [4+4C] frameworks at different equilibrium states were listed in Table 8.

The EPR spectrum of the pristine organic framework is shown in Figure 16 (red). Compared to the EPR spectrum of the organic framework after annealing, the shape of the spectra doesn't show any visible change. However, the defect density of the annealed framework was a bit lower than the pristine framework, resulting in an increase of crosslinking degree from 92.8 % to 94.8 %.

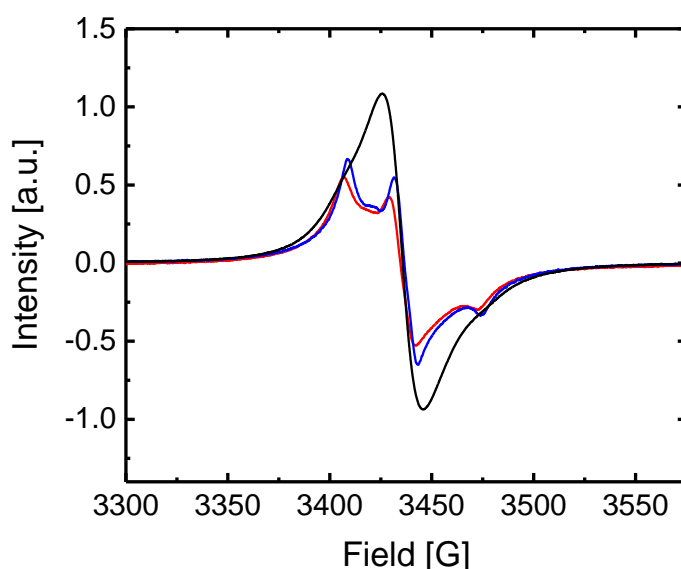


Figure 16: EPR spectra of the pristine [4+4C] organic framework (red), after increasing (blue) and again decreasing (black) the crosslinking degree.

The washing solution after the annealing step was also investigated with EPR to confirm the presence of TEMPO nitroxide in the solution. This is also an indication of successful further crosslinking. After adding 5.00 equivalent TEMPO nitroxide to the organic framework at elevated temperature, the crosslinking degree dropped to 88.9 %. In the EPR spectrum of the framework after de-crosslinking, the defined structure of the two shoulders disappeared to a single broad peak.

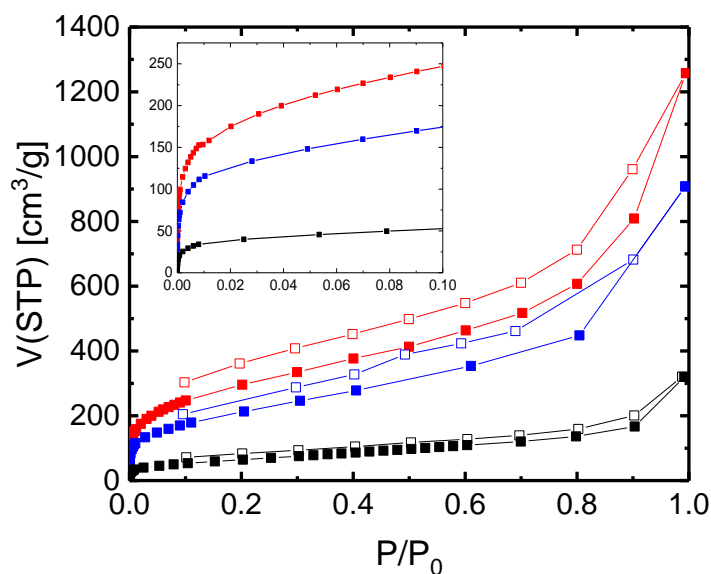


Figure 17: Ar gas adsorption of pristine [4+4C] framework (red), after annealing (blue) and after de-crosslinking (black) measured at 87 K. The filled cubes represent the adsorption branch and the empty cubes represent the desorption branch.

[4+4C] organic frameworks have also been investigated by gas adsorption to determine the porosity of this material. The synthesized frameworks were evacuated in vacuum at room temperature for 120 hours to remove all guest molecules from the pores. From 0 to 1 bar ($1 \text{ bar} = P_0$), uptakes of the [4+4C] framework at different equilibrium states were measured. Between 10^{-5} to $2 \cdot 10^{-2} P/P_0$, sharp uptake was observed in all three states, which indicate the presence of micropores. The amount of adsorbed Argon gas increased in the region $> 0.8 P/P_0$ rapidly, which indicate the capillary condensation of macropores and mesopores formed by the framework synthesis. The Brunauer-Emmett-Teller (BET) model was applied to the isotherm for 0.05 to 0.3. The pristine frameworks have a considerable high BET surface area of $923 \text{ m}^2/\text{g}$. After annealing, the BET surface area dropped to $675 \text{ m}^2/\text{g}$ and after de-crosslinking with 5.00 equivalent TEMPO nitroxide to $207 \text{ m}^2/\text{g}$. In Figure 17, the argon gas adsorption isotherm of the pristine, annealed and de-crosslinked states measured at 87 K were shown.

Using density functional theory (DFT) models, the pore size distribution of the [4+4C] framework at different equilibrium states were investigated. Among all available DFT models, the “Argon at 87 K on carbon for cylindrical pores with QSDFT adsorption branch” was chosen due to the lowest fitting error by all three samples. In Figure 18, the pore size distribution of all three states were shown.

The pristine framework exhibits a predominant micropore of 10 \AA and 18 \AA . Further annealing causes a slight increase of the pore size, while the de-crosslinking step causes a decrease of the pore size to 9 \AA .

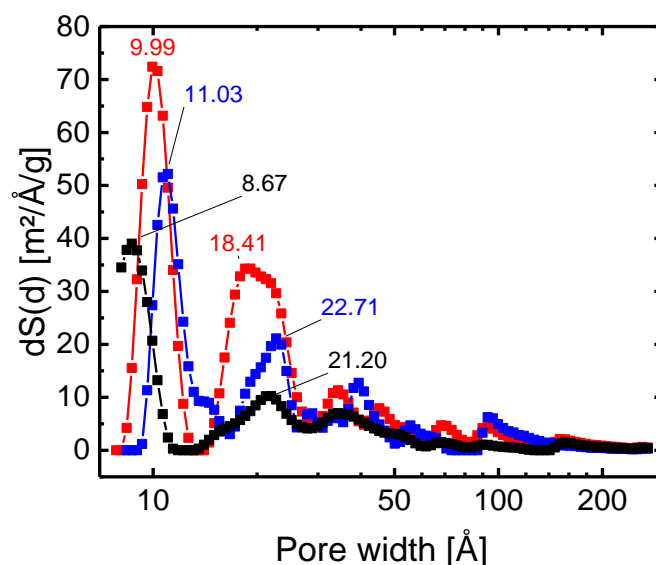
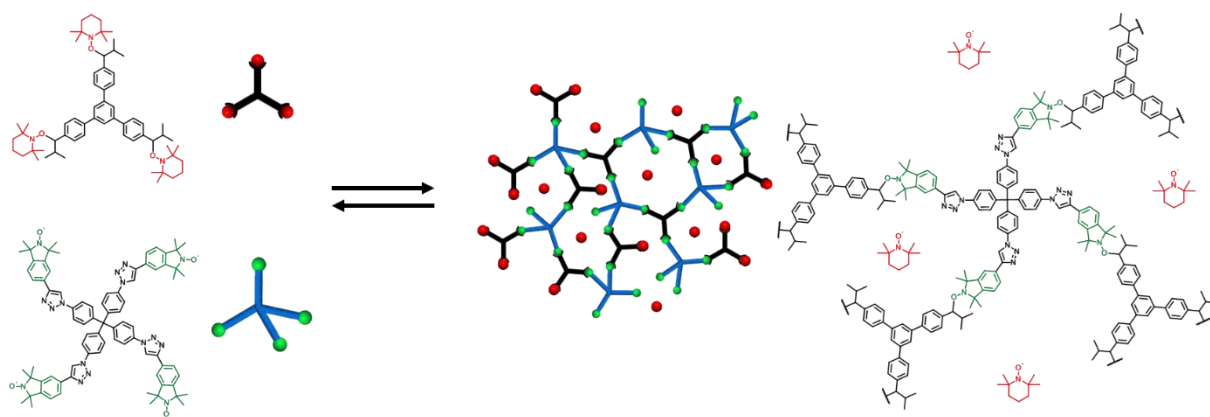


Figure 18: Pore size distribution of pristine [4+4C] framework (red), after annealing (blue) and after de-crosslinking (black).

It was assumed, that unreacted alkoxyamine side groups are present in the pristine framework, which can also be seen by the CLD. During the annealing step, TEMPO nitroxide cleaved from the alkoxyamine side group and the C-centered radical reacts with the nearest unreacted nitroxide side group. The pore size increases through the absence of the cleaved TEMPO nitroxide and the new formed bond. However, during the de-crosslinking step, TEMPO nitroxide molecules were added to the framework. At elevated temperature, homolysis of the C-O bonds occurs and the exchange reaction with TEMPO nitroxide takes place, which causes a higher steric demand. Due to the rigid structure of the building blocks, rotation around its own axis is hindered once two of the four active side groups participate in the exchange process. This is presumably the reason for the minor change in pore size.

Beside the EPR and gas adsorption investigation, the framework was investigated at all three states with XRD. All three states were revealed to be amorphous materials.

In addition to the [4+4C] organic framework, the tuning of the crosslinking degree has also been investigated with other combinations between multivalent alkoxyamines and nitroxide as well as their relationship with the porosity.



Scheme 53: Synthesis of the [3+4C] organic framework via nitroxide exchange reaction.

For the synthesis of the [3+4C] organic framework, Tri-AA and Tetra-[C]-NO are dissolved in a toluene/methanol-mixture (9/1). The heat induces the reversible cleavage of C–O from Tetra-AA and leads to persistent nitroxide radicals (TEMPO) and transient C-centered radicals. Transient C-centered radicals spontaneously form new bonds with the Tetra-[C]-NO, which enable the formation of an organic framework structures (Scheme 53). The reaction mixture was heated to 100 °C for 5 days, analog to the synthesis of [4+4C] organic framework. After washing and drying of the sample the final organic framework was obtained with a yield of 20%.

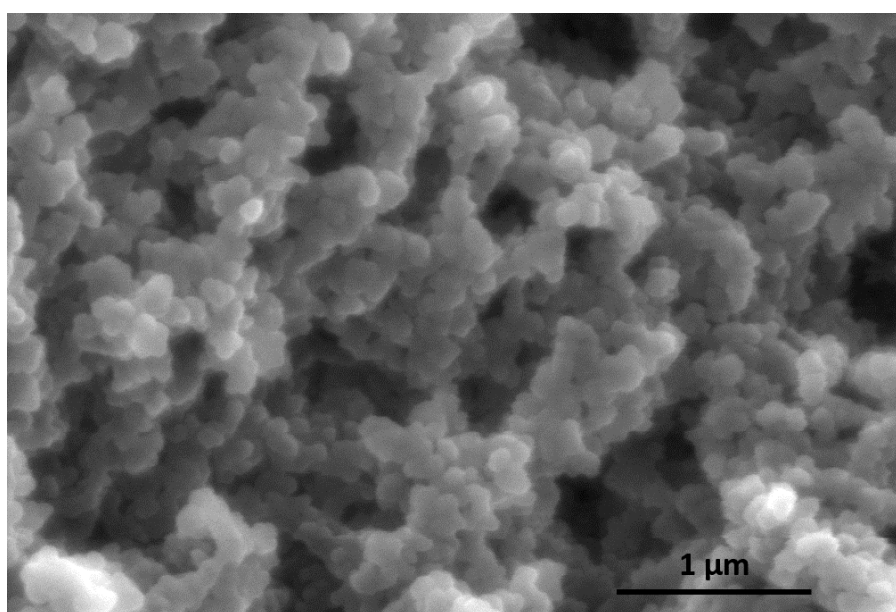


Figure 19: SEM image of pristine [3+4C] framework.

The SEM analysis shown in Figure 19 revealed a mix topology of packed particles. The particle size varied between 50 nm to 150 nm. Free spaces of 5 to 400 nm between the particles were also observed.

The synthesized [3+4C] framework was then investigated with ATR-FT-IR, shown in Figure 20. In the region around 2971 cm^{-1} , and 2871 cm^{-1} , asymmetric and symmetric vibration of aliphatic- CH_3 bond are observed, which originates from the methyl group on the Tri-AA. In the finger print area, the vibration of aryl-CH can also be identified.

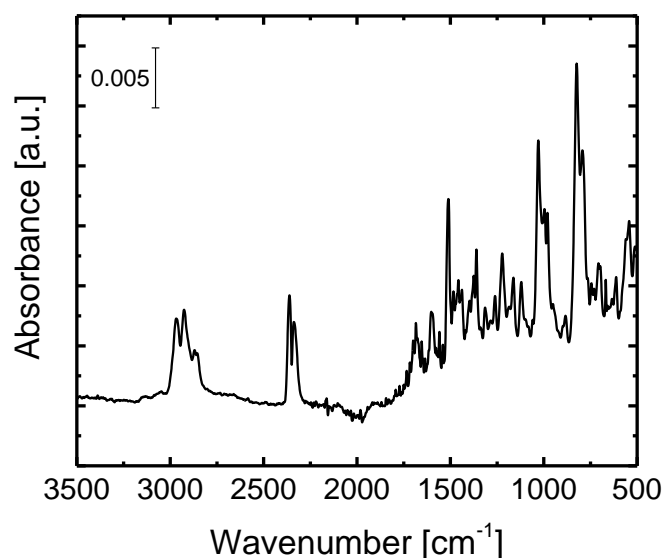


Figure 20: IR spectra of the [3+4C] framework.

After each washing step, the washing solution was investigated by EPR spectroscopy. TEMPO nitroxide was proven to be cleaved also in this case as a byproduct from the framework synthesis. It could be shown, that also in this case, the amount of TEMPO nitroxide went below the measurable quantity after five washing cycles.

Table 9: Crosslinking degree and BET surface area of [3+4C] framework at pristine, annealed and de-crosslinked states.

	Pristine sample	After annealing	After de-crosslinking
CLD [%]	94.1	95.4	86.7
SA_{BET} [m²/g]	1200	995	595

Analog to the equilibrium shift in the previous chapter, this organic framework was also investigated by removal as well as addition of the TEMPO nitroxide to the organic framework at elevated temperature. The crosslinking degree of the [3+4C] frameworks at different equilibrium states were listed in Table 9.

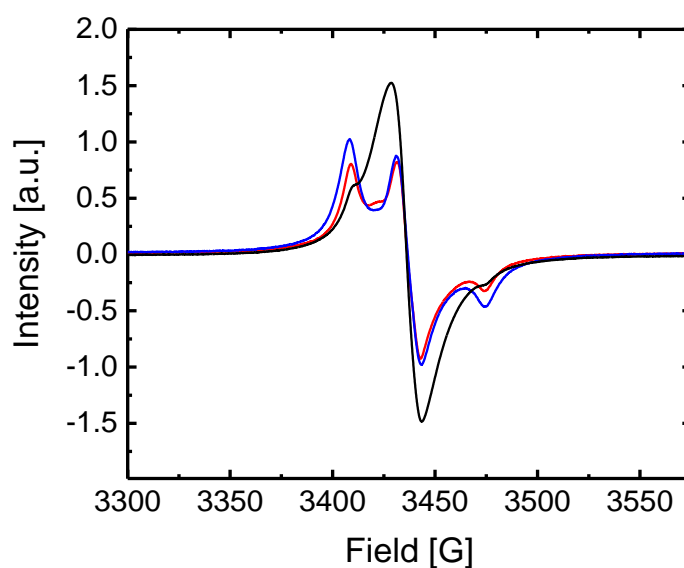


Figure 21: EPR spectra of the pristine [3+4C] organic framework (red), after increasing (blue) and again decreasing (black) the crosslinking degree.

The EPR spectrum of the pristine organic framework is shown in Figure 21 (red). Like [4+4C] framework, the EPR spectra of pristine and annealed sample have no major visible difference in their shape. However, the defect density of the pristine framework is higher than the annealed framework, resulting in an increase of crosslinking degree from 94.1 % to 95.4 %. Also, in this case, TEMPO nitroxide was detected in the washing solution after annealing, which confirm the further crosslinking. Compared to the EPR spectrum of the organic framework after annealing, the shape of the spectrum didn't change. However, the defect density of the annealed framework was lower than the pristine framework, resulting in an increase of crosslinking degree from 92.8 % to 94.8 %. After adding 5.00 equivalent TEMPO nitroxide to the organic framework at elevated temperature, the crosslinking degree dropped to 86.7 %. In the EPR spectra of the framework after de-crosslinking, the intensity of the peak around 3408 G decrease that much, that it is hardly visible under the broad peak around 3428 G.

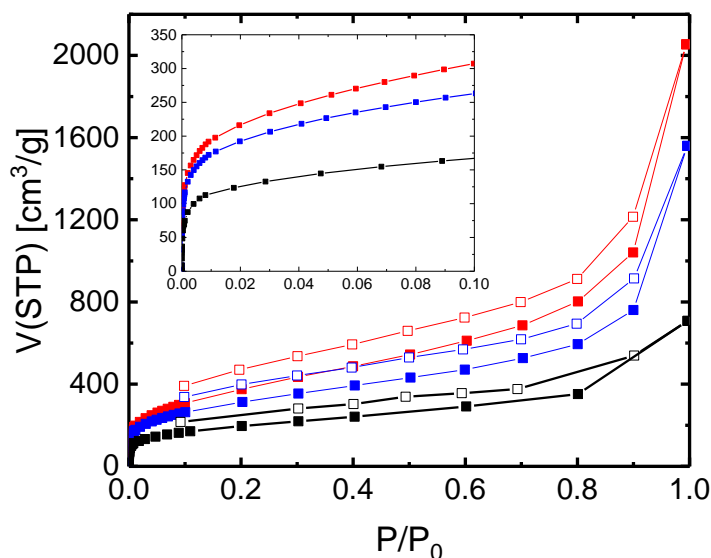


Figure 22: Ar gas adsorption of pristine [3+4C] framework (red), after annealing (blue) and after de-crosslinking (black) measured at 87 K. The filled cubes represent the adsorption branch and the empty cubes represent the desorption branch.

To compare with the previous system, the porosity of the [3+4C] framework at pristine, annealed and de-crosslinked states was also investigated with gas adsorption. Same as the previous system, the uptake measurements were investigated between 0 to 1 bar. Between 10^{-5} to $2 \cdot 10^{-2}$ P/P_0 , sharp uptake was observed in all three states, which indicate the presence of micropores. Also, in this system, presence of macropores and mesopores were indicated due to the rapid increase of adsorbed argon gas from a partial pressure of 0.8. The BET model was applied to the isotherm for 0.05 to 0.3. The pristine frameworks have a BET surface area of $1200 \text{ m}^2/\text{g}$, which is even higher than the pristine [4+4C] framework. After annealing, the BET surface area dropped to $995 \text{ m}^2/\text{g}$ and after de-crosslinking with 5.00 equivalent TEMPO nitroxide to $595 \text{ m}^2/\text{g}$. In Figure 22, the argon gas adsorption isotherm of the pristine, annealed and de-crosslinked states measured at 87 K were shown. Beside the EPR and gas adsorption investigation, the framework was investigated at all three states with XRD. All three states were revealed to be amorphous materials.

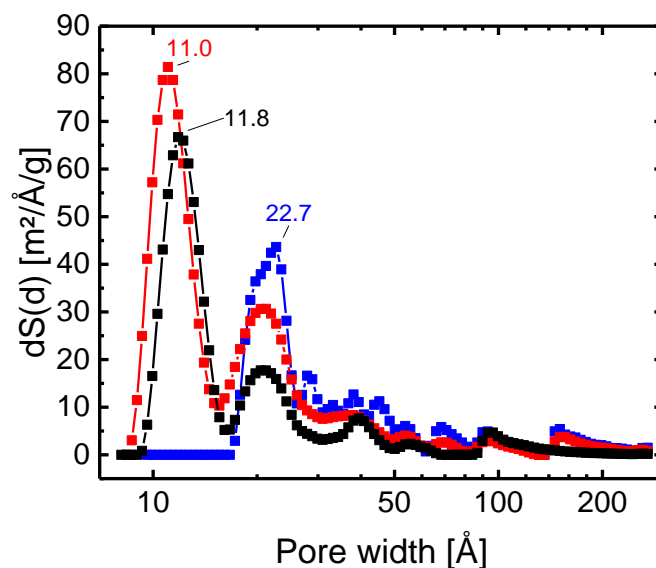
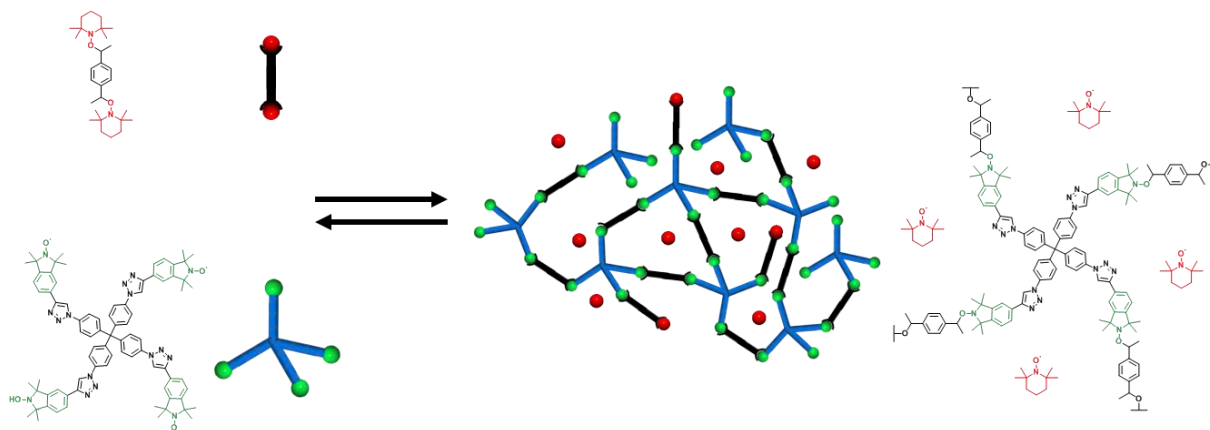


Figure 23: Pore size distribution of pristine [3+4C] framework (red), after annealing (blue) and after de-crosslinking (black).

The pristine framework exhibits predominant micropores of 11 Å and some larger pores between 15 Å and 26 Å. By further annealing, the pores around 11 Å completely vanished and increase of the larger pores between 15 Å to 26 Å were observed. After de-crosslinking, the micropores around 11 Å - 12 Å formed again in the framework and decrease of the larger pores between 15 Å to 26 Å were observed. Like the previous system, unreacted alkoxyamines side groups are present in the pristine framework. Therefore, by cleavage of TEMPO nitroxide during the annealing step, pore size increased through the absence of the cleaved nitroxide and the new formed bond. While the de-crosslinking step, TEMPO nitroxide were added to the framework, resulting reformation of the TEMPO-alkoxyamine side group accompanied with a decrease of the pores. In Table 9, the crosslinking degree and BET surface area of the [3+4C] framework at pristine, annealed and de-crosslinked states were shown.



Scheme 54: Tuning the cross-linking degree by thermal annealing of the network polymer upon removal (left to right) or addition (right to left) of TEMPO nitroxides.

To complete the systematic investigation, Di-AA was also considered for the synthesis of porous organic framework. For the synthesis of the [2+4C] porous organic framework, Di-AA and Tetra-[C]-NO are dissolved in a toluene/methanol-mixture (9/1). The heat induces the reversible cleavage of the C–O from Di-AA, resulting in persistent nitroxide radicals (TEMPO) and transient C-centered radicals. Transient C-centered radicals spontaneously form new bonds with the Tetra-[C]-NO, which enable the formation of the organic framework structures (Scheme 54).

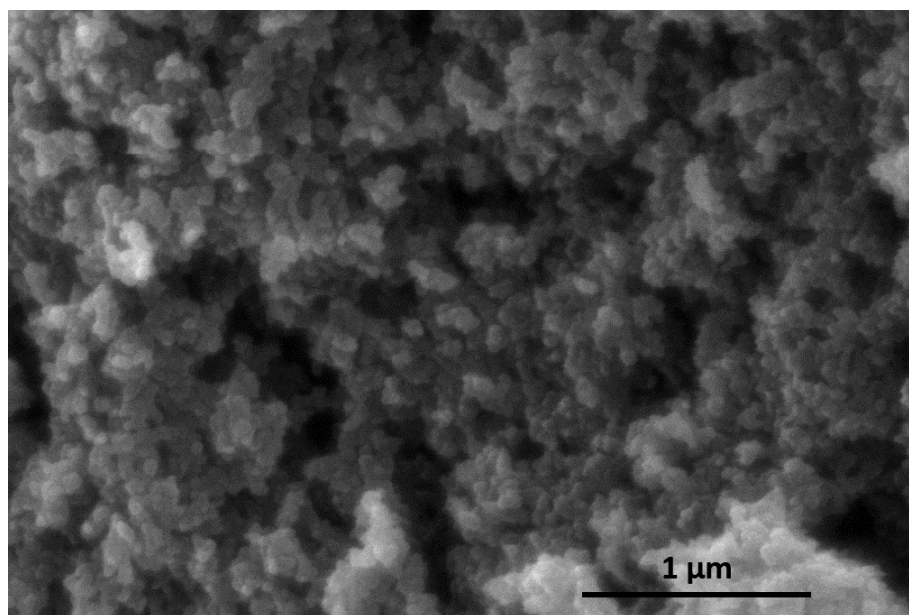


Figure 24: SEM image of pristine [2+4C] framework.

The SEM analysis shown in Figure 24 revealed a mix topology of packed particles. The particle size varied between 20 nm to 70 nm. Free spaces of 5 to 400 nm between the particles were also observed.

Like the previous two frameworks, EPR spectroscopy was used to determine the crosslinking degree of the three different states. According to the defect density, crosslinking degree of the pristine sample was determined to be 93.5 %. After the annealing step, crosslinking degree increase to 96.7 %. Same

as the two previous case, TEMPO nitroxide was also found detected in the washing solution after annealing, indicating a successful further crosslinking step. After the de-crosslinking step with 5.00 equivalent TEMPO nitroxide the CLD decrease to 85.5 %.

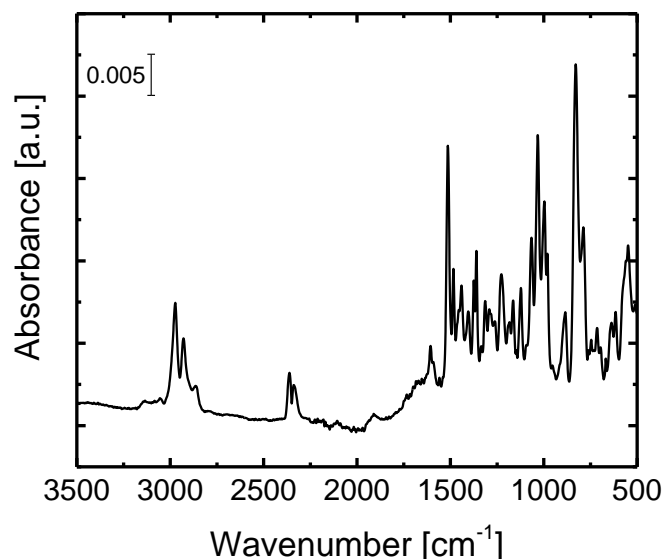


Figure 25: IR spectra of the [2+4C] framework.

The synthesized organic framework then was investigated with ATR-FT-IR. In the region around 2971 cm^{-1} , and 2871 cm^{-1} , asymmetric and symmetric vibration of aliphatic- CH_3 bond are observed, which origins from the methyl group on the Di-AA. In the finger print area, the vibration of aryl-CH can also be identified.

Analog to the equilibrium shift in the previous chapter, this organic framework was also investigated by removal as well as addition of the TEMPO nitroxide to the organic framework at elevated temperature. The crosslinking degree of the [2+4C] frameworks at different equilibrium states were listed in Table 10.

Table 10: Crosslinking degree and BET surface area of [2+4C] framework at pristine, annealed and de-crosslinked states.

	Pristine sample	After annealing	After de-crosslinking
CLD [%]	93.4	96.9	85.6
SA_{BET} [m²/g]	378	666	260

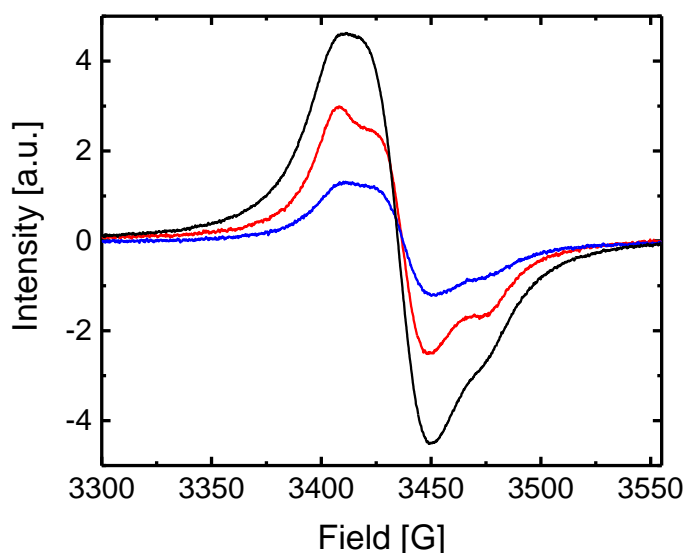


Figure 26: EPR spectra of the pristine [2+4C] organic framework (red), after increasing (blue) and again decreasing (black) the crosslinking degree.

To compare with the previous two systems, the porosity of the [2+4C] framework at pristine, annealed and de-crosslinked states was also investigated with gas adsorption. Same as the previous system, the uptake measurements were investigated between 0 to 1 bar. Also, in this case, sharp uptake was observed between 10^{-5} to $2 \cdot 10^{-2}$ P/P_0 , which indicate the presence of micropores. However, the strong increase of adsorbed argon gas from 0.8 partial pressure indicate the presence of enough meso- and macropores.

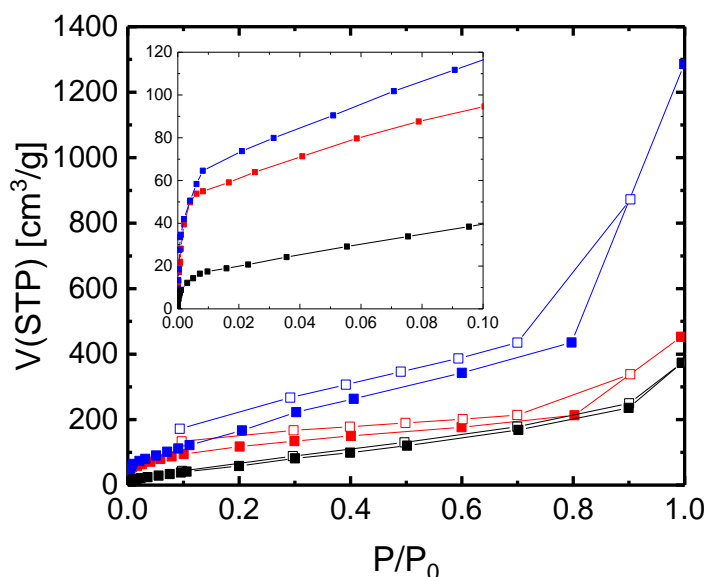


Figure 27: Ar gas adsorption of pristine [2+4C] framework (red), after annealing (blue) and after de-crosslinking (black) measured at 87 K. The filled cubes represent the adsorption branch and the empty cubes represent the desorption branch.

The BET model was applied to the isotherm for 0.05 to 0.3. Unlike the previous systems, the changing of the porosity behaves in another way. The BET surface area of the pristine framework is at $378 \text{ m}^2/\text{g}$.

After the annealing, the BET surface area increases to 666 m²/g. After de-crosslinking with 5.00 equivalent TEMPO nitroxide, the BET surface area decreases to 260 m²/g. In Figure 27, the argon gas adsorption isotherm of the pristine, annealed and de-crosslinked states measured at 87 K were shown.

By considering the pore size distributions, it was observed, that the pores of this frameworks are larger than the other two systems. It was assumed, that the larger pores origins from the underlying topology.

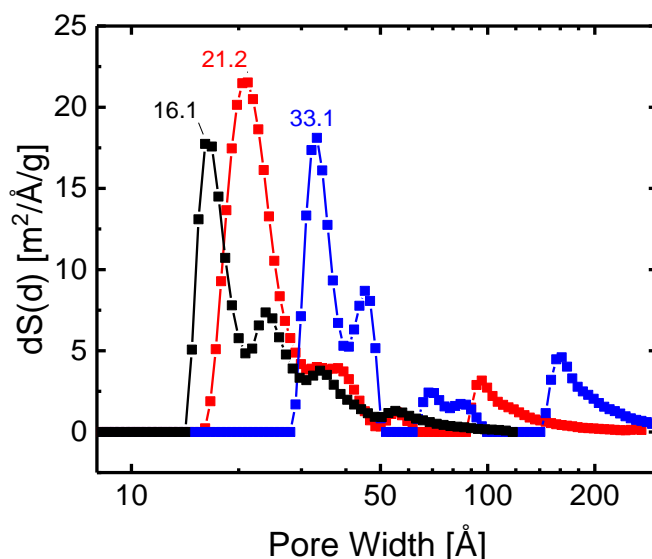


Figure 28: Pore size distribution of pristine [2+4C] framework (red), after annealing (blue) and after de-crosslinking (black).

Both frameworks [2+4C] as well as [4+4C] form a structure composed of tetrahedral nodes (tetrahedral core of Tetra-AA or Tetra-[C]-NO). The difference is the distance between the nodes. For [4+4C] framework, no additional spacer is present between those nodes, resulting in a tightly entangled framework. However, in the [2+4C] framework, the linear alkoxyamine serve as spacer between the tetrahedral nodes, which extends the distance of the tetrahedral nodes.

While annealing of the [2+4C] framework, the unreacted alkoxyamine side group cleaves TEMPO from itself, which make the C-centered radical ready for further reaction with another nitroxide side group. In comparison to [4+4C] framework, the C-centered radical can react with nitroxide groups from slightly more distance duo to its possibility to rotate around its own axis. Therefore, the annealing and de-crosslinking resulting in a significant change in their pore size.

Beside the EPR and gas adsorption investigation, the framework was investigated at all three states with XRD. All three states were revealed to be amorphous material.

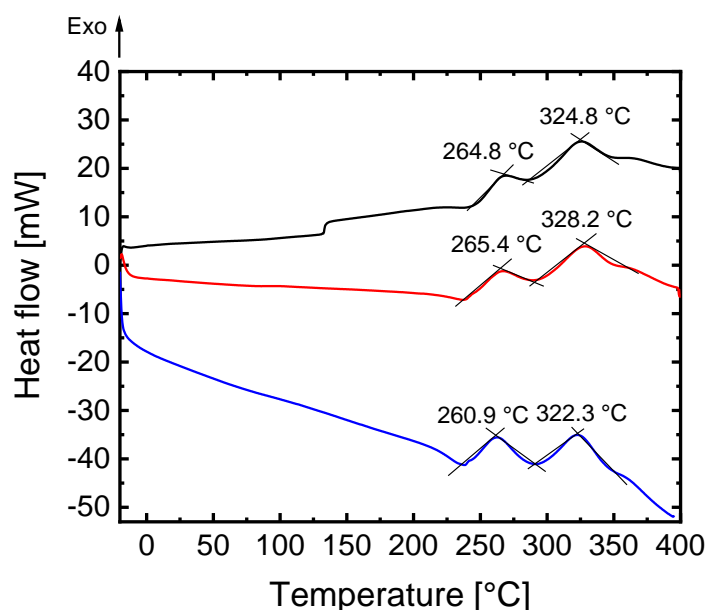
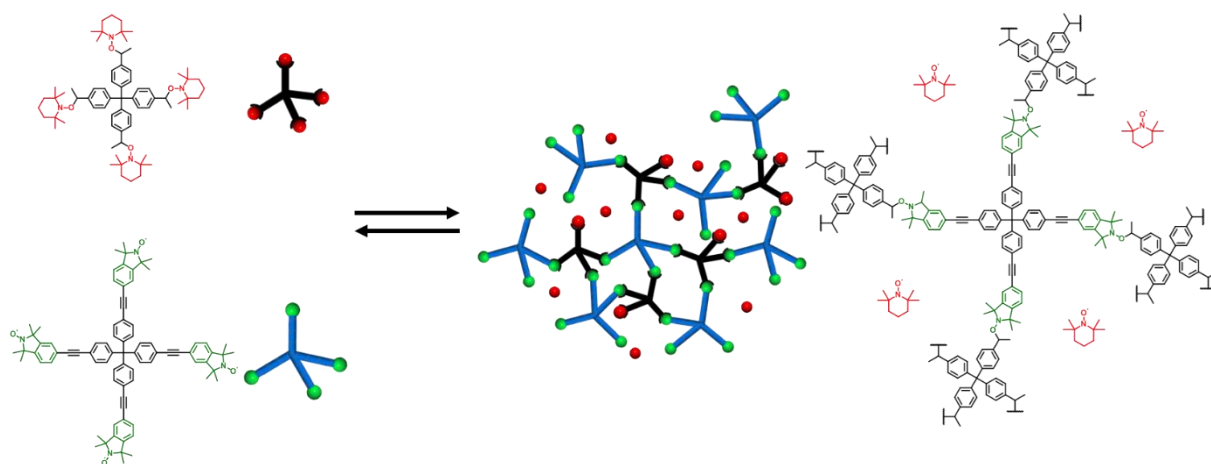


Figure 29: DSC curves of [2+4C] frameworks at pristine (red), annealed (blue) and de-crosslinked (black) status.

Different than the other systems, the DSC curves of [2+4C] frameworks shown in Figure 29 reveals an unexpected phenomenon, i.e. cold crystallization, during the first heating cycle. Indeed, the cold crystallization peak in DSC analysis usually originates only from the amorphous regions, which are left over after a thermal treatment (i.e. annealing in the current case) of a sample. It has been also reported that the state of the amorphous regions clearly can undergo changes due to the aforementioned thermal treatment. Respectively, for the pristine framework, two exothermic peaks were detected. The first peak was observed at 265.4 °C, whereas the second peak appeared at 328.2 °C. After the annealing step, both peaks shift slightly in the lower temperature range to 260.9 °C and 322.3 °C. After the de-crosslinking step, both peaks shifted slightly in the higher temperature range to 264.8 °C and 324.8 °C. It is also distinguished, that the intensity of the first peak increased after the annealing process of the pristine sample, and decreased after the de-crosslinking step. In all three states, any glass transition temperature was detectable, and further no changes were observed while the cooling cycle. In fact, the presence of cold crystallization points out an increase of mobility within the framework at elevated temperature. The mobility enables the possibility to reorient the reactive units, and triggers the reorganization of fragments within the framework, resulting in stacking of the aromatic backbones of the particular di-fold components. It is postulated, that the aromatic systems within the framework are more tended to reorganize at higher crosslinking degree than at lower crosslinking degree. Consequently, the reason for the appearance of cold crystallization only in [2+4C] framework, but not in the other frameworks can be rationalized in this way. Particularly, assuming that the stacking of the aromatic backbones of other multi-fold components is not feasible due to compositional geometry.

For the synthesis of another tetra-fold nitroxide building block, the Sonogashira-Hagihara cross coupling reaction was considered. The reason to use a different reaction is to synthesize a tetra-fold nitroxide is the altered geometry. While the angle of the nitroxide radical from Tetra-[C]-NO is around 60° to the core, the angle of the nitroxide radical from Tetra-[S]-NO is only around 30° to the core. Due to the reduce of the angle, a more defined structuring was assumed as the building block became closer to a perfect tetrahedral.



Scheme 55: Synthesis of the [4+4S] organic framework via nitroxide exchange reaction.

The synthesis of the [4+4S] organic framework is the same as the synthesis of the [4+4C] framework. Tetra-AA and Tetra-[S]-NO are dissolved in a toluene/methanol-mixture (9/1). The heat induces the reversible cleavage of C–O from Tetra-AA and leads to persistent nitroxide radicals (TEMPO) and transient C-centered radicals. Transient C-centered radicals spontaneously form new bonds with the Tetra-[S]-NO, which enable the formation of an organic framework structures (Scheme 55). The reaction mixture was heated to 100°C for 5 days. After washing and drying of the sample we obtained the final organic framework with a yield of 33%.

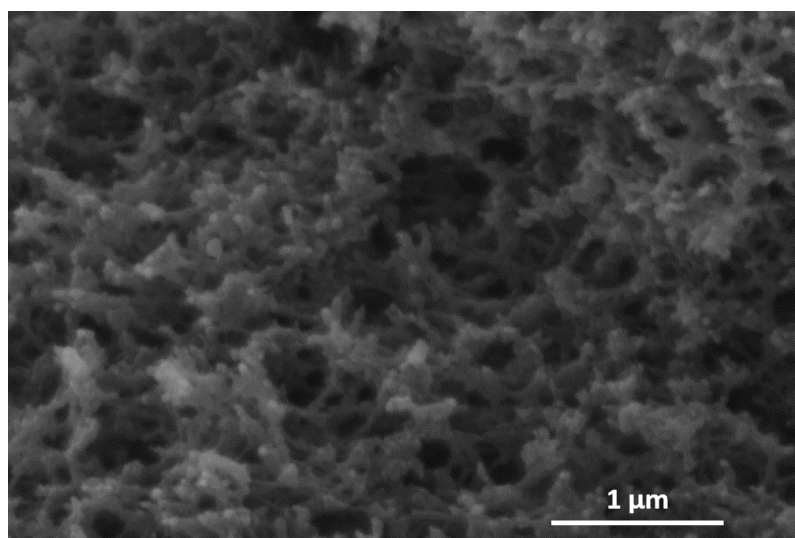


Figure 30: SEM image of pristine [4+4S] framework.

The SEM analysis shown in Figure 30 revealed a mix topology of packed particles and coral-like growth. The particle size varied between 30 nm to 60 nm. Free spaces of 50 to 500 nm between the particles were also observed.

EPR as well as gas adsorption of pristine annealed and de-crosslinked framework were measured to determine the CLD and the porosity of the material.

Table 11: Crosslinking degree and BET surface area of [4+4S] framework at pristine, annealed and de-crosslinked states.

	Pristine sample	After annealing	After de-crosslinking
CLD [%]	90.3	93.3	84.5
SA_{BET} [m²/g]	1150	266	168

Analog to the equilibrium shift in the previous chapter, this organic framework was also investigated by removal as well as addition of the TEMPO nitroxide to the organic framework at 100 °C. The crosslinking degree of the [4+4S] frameworks at different equilibrium states were listed in Table 11.

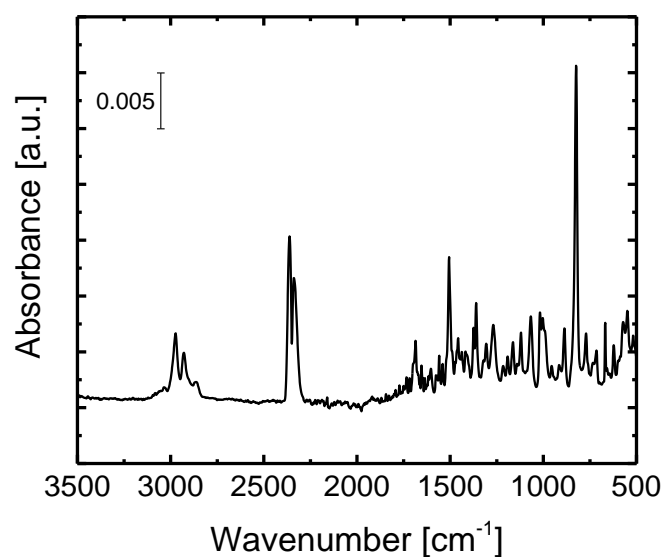


Figure 31: IR spectra of the [4+4S] framework.

The synthesized organic framework then was investigated with ATR-FT-IR. In the region around 2971 cm⁻¹, and 2871 cm⁻¹, asymmetric and symmetric vibration of aliphatic-CH₃ bond are observed, which origins from the methyl group on the Tetra-AA. In the finger print area, the vibration of aryl-CH can also be identified.

According to the defect density by the EPR spectra, CLD of the pristine framework was determined to be 90.3 %. After the annealing step, the CLD increase to 93.3 %. The washing solution after annealing confirmed the presence of TEMPO nitroxide, which indicates the successful further crosslinking. and

decrease to 84.5 % after de-crosslinking with 5.00 equivalent TEMPO nitroxide. The EPR spectra of all three states were shown in Figure 32.

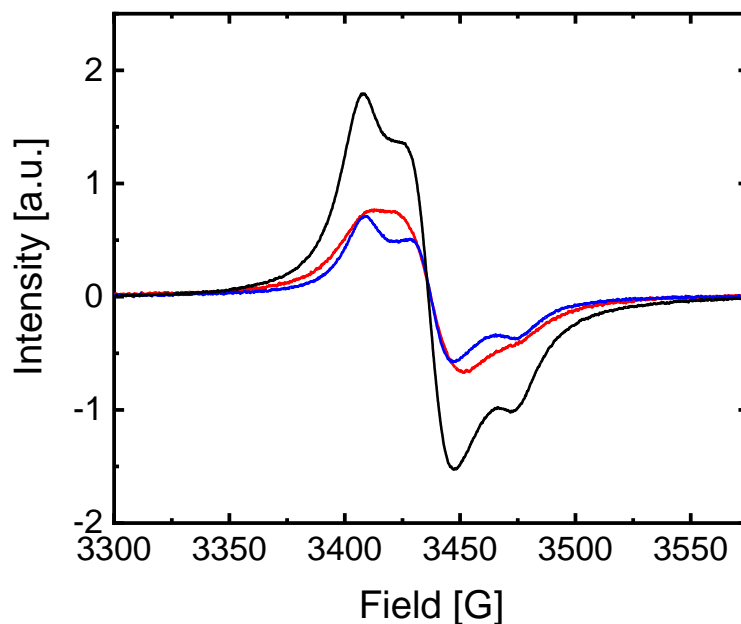


Figure 32: EPR spectra of the pristine [4+4S] organic framework (red), after increasing (blue) and again decreasing (black) the crosslinking degree.

The uptake measurements were investigated between 0 to 1 bar. A sharp uptake was observed between 10^{-5} to $2 \cdot 10^{-2}$ P/P_0 , which indicate the presence of micropores. Also, in these systems, meso- and macropores are not negligible due to the strong increase of adsorbed argon gas after 0.8 partial pressure.

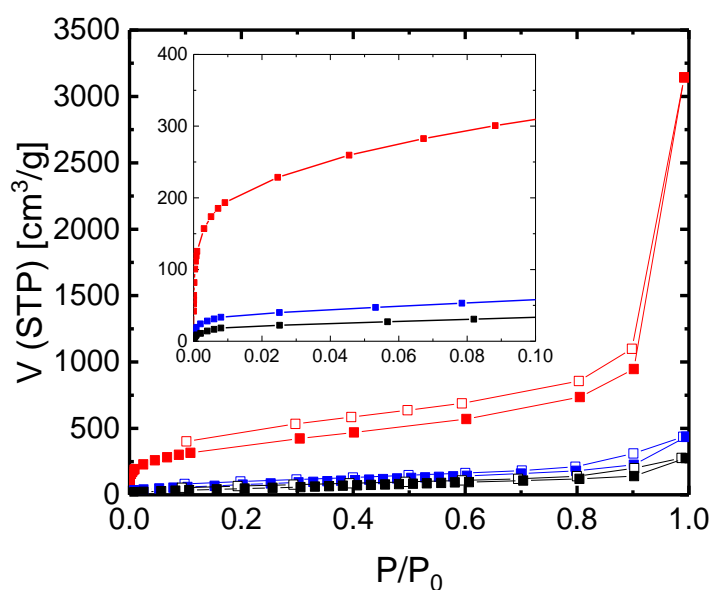


Figure 33: Ar gas adsorption of pristine [4+4S] framework (red), after annealing (blue) and after de-crosslinking (black) measured at 87 K. The filled cubes represent the adsorption branch and the empty cubes represent the desorption branch.

As expected, after applying the BET model to the isotherm from 0.05 to 0.3 partial pressure, the pristine framework has a high BET surface area of 1150 m²/g. However, after the annealing step, the BET surface area decreases significantly to 266 m²/g. After the de-crosslinking step, the BET surface area decreased further to 168 m²/g. In Figure 33, the argon gas adsorption isotherm of the pristine, annealed and de-crosslinked states measured at 87 K were shown.

By considering the pore size distributions, it was observed, that the pristine framework has predominant micropore like [4+4C] framework at 10 Å. Between 16 Å and 27 Å, larger pores are present. However, the micropores around 10 Å was completely not existing anymore after the annealing step. Also, after the de-crosslinking step, the micropores didn't form back but growing larger, which may indicate a structure collapse.

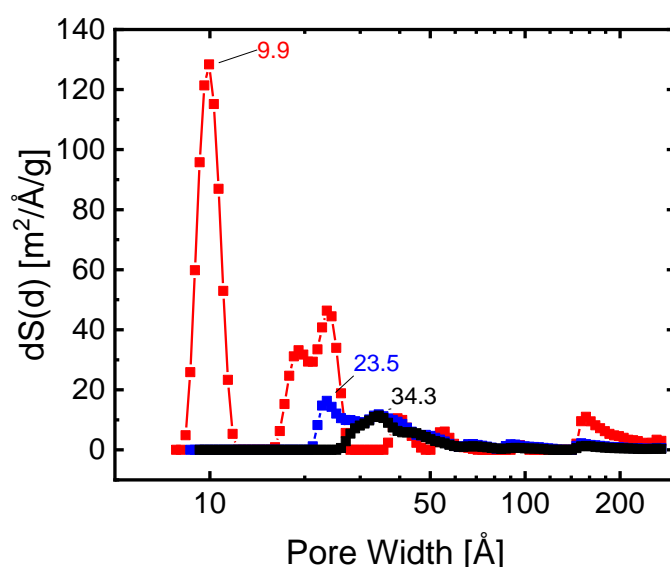


Figure 34: Pore size distribution of pristine [4+4S] framework (red), after annealing (blue) and after de-crosslinking (black).

Due to the limited amount of the organic building blocks, this experiment could not be repeated. Therefore, it is not clear if the framework was really collapsed or due various reasons it collapsed after annealing and de-crosslinking.

Beside the EPR and gas adsorption investigation, the framework was investigated at all three states with XRD. All three states were revealed to be amorphous material.

In summary, the nitroxide exchange reaction was introduced for the synthesis of porous organic polymer directly from tetra-fold nitroxide and di-, tri-, tetra-fold alkoxyamines. The resulting polymers show tunable porosity and crosslinking degree by modulating the reaction equilibrium. In Table 12, the BET surface area of each pristine frameworks and their node to node strut lengths are summarized.

Table 12: Summary of the BET surface area and simulated node to node strut length from each framework.

	S_{BET} [m^2/g]	L_{strut} [\AA]
2+4C	378	33.6
3+4C	1200	19.8
4+4C	923	17.5
4+4S	1150	16.2

Particularly regarding the pristine frameworks, it was observed, that the frameworks based on different multi-fold building blocks result in different surface areas and pore size distributions. To determine the reason for this behavior, the node to node strut lengths were investigated using the simulated 3D structure of each framework. For the [2+4C] framework, the node to node strut length was determined to be 33.6 \AA . The [3+4C] framework has a strut length of 19.8 \AA and the [4+4C] framework a strut length of 17.5 \AA . The strut length of [4+4S] framework was determined to be 16.2 \AA . Comparing the strut lengths with the BET surface area of the different frameworks, a dependency can be observed.

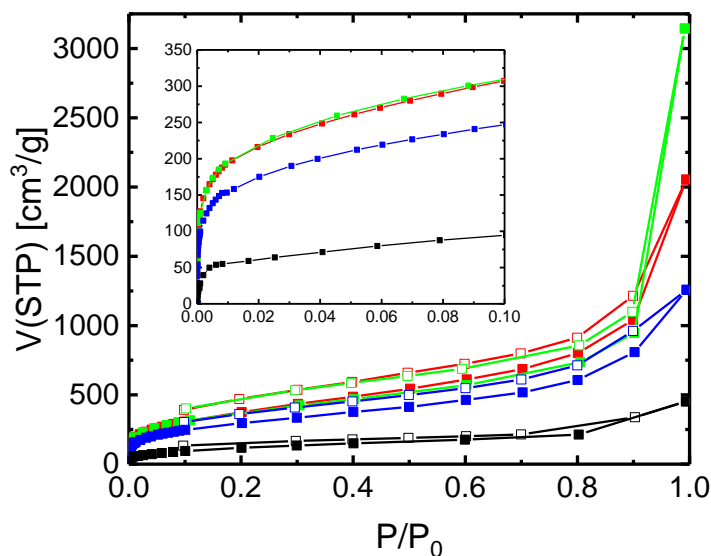


Figure 35: Ar gas adsorption of all pristine frameworks: [4+4C] (blue), [3+4C] (red), [2+4C] (black) and [4+4S] (green).

The smaller the strut length is, the higher the BET surface area. This behavior was also observed in the series of PAE networks synthesized by Cooper and co-workers in 2008.^[96] By comparison of the pore size distribution with the strut lengths, a similar trend was observed. However, much smaller pores

were observed in all pore size distributions. This is probably due to catenation and entanglement within the reacted components. In addition, the mesopores were assumed to arise from the agglomeration of the particles. This assumption can be confirmed by SEM images, that show free spaces of different diameters.

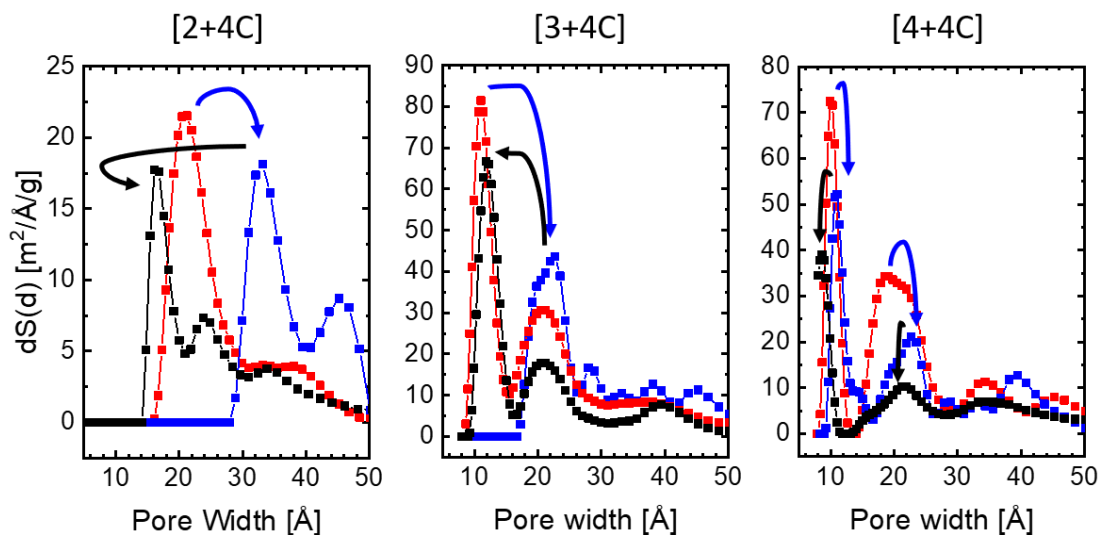


Figure 36: Pore size distribution of [2+4C], [3+4C], [4+4C] frameworks at pristine (red), annealed (blue) and de-crosslinked (black) states. The annealing step is demonstrated as blue arrow and the de-crosslinking step as black arrow.

In Figure 36, pore size distributions of [2+4C], [3+4C] and [4+4C] frameworks in pristine, annealed and de-crosslinked states are shown. It is recognizable, that the pore size increased for all three frameworks after annealing and decreased after de-crosslinking. The difference is the extent of the changes. The pore size changes decreased in the following order: [2+4C] > [3+4C] > [4+4C].

It was assumed, that two processes occur during the annealing step. One process is the further crosslinking of unreacted alkoxyamine moieties with unreacted nitroxide moieties. It has been proven by EPR spectroscopy, that the pristine framework still bears open nitroxide moieties due to the existing paramagnetic signal. Also, in the solution of all annealed framework, TEMPO nitroxide was identified, which indicates the presence of unreacted alkoxyamine moieties in the pristine states. In Table 13, the crosslinking degree of [2+4C], [3+4C] and [4+4C] at pristine, annealed and de-crosslinked states are shown. The increase of the crosslinking degree after annealing indicate of the decrease of EPR active moieties within the framework, which confirmed the further crosslinking of the unreacted alkoxyamine and nitroxide moieties.

Table 13: Crosslinking degrees of [2+4C], [3+4C], [4+4C] frameworks at pristine, annealed and de-crosslinked states.

	pristine [%]	annealed [%]	de-crosslinked [%]
2+4C	93.4	96.9	85.6
3+4C	94.1	95.4	86.7
4+4C	92.8	94.8	88.9

Since the nitroxide exchange reaction is fully reversible, the second process is the bond breakage and recombination of the already formed C-O bond. As already shown in Figure 36, the [2+4C] framework revealed the largest changes during annealing and de-crosslinking step, while [4+4C] framework revealed the least changes. It was assumed that the steric demand of the applied molecular building blocks plays a role in the mobility within the framework structure. Moreover, the probability of the simultaneous cleavage of all four active functional groups within the building blocks during annealing is much lower than in the case of two active functional groups, which also explains the major change in the porosity and pore size of the [2+4C] framework. The simulated structure also indicates that small building blocks like Di-AA which formed through bond breakage and recombination of the framework can easily pass through the pores. Within the framework, the Di-AA can move easily to the desired position and correct framework flaws through recombination. However, this procedure is less likely for increasing building block size. The [4+4S] framework was taken out of the consideration, due to the indication of structural collapse for unknown reason or dense interpenetration of the annealed framework, which is also observed in 3D COFs.^[62]

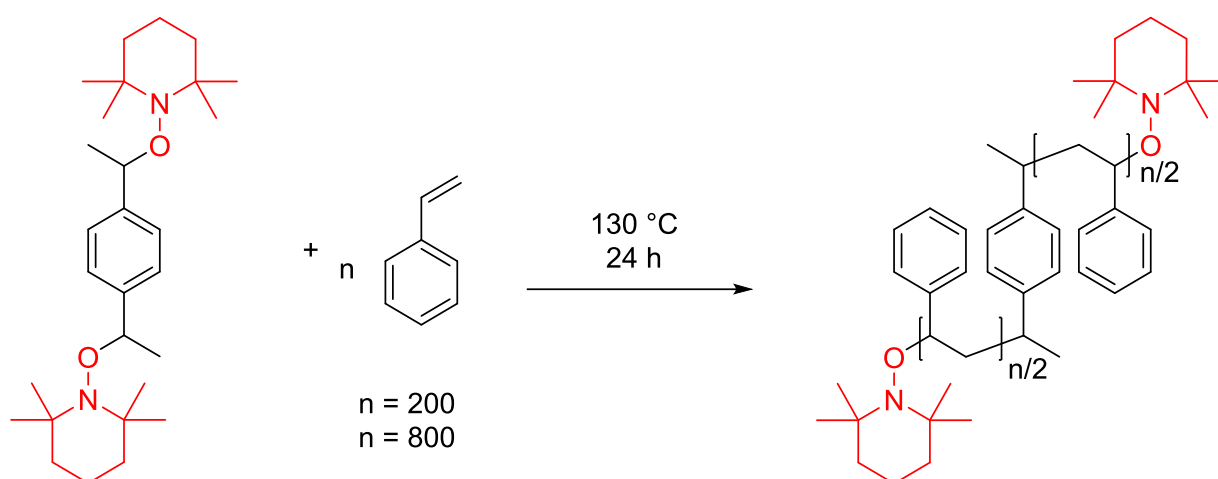
It is also assumed, that reorganization of the particles through annealing leads to different packing resulting in altered interparticular vacancies. During the decrosslinking step, TEMPO nitroxide was added to the framework. At elevated temperature, the added TEMPO nitroxide exchanges with the cleaved nitroxide which lead to narrowing of the pores again. It is speculated, that the de-crosslinking step also decomposes part of the framework structure, resulting in an even lower surface area.

In conclusion, the synthesis of the porous organic framework via nitroxide exchange reaction were introduced. Furthermore, the porosity and the pore size can be modified by modulating the equilibrium of the exchange reaction.

4.4 Synthesis of crosslinked polystyrene via nitroxide exchange reaction

In the previous chapters, nitroxide exchange reaction was developed as a novel reaction for the synthesis of different organic framework with outstanding stimuli-responsive and self-healing properties. In this chapter, nitroxide exchange reaction was combined with the nitroxide mediated polymerization to create a new type of crosslinked polymer.

First, prepolymers were synthesized via nitroxide mediated polymerization with Di-AA and Tri-AA. The reason for choosing this specific type of polymerization is the usage of alkoxyamine as initiator, which will remain as chain end after the polymerization. Using this alkoxyamine end-functionalization, nitroxide exchange reaction can be used to connect linear or star-polymers resulting in a polymer network.



Scheme 56: Polymerization of styrene with Di-AA.

Styrene has been chosen as monomer for the synthesis of linear telechelic and three armed polymers. For the synthesis of linear Di-Polystyrene (Di-PS), Di-AA was used as the initiator. The Di-AA was directly dissolved in styrene without any usage of other solvent under inert conditions. The reaction mixture was heated to $130\text{ }^{\circ}\text{C}$ for 24 h. During the polymerization, the conversions were determined by ^1H NMR and the molar mass and dispersity of the polymer were determined by GPC.

For the synthesis of Di-polystyrene, 200 and 800 equivalent styrene have been considered for the polymerization. The conversion rates, the molar masses and dispersities (\bar{D}) for the synthesis of both Di-PS were listed in Table 14 and Table 15 respectively.

Table 14: Conversion rate, molar mass and \bar{D} of Di-PS with 200 equivalent styrene.

Time [h]	Conversion [%]	M_n [g/mol]	\bar{D}
2	58.5	6900	1.12
3	63.3	6900	1.10
4	86.2	11800	1.13
20	94.3	14800	1.14
Final	100	15800	1.10

By the polymerization of 200 equivalents of styrene, the conversion rate reached already 94.3 % after 20 h. After precipitation and purification, the pure Di-PS has a low \bar{D} of 1.10 and a molar mass of 15900 g/mol, which is close to the targeted molar mass of 21300 g/mol. The difference can be explained by the SEC characterization technique which is relative to a calibration.

Table 15: Conversion rate, molar mass and \bar{D} of Di-PS with 800 equivalent styrene.

Time [h]	Conversion [%]	M_n [g/mol]	PDI
2	61.3	28600	1.12
3	75.8	34400	1.16
4	91.74	57100	1.18
20	94.33	77200	1.23
Final	100	86100	1.16

By the polymerization of 800 equivalent styrene, the conversion rate reached also already after 20 h over 94.3 %. After precipitation and purification, the pure polymer has a \bar{D} of 1.16, which also indicate a controlled polymerization. The molar mass reached 86100 g/mol, which is close to the target molar mass of 83800 g/mol.

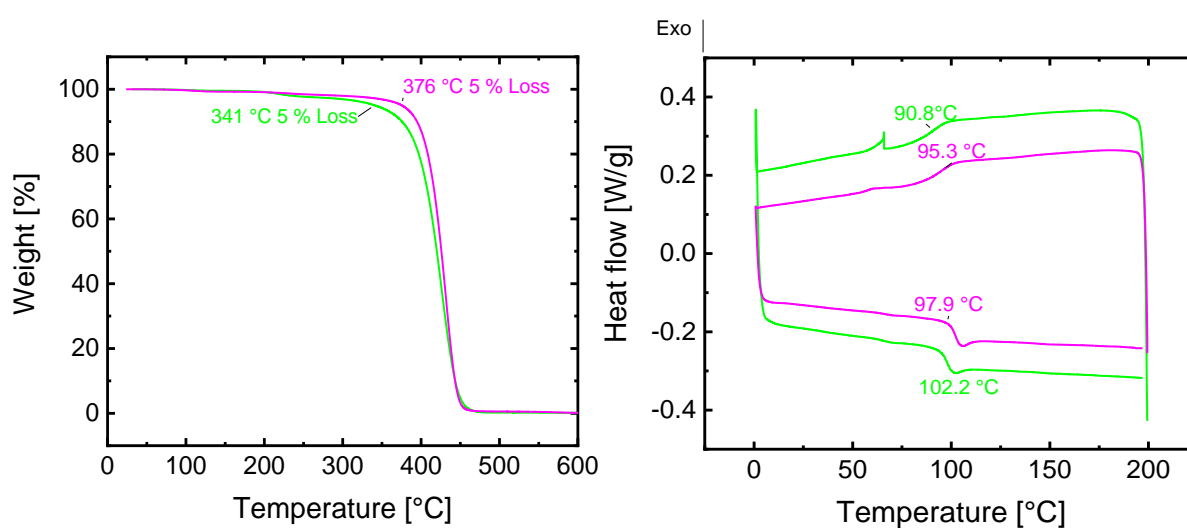
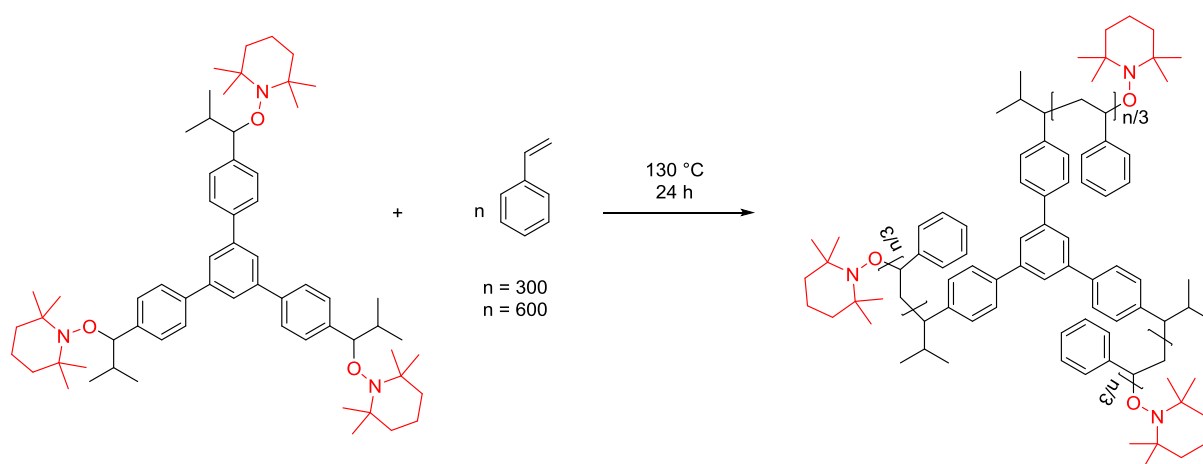


Figure 37: left) Thermal gravimetric analysis data of Di-PS with molar mass of 15800 g/mol (green) and 86100 g/mol (magenta). right) Differential scanning calorimetry data of Di-PS with molar mass of 15800 g/mol (green) and 86100 g/mol (magenta).

Both Di-PS were investigated with thermal gravimetric analysis to determine the thermal decomposition. As shown in Figure 37, the 5 % weight loss were achieved from Di-PS with 15800 g/mol molar mass at 341 °C and from the Di-PS with 86100 g/mol molar mass at 376 °C. The TGA investigation are consistent with the literature, that polymers with higher molar masses have higher decomposition temperature.^[97]

Afterwards, both Di-PS were investigated with differential scanning calorimetry to determine the glass transition temperatures. The Di-PS with 15800 g/mol molar mass has a glass transition temperature of 91 °C upon cooling, while the glass transition temperature during heating appeared at 102 °C. For the Di-PS with 86100 g/mol molar mass, the glass transition temperature during heating was observed at 95 °C and during cooling at 98 °C. Also, in this case, the fact of higher glass transition temperature for polymers of higher molar mass are consistent with the literature.^[98] In Figure 37, the DSC curves of both Di-PS were shown.

For the synthesis of three armed-Polystyrene (Tri-PS), Tri-AA was used as the initiator. The Tri-AA was directly dissolved in styrene without any usage of other solvent at inert condition. The reaction mixture was heated to 130 °C for 24 h. During the polymerization, the conversions were determined by NMR and the molar mass and dispersity of the polymer were determined by GPC.



Scheme 57: Polymerization of styrene with Tri-AA.

For the synthesis of Tri-fold-polystyrene, 300 and 600 equivalents of styrene have been considered for the polymerization. The conversion rates, the molar masses and dispersity (\mathcal{D}) for the synthesis of both Tri-PS were listed in Table 16 and Table 17 respectively.

Table 16: Conversion rate, molar mass and \bar{D} of Tri-PS with 300 equivalents of styrene.

Time [h]	Conversion [%]	M_n [g/mol]	PDI
2	64.9	13600	1.12
4	64.5	14600	1.11
6	79.4	16600	1.14
10	90.1	17500	1.11
Final	100	18400	1.11

By the polymerization of 300 equivalents of styrene, the conversion rate reached after 10 h 90.1 % with a molar mass of 17500 g/mol. After precipitation and purification, the molar mass was determined to be 18400g/mol, which is around 57 % of the target molar mass of 32200 g/mol. The PDI of 1.11 indicate a good control of the polymerization. However, the GPC device is calibration with standard linear polystyrene, therefore the real molar mass of the Tri-PS could be higher.

Table 17: Conversion rate, molar mass and \bar{D} Tri-PS with 600 equivalents of styrene.

Time [h]	Conversion [%]	M_n [g/mol]	PDI
2	58.5	19000	1.29
4	75.2	26800	1.30
6	90.90	33500	1.25
10	91.74	33300	1.31
Final	100	34500	1.30

Also, by the polymerization of 600 equivalents of styrene, over 90 % was converted after 10 h. After precipitation and purification, the molar mass of the pure Tri-PS was determined to be 34500 g/mol, which is around 55 % of the target molar mass of 63400 g/mol. The \bar{D} of 1.30 is correct for a branched polymer, indicating a good control of the polymerization. In Figure 38, the GPC spectra of both Di-PS and both Tri-PS were shown.

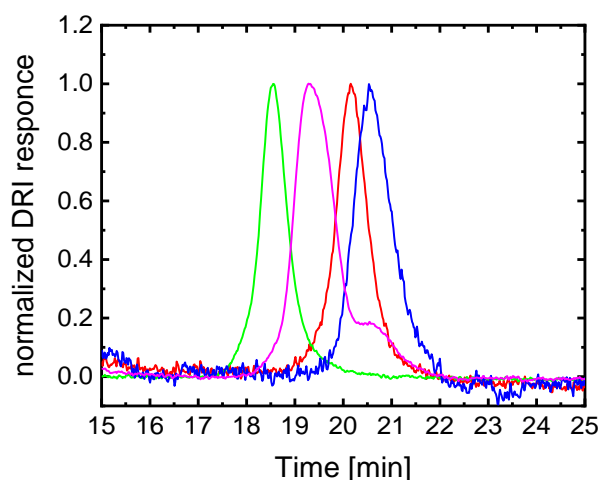


Figure 38: Gel permeation chromatography of the Di-PS with 15800 g/mol (blue), 86100 g/mol (green), Tri-PS with 18350 g/mol (red), 34520 g/mol (magenta).

Both Tri-PS were investigated with thermal gravimetric analysis to determine the thermal decomposition. The 5 % weight loss were achieved for the Tri-PS with 15800 g/mol at 336 °C and from the Tri-PS with 34500 g/mol at 363 °C, which is consistent to the previous investigation. In Figure 39, the TGA curves of both Tri-PS were shown.

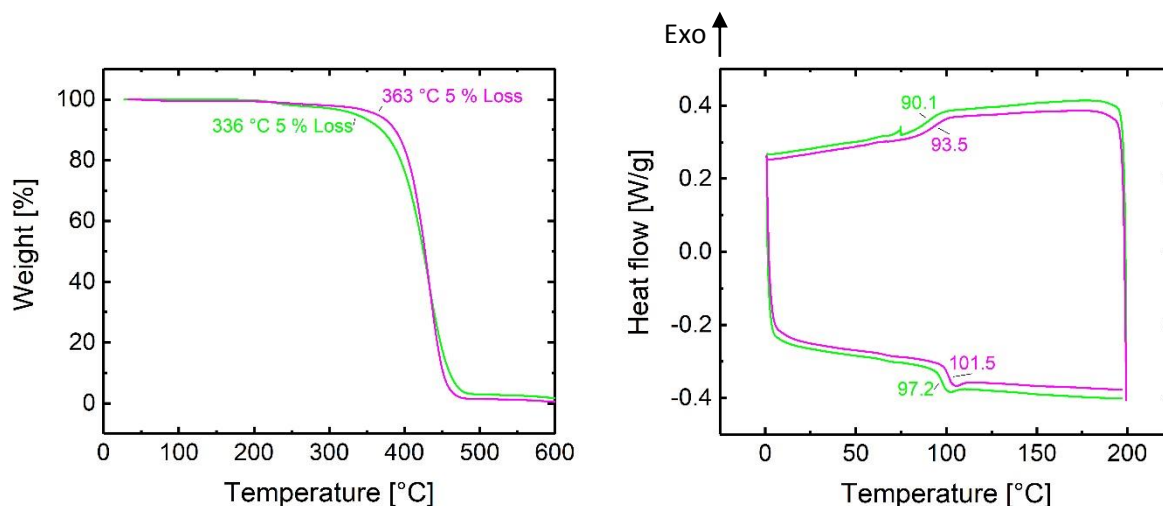


Figure 39: left) Thermal gravimetric analysis data of Tri-PS with molar mass of 18350 g/mol (green) and 34520 g/mol (magenta). right) Differential scanning calorimetry data of Tri-PS with molar mass of 18350 g/mol (green) and 34520 g/mol (magenta).

The Tri-PS with 18300 g/mol molar mass has a glass transition temperature of 90 °C, while the glass transition temperature during cooling appeared at 97 °C. For the Tri-PS with 34500 g/mol molar mass, the same heating rate was used and the glass transition temperature during heating was observed at 94 °C and during heating at 102 °C. By comparison of the glass transition temperatures of both Tri-PS, the same trend was found, as the polymer with lower molar mass possess a lower glass transition temperature. In Figure 39: left) Thermal gravimetric analysis data of Tri-PS with molar mass of 18350 g/mol (green) and 34520 g/mol (magenta). right) Differential scanning calorimetry data of Tri-PS with molar mass of 18350 g/mol (green) and 34520 g/mol (magenta).Figure 39, the DSC curves of both Tri-PS were shown. When comparing the Di-PS with Tri-PS, the DSC data have not shown major difference.

Di-PS as well as Tri-PS were also investigated with ATR-FT-IR, the spectra were, shown in Figure 40. Both IR spectra were nearly identical by comparison. The spectrum of Di-PS as well as of Tri-PS shown typical aromatic C-H stretching bands between the range of 3082 cm^{-1} to 3025 cm^{-1} . Also, the asymmetric and symmetric CH_2 stretching bands at 2921 cm^{-1} and 2850 cm^{-1} was observed. At 1492 cm^{-1} and 1451 cm^{-1} , the aromatic C-C stretching bands were identified. In the range of 1069 cm^{-1} to 538 cm^{-1} , in-plane as well as out-of-plane aromatic stretching bands from the C-H bond were observed.

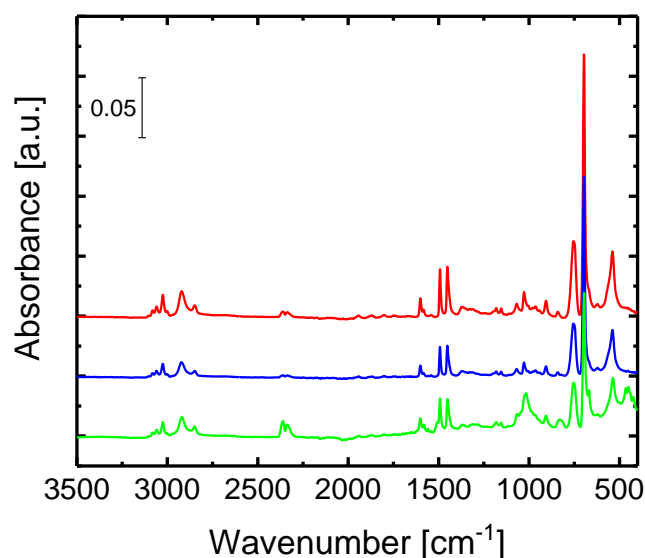


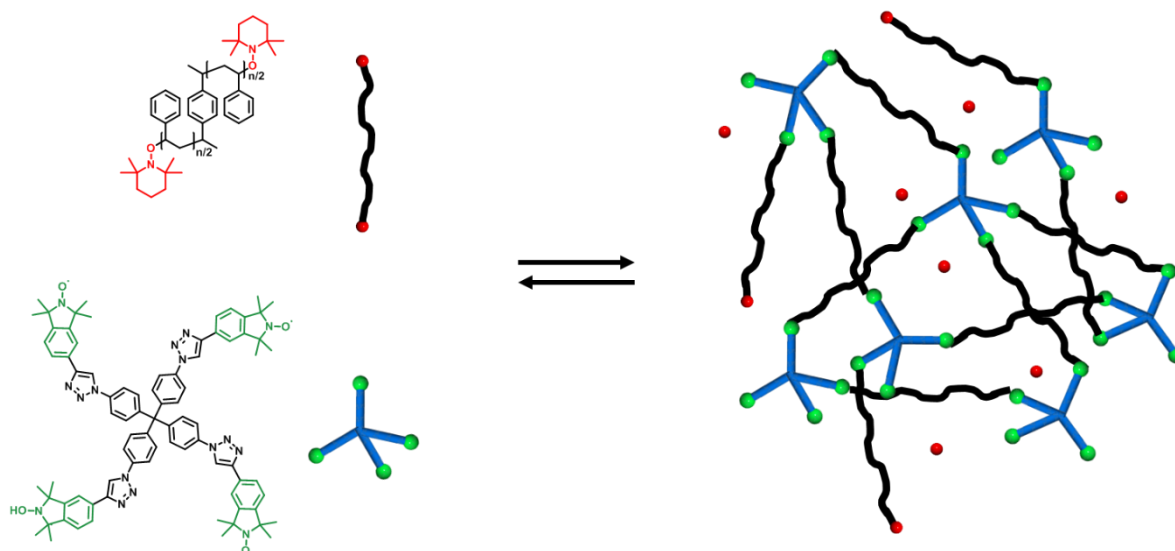
Figure 40: IR spectra of Di-PS (red), Tri-PS (blue) and HCP-172 (green).

For the nitroxide exchange reaction, Di-PS and Tri-PS with the lower molar mass were chosen to obtain networks with a higher crosslinking density. In Table 18, all studied combinations are shown. The exchange reaction was proceeded at 100 °C for 48 h. The ratios were in all cases 1 alkoxyamine to 1 nitroxide moiety.

Table 18: All crosslinking reaction between multifold polystyrene and multifold nitroxide.

	Polystyrene	Nitroxide
CLP-162	Di-PS	Tetra-[C]-NO
CLP-163	Di-PS	Tri-NO
CLP-164	Tri-PS	Tetra-[C]-NO
CLP-165	Tri-PS	Tri-NO

For the nitroxide exchange reaction, Di-PS with 15800 g/mol was chosen to exchange with Tetra-[C]-NO. Di-PS and Tetra-[C]-NO are dissolved in a toluene in inert condition. While the reaction mixture was heated at elevated temperature, the reversible cleavage of the C–O from Di-PS resulted in persistent nitroxide radicals (TEMPO) and transient C-centered radicals. The C-centered radical can spontaneously form new bonds with the used Tetra-[C]-NO. The reaction was screened under different reaction conditions.



Scheme 58: Nitroxide exchange reaction between Di-PS and Tetra-[C]-NO.

In the reaction CLP-162, the exchange reaction was set at 100°C analog to the framework's synthesis with a ratio of 2 Di-PS to 1 Tetra-[C]-NO (1:1 alkoxyamine to nitroxide moiety). For a better understanding, the concentration is referring to the Tetra-[C]-NO. In the sample CLP-162, the concentration of the nitroxide is 0.019 mol/L. However, after washing with THF, a very low amount of precipitate appeared, which were barely enough for further characterization. Therefore, in the next reactions, the temperature was increased to 130 °C.

Table 19: Screening of the exchange reaction with Di-PS and Tetra-[C]-NO.

Sample Nr.	Temperature [°C]	Ratio Di-PS:Tetra-[C]-NO	Concentration (Tetra-[C]-NO) [mol/L]
CLP-162	100	2:1	0.019
CLP-171	130	2:10	0.019
CLP-172	130	2:1	0.095
CLP-173	130	2:1	0.00095

In reaction 171, with the same concentration, the ratio of Di-PS and Tetra-[C]-NO was changed to 2:10 (1:10 alkoxyamine to nitroxide moieties). After purification with THF, the precipitate was investigated with DSC. The glass transition temperature of the CLP-171 shows a clear increase of nearly 10 °C, which indicate the presence of crosslinking points. In the reaction CLP-172 and CLP-173 the ratio of remains 2 Di-PS to 1 Tetra-[C]-NO (1:1 alkoxyamine to nitroxide moieties) but the concentration was modified. Also, in case of reaction CLP-173, the amount of precipitate after purification with THF was very low. Unlike the reaction CLP-173, CLP-172 exhibited an insoluble precipitate after the exchange reaction. In DSC the sample CLP-172 showed a higher glass transition temperature than the sample CLP-171, which indicate a higher crosslinking degree. In the IR spectrum of the CLP-172 shown in Figure 41, additional bands assigned to triazole ring from Tetra-[C]-NO were observed. Due to the fact, that the CLP-172

was washed several times with DCM, unreacted Tetra-[C]-NO should be completely removed. Therefore, the presence of the additional bands verified the successful crosslinking.

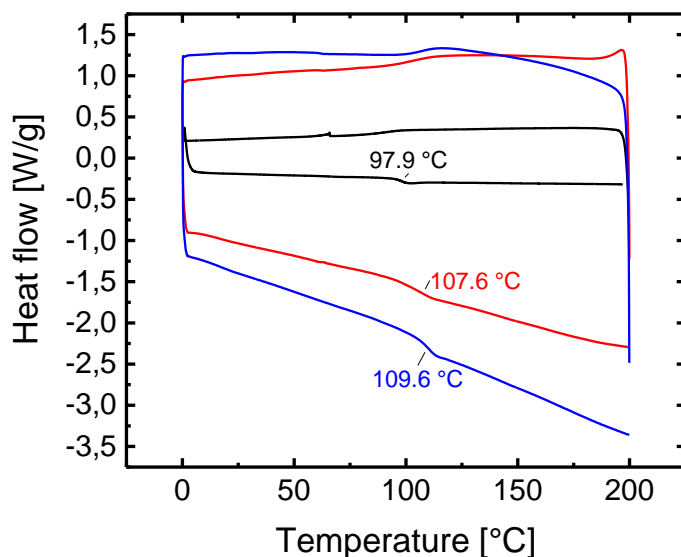
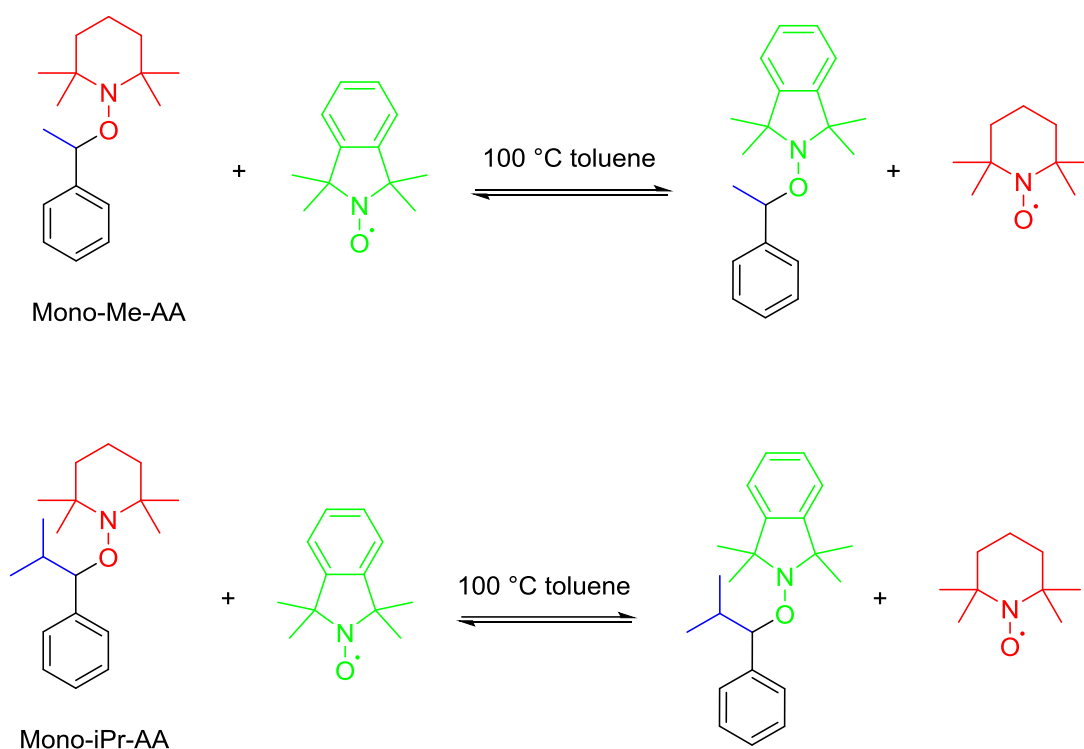


Figure 41: Differential scanning calorimetry data of Di-PS with molar mass of 18350 g/mol (black), HCP-171 (red) and HCP-172 (blue)

In this chapter, the synthesis of crosslinked polymers via nitroxide mediated polymerization combined with nitroxide exchange reaction was introduced. For the synthesis of the polymer networks, well-defined multifold polystyrenes were successfully synthesized via nitroxide mediated polymerization. The crosslinking of the multifold PS with multifold nitroxide turned out to be a challenging. According to the DSC and IR data, crosslinking occurs indeed under the tested reaction condition. To investigate the viscoelastic behavior and mesh size of the crosslinked polymers, swelling tests, dynamic mechanical analysis and inverse gel permeation chromatography should be done, however due to the low amount of the crosslinked polymer, these investigations could not be performed yet. In this investigation, prepolymers were first synthesized and further crosslinked with multi-fold nitroxide. For future investigation, the in chapter 4.2 and 4.3 introduced organic frameworks can be also used as template. By adding styrene at elevated temperature to the organic framework, the polystyrene can grow within the framework.

4.5 Side group effect investigation of alkoxyamine via EPR spectroscopy

For the synthesis of the covalent dynamic frameworks via nitroxide exchange reaction, multifold alkoxyamines with either methyl groups or isopropyl groups were used. However, due to synthetic challenges of some specific building blocks, kinetic investigation of the multifold exchange reactions could not be fully investigated. Therefore, mono-functionalized alkoxyamines and nitroxides were synthesized as model systems for the investigation of the reaction kinetics.



Scheme 59: Up) Exchange reaction between mono-Me-AA and tetra-methyl-isoindoline-NO. Bottom) Exchange reaction between mono-iPr-AA and tetra-methyl-isoindoline-NO.

Two mono-alkoxyamines (abbreviated as mono-AA) with different side groups e.g. Me-, *i*Pr-, marked in blue and TEMPO as leaving nitroxide marked in red were used to investigate the exchange reaction kinetic with tetra-methyl-isoindoline nitroxide (abbreviated in TMINO) marked in green. For the kinetic investigation, the exchange reaction was monitored *in situ* with EPR spectroscopy. To prevent any leaking of the vials or permeation of oxygen into the reaction mixture, several aliquots were prepared according to the time interval e.g. 15 min, 1 h, 2 h, 17 h, 48 h, 96 h, 144 h. Those aliquot sample were taken out from the oven after above mentioned time interval and investigated with EPR spectroscopy.

Before the investigation of the two exchange reactions, 1 mM pure TEMPO and TMINO were investigated with EPR spectroscopy. Using the program Xenon, the EPR spectra of the two pure nitroxides were set as references, which can be later used for the fitting of the reaction mixture. As

already mentioned in chapter 4.2, pure TEMPO has a hyperfine couplings constant of 15.5 G and pure TMINO has a hyperfine couplings constant of 14.1 G. In both exchange reactions, TMINO is the additional nitroxide given into the exchange reaction, therefore the concentration of TMINO should decrease over time. In contrast to TMINO, TEMPO is in both cases the leaving nitroxide, which should show completely opposite behavior than the TMINO.

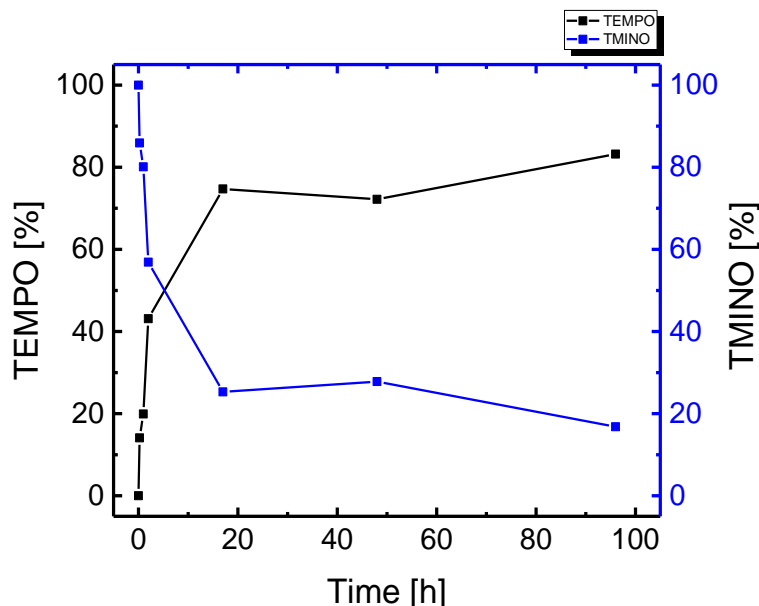


Figure 42: Ratio of two TEMPO nitroxide and TMINO during the exchange reaction between mono Me-AA and TMINO.

First, the exchange reaction between mono-Me-AA and TMINO was investigated. Before the exchange reaction took place, only TMINO was detected via EPR measurement with a hyperfine coupling constant of 14.1 G. Already after 15 minutes, the ratio between both nitroxide moieties start to change. The ratio of TEMPO and TMINO after 15 minutes was determined to be 14 % to 86 %. After 1 hour, the ratio of TEMPO increased from 14 % to 19 % and the ratio of TMINO decreased from 86 % to 81 %. After 2 hours, the ratio of the TEMPO was increased to 43 % and the ratio of TMINO was decreased to 57 %. The next aliquot was reacted overnight, which was taken out after 17 hours. After 17 hours, the ratio change was dramatically, the ratio of TEMPO was determined to be 75 % and the ratio of TMINO was 15 %. After 48 h, no large change in the ration was observed for both nitroxide moieties. Finally, after 96 h, the ratio of TEMPO was determined to be 83 % and the TMINO 17 %.

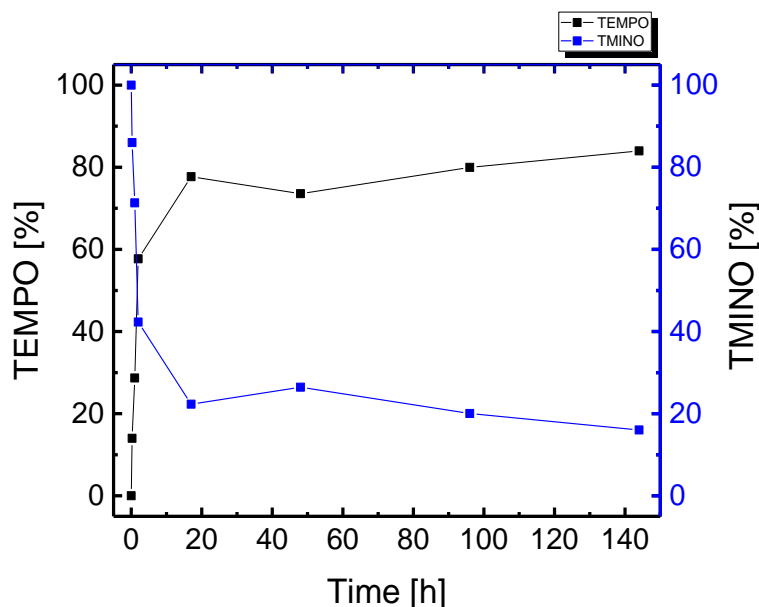
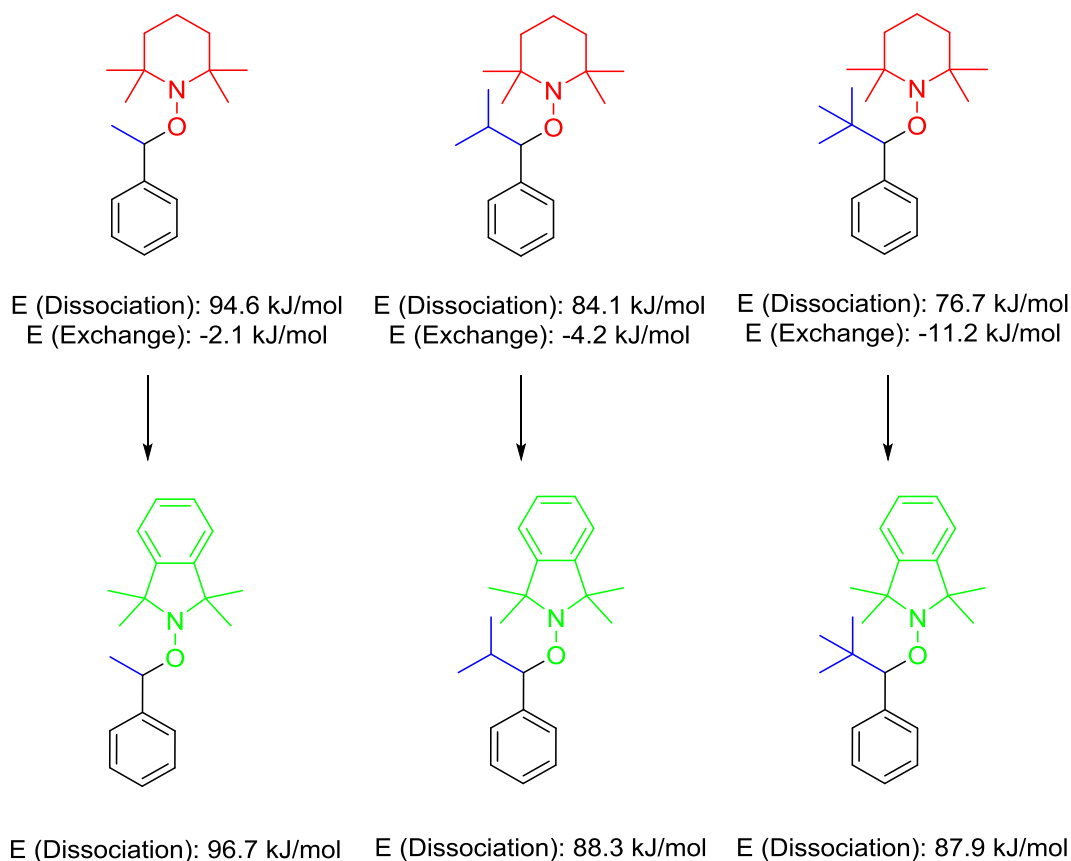


Figure 43: Ratio of two TEMPO nitroxide and TMINO during the exchange reaction between mono *iPr*-AA and TMINO.

Then, the exchange reaction between mono-*iPr*-AA and TMINO was investigated. Also, in this case, only TMINO was detected via EPR measurement before the exchange reaction took place. Unlike the exchange reaction between mono-Me-AA and TMINO, the exchange reaction between mono-*iPr*-AA and TMINO proceeded much faster. According to the EPR measurement, after 1 hour the ratio between TEMPO and TMINO was already determined to be 29 % to 71 %. After 2 hours, the ratio as dominated by TEMPO, since it was determined to be 58 % to 42 %. After 17 hours the ratio between TEMPO and TMINO reached 74 % to 26 %. In the next four days, the ratios have a small fluctuation of 2-3%. Around 144 hours, the ratio between TEMPO and TMINO was determined to be 84 % to 16 %.

When comparing both exchange reactions, a clear difference of the exchange reaction speed in the first 17 hours was observed. The exchange reaction between mono-*iPr*-AA and TMINO proceeded apparently faster than the reaction between mono-Me-AA and TMINO. It was assumed, that the steric demand of the side groups on the alkoxyamines resulting in a significant effect to the exchange reaction. It is further assumed that the inductive effect of the larger alkane groups stabilizes the radical resulting in an increased reactivity.

To verify those assumptions, quantum chemical calculations were performed by Dr. Angela Bihlmeier and Dr. David Sulzer at IPC/KIT. Using the quantum chemical calculations, dissociation energy of mono-Me-AA was determined to be 94.6 kJ/mol and the dissociation energy of mono-*iPr*-AA was determined to be 84.1 kJ/mol. Apparently, the mono-*iPr*-AA has a lower dissociation energy than the mono-Me-AA, which means, that less energy is needed to dissociate TEMPO from mono-*iPr*-AA.

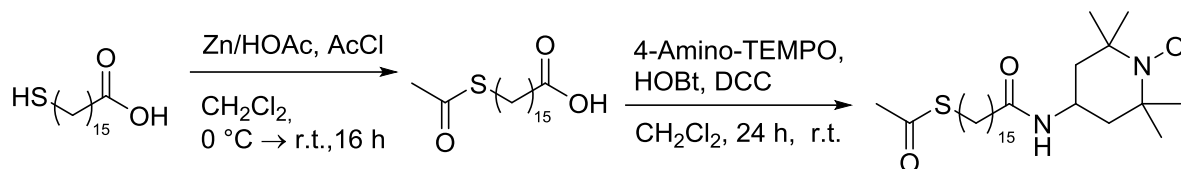


Scheme 60: Dissociation energy of mono-Me-AA, mono-iPr-AA and mono-tBu-AA and the corresponding exchanged TMINO alkoxyamine.

The dissociation energy of the TEMPO functionalized AA can be used to determine the reaction rate of the homolysis and therefore the exchange reaction. A smaller dissociation energy leads to a faster reaction rate thus a faster decrease in concentration of the starting material. The calculated dissociation energies fit qualitatively to the obtained experimental results and proof the feasibility of the method. By comparing the dissociation energies of the TEMPO-based AA and the isoindoline-based AA, the exchange energy can be calculated, which is correlated to the ratio of the compounds at the thermodynamic equilibrium. For the exchange reaction between mono-Me-AA and TMINO, the exchange energy was determined to be -2.1 kJ/mol. Compare to mono-Me-AA, the exchange energy between mono--AA and TMINO was -4.2 kJ/mol. A greater exchange energy shifts the equilibrium towards the product side. These findings were taken as a starting point on how more sterically demanding groups would affect the reaction, for this the *tert*-butyl moiety was calculated. Calculation suggest an exchange energy more than five times larger compared to the methyl-moiety, creating a high interest in supporting this theoretical discovery by experimental results.

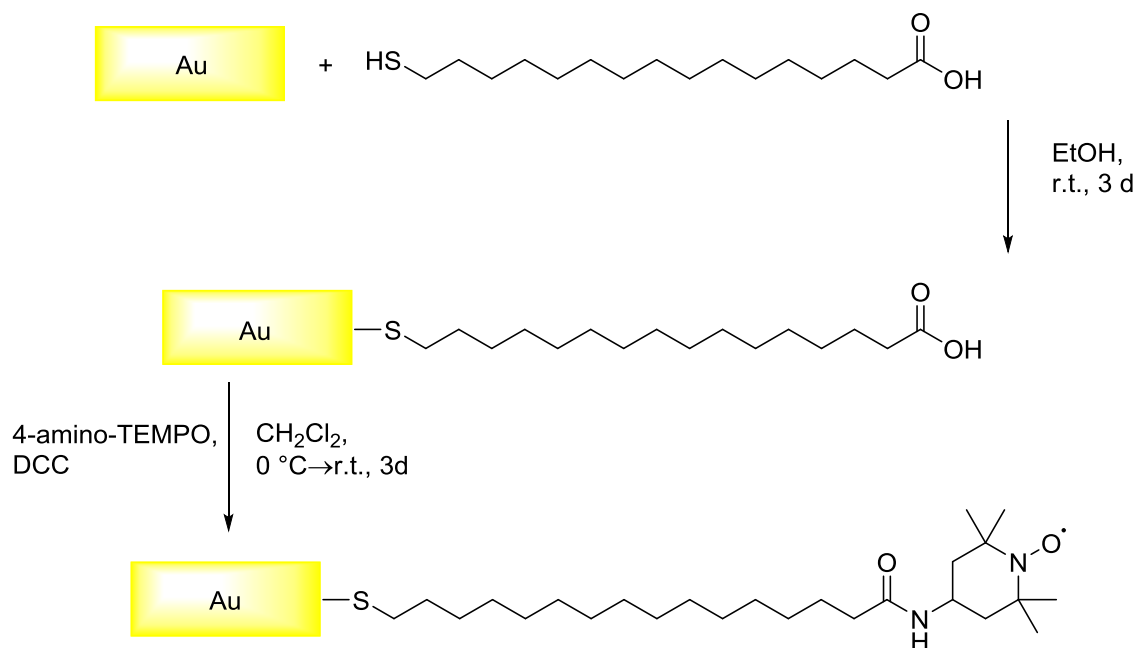
4.6 Synthesis of nitroxide exchange organic framework on gold surface

For the framework synthesis on gold surfaces, self-assembled monolayers (abbreviated as SAM) with TEMPO as head group were prepared.



Scheme 61: Synthesis of acetylthiol-C₁₆-TEMPO.

To synthesize TEMPO functionalized SAM, 16-mercaptohexadecanoic acid (abbreviated as MHDA) was used as precursor. Glacial acid was used to oxidized Zn to Zn²⁺, which active the acetyl chloride for the protection of the thiol group. The acetyl-protected thiol was then transformed to acetylthiol-C₁₆-TEMPO using 4-amino-TEMPO, which undergone an amide linkage with the carboxylic acid group of the acetyl-protected thiol.



Scheme 62: Direct synthesis of C₁₆-TEMPO-SAM on MHDA functionalized gold substrate.

Two approaches were investigated to functionalize the gold surfaces with the desired C₁₆-TEMPO-SAM. The first approach was the immersion of gold substrate directly in C₁₆-TEMPO SAM solution. Like the Surface-mounted Metal Organic Framework (SURMOF) synthesis, the immersion time was chosen to be 3 days. As shown in Scheme 62, the second approach was the subsequent treatment of the MHDA functionalized gold substrate with 4-amino-TEMPO.

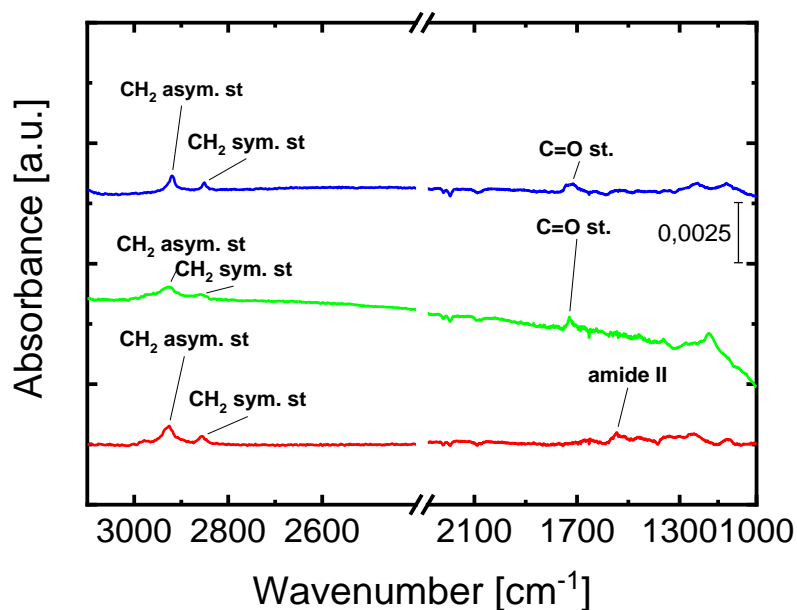
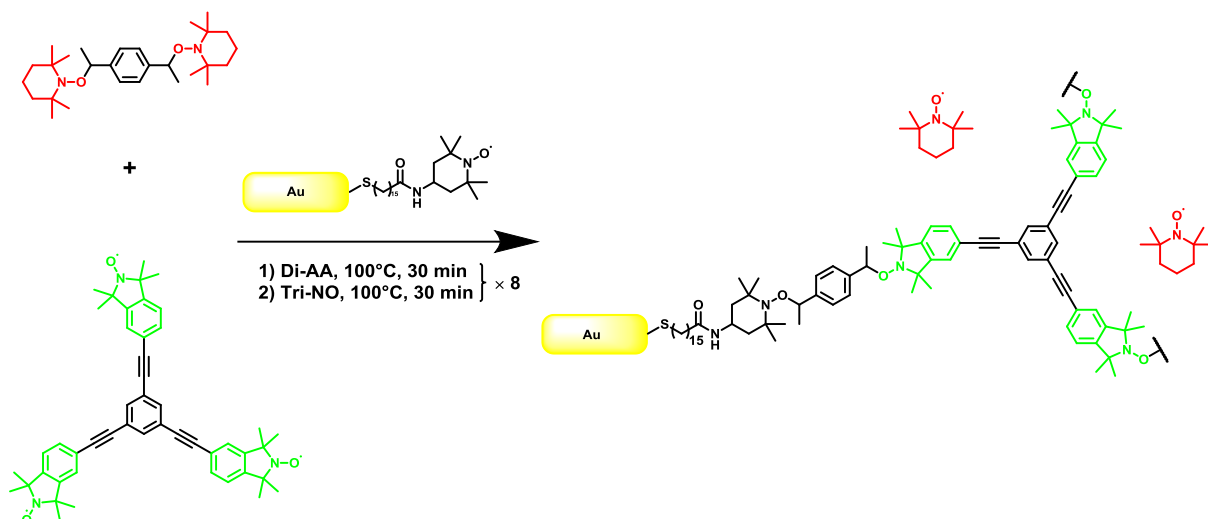


Figure 44: IRRA spectra of functionalized gold substrates. MHDA functionalized gold-substrate (blue), subsequent treatment of MHDA functionalized gold substrate with 4-amino-TEMPO (green), direct functionalization with C₁₆-TEMPO-SAM (red).

To prove the presence of the SAM on the gold substrate, IRRAS was measured (Figure 44). In the blue spectra, the MHDA functionalized gold surface is shown. In the green spectra, the subsequent treated MHDA functionalized gold substrate is shown. The red spectra show the direct functionalization of C₁₆-TEMPO SAM on the gold surface. In all three spectra, asymmetric as well as the symmetric CH₂ stretching vibration was observed. In the blue and green spectra, the carbonyl stretching vibration of the carboxyl group was identified. However, characteristic bands of amide groups could not be observed. Unlike the previous spectra, amide band was observed in the red spectra. It was assumed, that the subsequent functionalization of 4-amino-TEMPO was not covering all carboxylic acid, which resulting in a low intensity of the band.

Therefore, Time of Flight – Secondary Ion Mass spectrometry (abbreviated as TOF-SIMS) as a highly sensitive surface characterization method of monolayers was used. As a negative prove, MHDA SAM was first investigated, which show a negligible intensity of the CNO-fragment. Due to the high intensity of CNO fragment in the C₁₆-TEMPO functionalized substrate, the existence of the subsequent functionalization was proven.



Scheme 63: Layer by layer synthesis of Di-AA and Tri-NO on C_{16} -TEMPO-SAM at 100°C .

Using the layer by layer method, the SURNEN synthesis was implemented in inert atmosphere with Di-AA and Tri-NO. Due to the fact, that the SAM was functionalized with TEMPO as head group, Di-AA was added first into the reaction vessel followed by Tri-NO. In the previous EPR investigation, it was proven, that the exchange reaction already starts after 15 minutes. Therefore, reaction time was set 30 minutes between each step. After 8 cycles, the sample was washed with ethanol and dried in a nitrogen flow. The sample was then investigated with IRRAS. It was observed, that the asymmetric and symmetric stretching vibrations vanished. In the region between 1200 cm^{-1} to 1800 cm^{-1} , some bands can be observed which indicate the presence of aromatic systems.

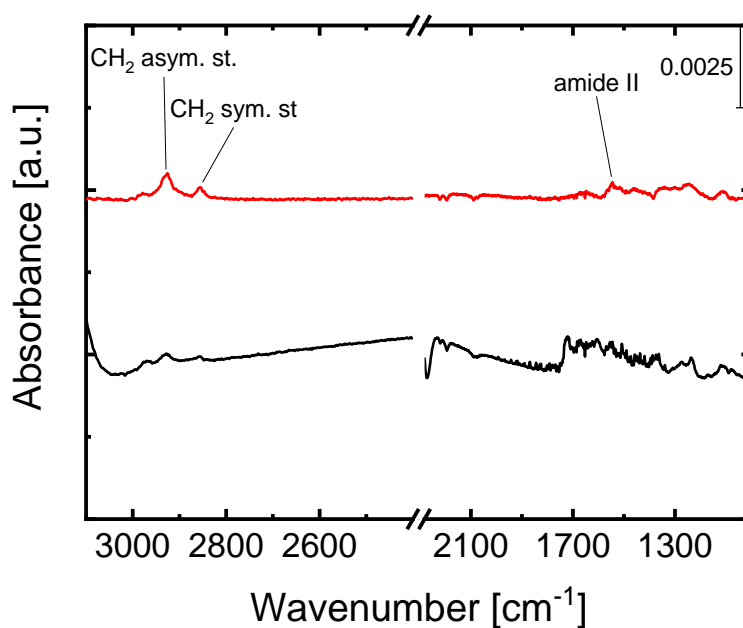


Figure 45: IRRAS spectra of the C_{16} -TEMPO-SAM functionalized gold substrates (red) and the layer by layer synthesized SURNEN.

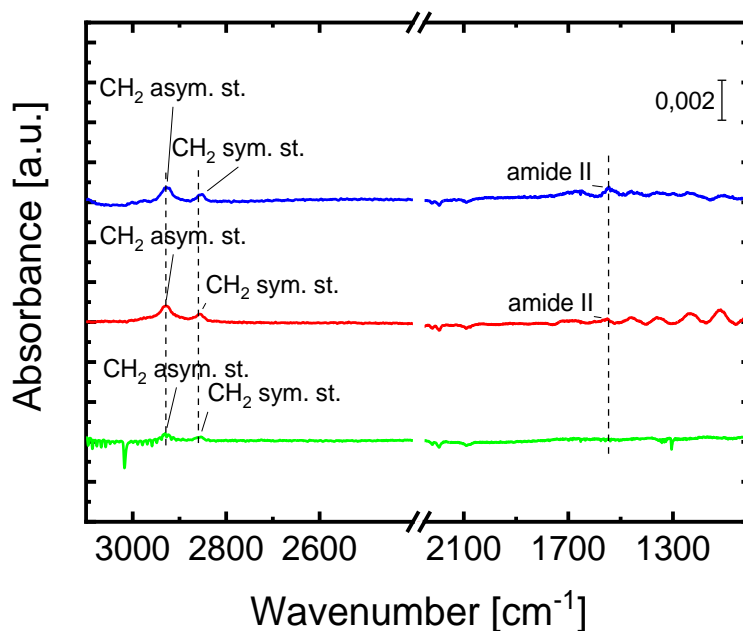


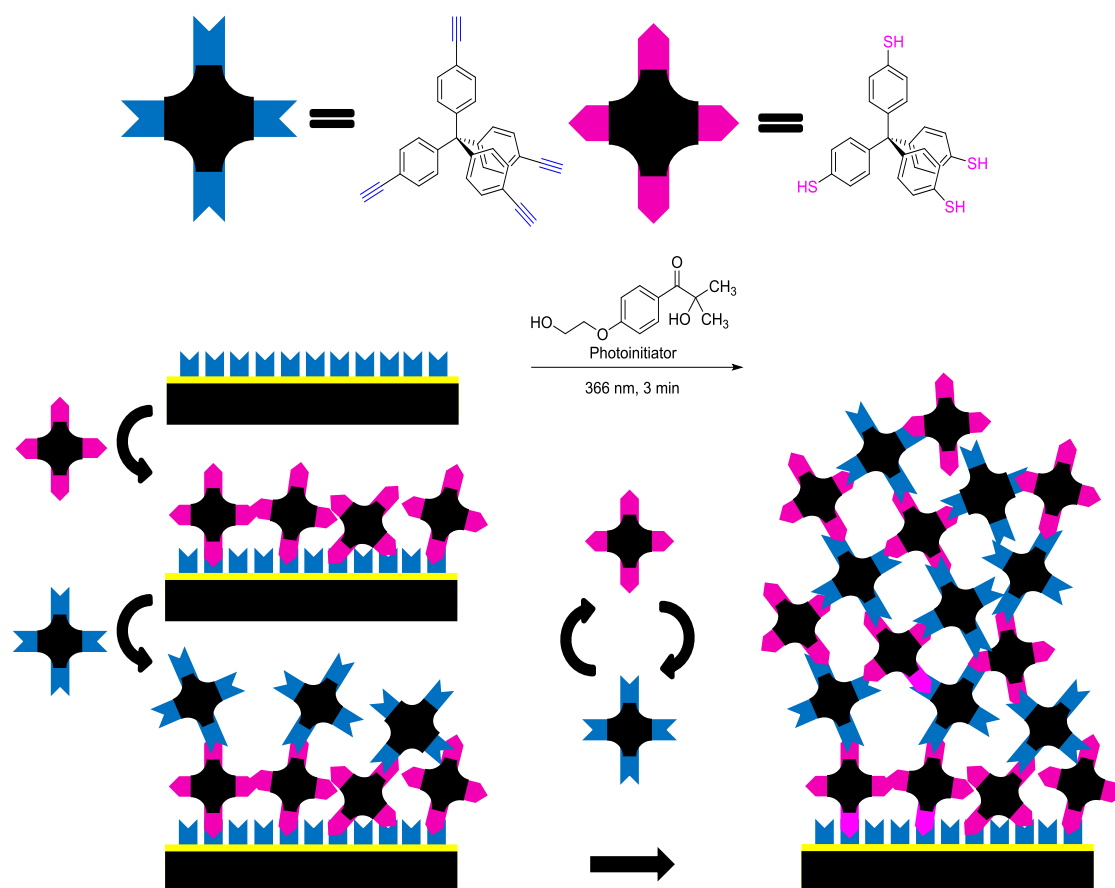
Figure 46: IRRA spectra of C_{16} -TEMPO-functionalized gold substrate, at room temperature (blue), at 80 °C (red) and at 100 °C (green)

Due to the low signal to noise ratio in the IRRA spectra, no convincing statement of the successful layer by layer synthesis could be made. Therefore, systematic investigation of the whole layer by layer synthesis was performed. The first point to consider is the stability of the C_{16} -TEMPO-SAM on the gold surface. To investigate the stability, C_{16} -TEMPO functionalized gold substrates were exposed to different temperatures and characterized by IRRAS. As shown in Figure 46, the amide band was still visible at 80 °C, however at 100 °C, the region between 1200 to 1800 cm^{-1} was completely flat and the intensity of the asymmetric and symmetric CH_2 band has been decreased. As the amide band as well as the CH_2 -stretching bands are both vanishing, a breaking of the amide bond next to the TEMPO moiety can be excluded. A total removal of the SAM by bond breakage near the sulfur anchor group explains the experimental results. Therefore, due to the thermal instability of the C_{16} -TEMPO-SAM on the gold surface, either more stable SAM need to be designed or other milder and specific synthesis approach need to be used.

In this chapter, the synthesis of nitroxide exchange organic framework thin films were introduced. For the thin film synthesis, SAMs with TEMPO as head groups were successfully synthesized. However, the synthesis of nitroxide exchange organic framework as thin film failed. The reason for the failure was the thermal instability of the synthesized C_{16} -TEMPO-SAM. To overcome the problem of thermal instability, the approach of thin film synthesis requires a different layer by layer method. Using the already introduced multifold alkoxyamine and nitroxides, the light induced synthesis is not possible due to the missing sensitizer group. Therefore, new building blocks have to be designed. In the meantime, the light induced layer by layer method was developed using the thiol-yne couplings reaction.

4.7 Synthesis of freestanding thiol-yne coupling thin films

For the synthesis of the CMP nanomembrane, gold coated substrate was immersed into alkyne functionalized SAM solution for 1 day. Comparing with the previous system based on thermal induction, this approach is light induced. In the first step, the SAM functionalized substrate was immersed in a solution of tetravalent thiol building block (abbreviated as TPM-SH) and a small amount of photo initiator (2-hydroxy-4'-(2-hydroxyethoxy)-2-methylpropanone), Afterwards, the substrate was irradiated using a standard UV lamp with a wavelength of 365 nm for 3 minutes. The substrate was then rinsed thoroughly with absolute THF and immersed into the solution of tetravalent alkyne building block (abbreviated as TPM-alkyne) with a small amount of the photo initiator. The substrate was again irradiated for 3 minutes and rinsed afterwards with absolute THF. This procedure was repeated for 20 cycles to obtain the thin film on the functionalized gold surface. To verify the synthesis, IRRAS was measured to detect the characteristic bands of the TYC thin film.



Scheme 64: Layer-by-layer synthesis of TPM-SH and TPM-alkyne using light induced thiol-yne coupling reaction (TYC) in presence of the photoinitiator 2-hydroxy-4'-(2-hydroxyethoxy)-2-methylpropanone. [Q. An, Y. Hassan, X. Yan, P. Krolla-Sidenstein, T. Mohammed, M. Lang, S. Bräse and M.I Tsotsalas, *Beilstein J. Org. Chem.*, 2017, 13, 558-563. Fast and efficient synthesis of microporous polymer nanomembranes via light-induced click reaction] - Published by Beilstein-Institut under the CC BY 4.0 license ^[99]

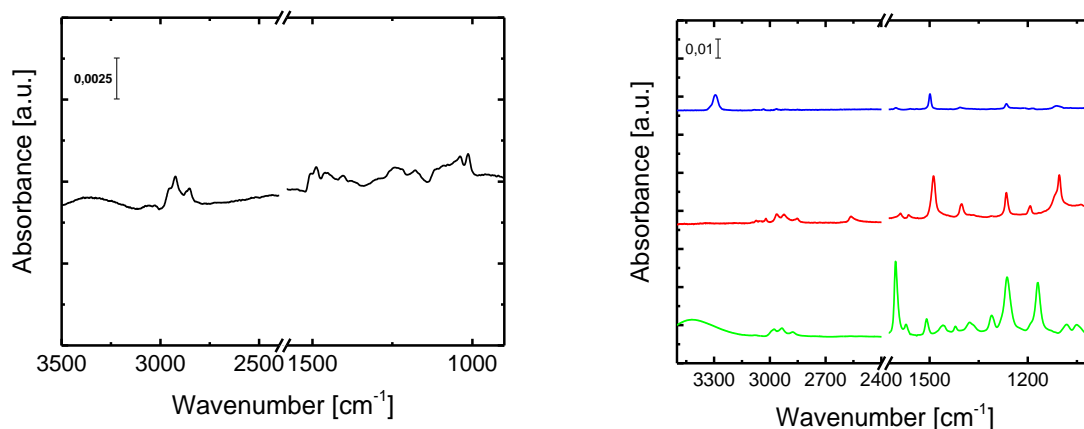


Figure 47: Left) IRRA spectrum of the TYC thin film on a gold coated silicon wafer (black). Right) IRRA spectra of the drop casted TPM-alkyne (blue), TPM-SH (red) and photo initiator (green). [Q. An, Y. Hassan, X. Yan, P. Krolla-Sidenstein, T. Mohammed, M. Lang, S. Bräse and M.I Tsotsalas, *Beilstein J. Org. Chem.*, 2017, 13, 558-563. Fast and efficient synthesis of microporous polymer nanomembranes via light-induced click reaction] - Published by Beilstein-Institut under the CC BY 4.0 license ^[99]

As reference, TPM-alkyne, TPM-SH and the photo initiator were also measured via IRRAS, which are shown in Figure 47 (right side). By comparing the IRRA spectra, a clear absence of the bands associated to alkyne and thiol functional groups was observed on the TYC thin film which indicate an almost quantitative reaction.

To evaluate the thickness of the TYC thin film, ellipsometry was used first. The measurements show an average thickness of about 25.1 ± 0.1 nm with a mean squared error (abbreviated as MSE) value of 5.69 after fitting with Cauchy mode, with the parameters $A_n=1.399$, $B_n=0.051$, $C_n=-0.0026$, k-amplitude=0 and exponent=1.5 suggesting a very low surface roughness. To confirm the thickness, the thin film was measured with AFM. Prior the AFM measurement, the thin film was coated with a stabilizing layer of polymethyl methacrylate (abbreviated as PMMA). Upon substrate dissolution, the PMMA stabilized TYC thin film was transferred to a fresh gold substrate. After drying, the PMMA layer was dissolved in acetone, leaving only the pure TYC thin film on the fresh substrate. Using line scan along the edge of film, the thickness was determined to be also roughly 20 nm.

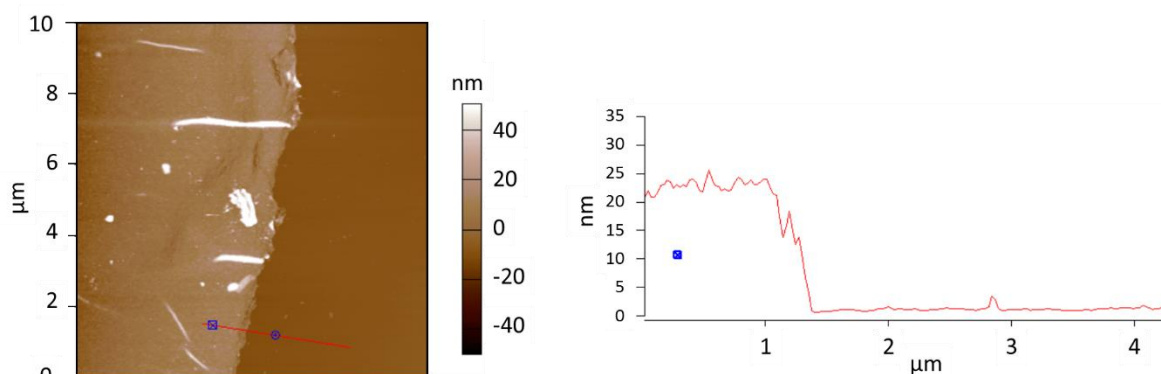


Figure 48: AFM image and line-scan across the edge of the TYC thin film. [Q. An, Y. Hassan, X. Yan, P. Krolla-Sidenstein, T. Mohammed, M. Lang, S. Bräse and M.I Tsotsalas, *Beilstein J. Org. Chem.*, 2017, 13, 558-563. Fast and efficient synthesis of microporous polymer nanomembranes via light-induced click reaction] - Published by Beilstein-Institut under the CC BY 4.0 license ^[99]

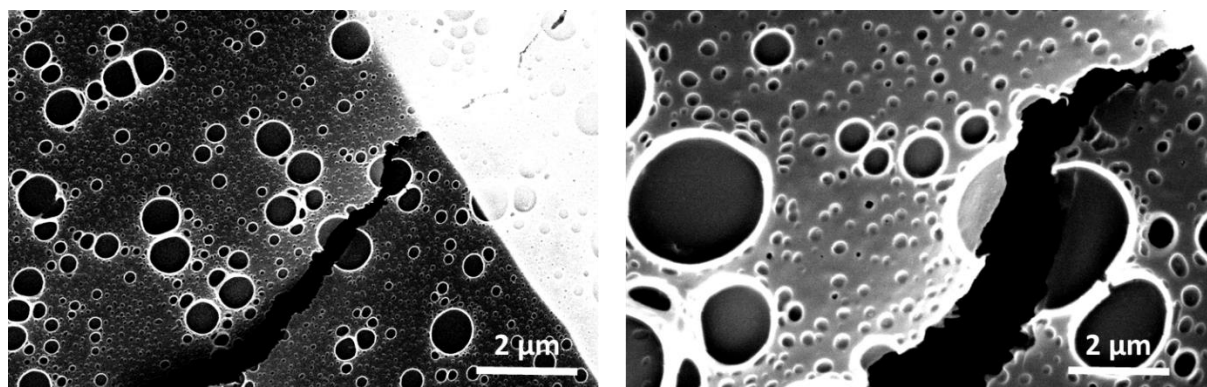


Figure 49: SEM images of freestanding TYC nanomembranes coated with a stabilizing PMMA layer containing large holes. [Q. An, Y. Hassan, X. Yan, P. Krolla-Sidenstein, T. Mohammed, M. Lang, S. Bräse and M.I Tsotsalas, *Beilstein J. Org. Chem.*, 2017, 13, 558-563. Fast and efficient synthesis of microporous polymer nanomembranes via light-induced click reaction] - Published by Beilstein-Institut under the CC BY 4.0 license^[99]

In order to produce freestanding thin film, the TYC thin film was spin coated with a dichloromethane (DCM) solution containing PMMA and PS in weight ratio of PMMA/PS = 8/2. During the spin-coating, the PS phase separates into islands, which then were selectively dissolved using cyclohexane. After the detachment of the sacrificial substrate, the freestanding thin film was obtained. For microscopic investigation, the thin film was transferred to a copper grid. Using scanning electron microscopy (abbreviated as SEM), images of the thin film were recorded, as shown in Figure 49.

In this chapter, the synthesis nanoscale thin film via photo-induced thiol-yne couplings reaction was introduced. This TYC thin film was synthesized via fast and efficient light induced layer by layer method, which can be also applied on other light induced systems in the future. The TYC reaction allows a rapid synthesis of homogeneous thin films with a thickness of about 1 nm per reaction cycle. Along with the possibility to transfer the thin film to any support, the TYC based thin film can be used in functional devices for applications gas or liquid phase separation or organic electronics.

5. Conclusion and Outlook

In this Ph.D. thesis, nitroxide exchange reaction was implemented for the first time to generate dynamic covalent organic frameworks directly by stitching modular multi-fold alkoxyamine and nitroxide as molecular components of defined structure.

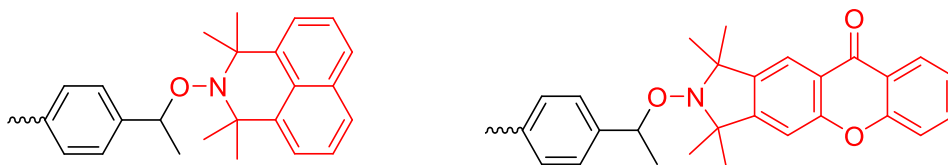
Overall, nine different combinations of nitroxides and alkoxyamines for the synthesis of nitroxide exchange frameworks have been investigated. Seven out of nine combinations (AA and NO), successfully produced frameworks under the tested conditions, while the reaction between Di-AA and Tri-NO and the reaction between Tri-AA and Di-NO were not successful. The following combinations produce gels with comparable medium to low porosity: Di-AA with Tetra-[C]-NO and Tri-AA with Tri-NO. Unlike these combinations, the following combinations produce organic frameworks with high porosity: Tri-AA with Tetra-[C]-NO; Tetra-AA with Tri-NO; Tetra-AA with Tetra-[C]-NO and Tetra-AA with Tetra-[S]-NO. With all synthesized frameworks, the crosslinking degree can be reversibly controlled over the reaction equilibrium by selective removal or addition of a specific amounts of the by-product TEMPO nitroxide. The control over the equilibrium results in a reversible modification of the chemical and physical properties of the framework e.g. crosslinking degree, swelling degree, fluorescence and porosity.

Furthermore, an initial experiment to merge between nitroxide exchange reaction and nitroxide mediated polymerization were performed to form crosslinked polymer materials. For that, well defined two arm- and three arm-polystyrene based on Di- and Tri- alkoxyamines were synthesized. Higher glass transition temperature was found after the exchange reaction with multifold nitroxides, which indicates crosslinking of the building blocks.

Beyond that, EPR spectroscopy was established as a suitable characterization method to monitor *in situ* the reaction progress, due to the different hyperfine coupling constants of various nitroxide moieties. By using EPR spectroscopy, ratios of nitroxide mixtures can be quantified. The side groups on the alkoxyamines were discovered to significantly influence the reaction kinetics of the exchange reaction.

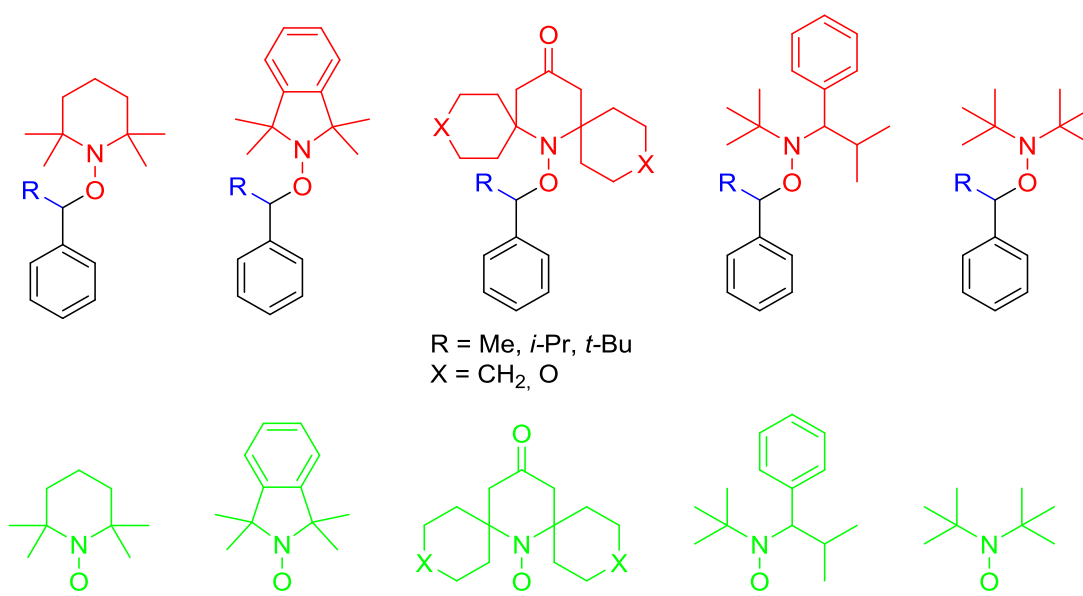
Additionally, the nitroxide exchange reaction was also attempted with the layer by layer method on TEMPO functionalized substrates to produce freestanding thin films. However, due to the thermal instability of the used TEMPO functionalized SAM, the thin film synthesis was not successful. As proof of concept, thiol-yne reaction was chosen as model system to establish the photochemical layer by layer synthesis method. According to IR and AFM measurements, TYC thin film was successfully synthesized via fast and efficient photo chemical layer by layer synthesis. This can be analogically used

on other photo induced systems, e.g. photo induced nitroxide exchange reaction. Scheme 65 shows possible alkoxyamine molecules suitable for the light induced synthesis method.



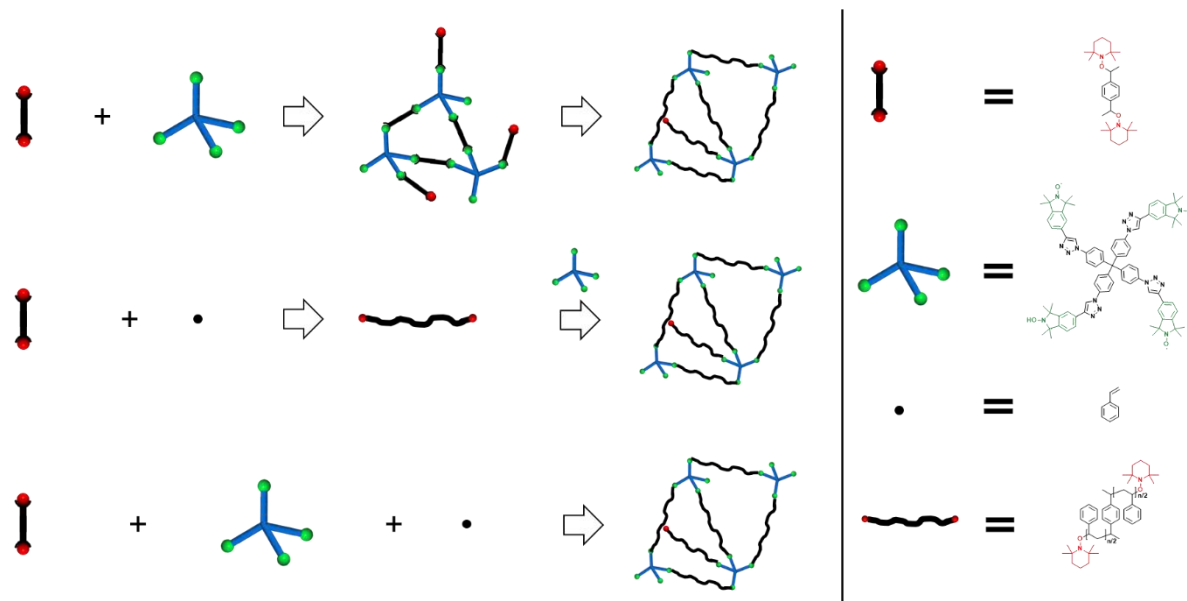
Scheme 65: Examples of alkoxyamine molecules suitable for the photo induced nitroxide exchange reaction.

Using the experimental EPR investigations and quantum chemical calculations, library of model systems consists of different mono alkoxyamines and nitroxides can be built to specifically design suitable building blocks for the frameworks synthesis. Scheme 66 shows the possible mono alkoxyamines and nitroxide for the nitroxide exchange library.



Scheme 66: Up) alkoxyamine with different side group (blue) and different leaving nitroxide (red). Bottom) Different additional nitroxide for the exchange reaction.

To enhance the crystallinity, either completely planar or enantiopure building blocks should be rational. Also, the implementation of photoactive functional groups on the building blocks would allow photoinduced synthesis to a bulk framework as well as on the different functionalized surfaces. Furthermore, mechanical measurements e.g. nano indentation, rheology and stress strain investigation can be considered to determine the mechanical property of the framework materials. It is also possible to explore the application as catalyst on the defect site of the already existing highly porous framework.



Scheme 67: Different approaches for the synthesis of crosslinked polystyrene.

Beside the already introduced crosslinking reaction for the synthesis of crosslinked polystyrene (Scheme 67 (ii)), two other approaches could be also considered in the future to extending the network strands. One way is to form a framework via nitroxide exchange reaction and then add the monomer to the framework upon heating (Scheme 67 (i)). The other way is to do the polymerization and the framework synthesis in a one pot approach (Scheme 67 (iii)). Comparing all three approaches, the most promising route can be chosen to synthesize higher ordered crosslinked polymer framework with homogeneous mesh size for further application tests, like separation of bio macromolecule.

6. Abbreviation

[C]-NO	Click-Nitroxide
[S]-NO	Sonogashira-Nitroxide
°	degree
°C	degree Celsius
µm	micrometer
2D	two dimensional
3D	three dimensional
Å	Angstrom
AA	Alkoxyamine
AcOH	Acetic acid
AFM	Atomic Force Microscopy
Ag	Silver
aq.	aqueous
ATR	Attenuated Total Reflection
BDBA	1,4-benzenediboronic acids
BDE	bond dissociation energy
BET	Brunauer Emmett Teller
Bn	Benzyl
CL	crosslinking
CLD	Crosslinking Degree
cm	centimeter
CMPs	Conjugated Microporous Polymers
COFs	Covalent Organic Frameworks
Cu	Copper
Cu(OTf) ₂	Copper(II) trifluoromethanesulfonate
CuAAC	Copper(I)-catalyzed Azide-Alkyne Cycloaddition
d	day
dB	decibel
DCC	N,N'-Dicyclohexylcarbodiimide
DCM	Dichloromethane
DEF	N,N-diethylformamide
DMA	Dimethylacetamide

DNA	deoxyribonucleic acid
DSC	Differential Scanning Calorimetry
DtBdP	Di-tert-butylbiphenyl
EI	Electron Ionization
EPR	Electron Paramagnetic Resonance
equiv.	equivalence
ESI-MS	Electrospray Ionization Mass Spectrometry
ESR	Electron Spin Resonance
EtOH	Ethanol
FAB-MS	Fast Atom Bombardment Mass spectrometry
FTIR	Fourier Transform Infrared
G	Gauss
Gd	gadolinium
GPC	Gel Permeation Chromatography
h	hour
HBr	Hydrogen Bromide
HCPs	Hyper Crosslinked Polymers
HHTP	2,3,6,7,10,11-hexahydroxytriphenylene
HOBT	Hydroxybenzotriazole
<i>i</i> Pr	isopropyl
IRRAS	Infrared reflection adsorption spectroscopy
ISC	intersystem crossing
IUPAC	International Union of Pure and Applied Chemistry
K	Kelvin
kHz	kilohertz
KI	Potassium Iodide
KOH	Potassium Hydroxide
lbl	Layer-by-Layer
LiAlH ₄	Lithium aluminium hydride
MALDI	Matrix-Assisted Laser Desorption/Ionization
<i>m</i> CPBA	<i>meta</i> -Chloroperoxybenzoic acid
Me	Methyl
MeCN	Acetonitrile
MeMgI	Methylmagnesium Iodide
MeOH	Methanol

MHDA	16-Mercaptohexadecanoic acid
min	minute
mL	milliliter
mM	millimolar
mmol	millimol
Mo	Molybdenum
MRI	Magnetic Resonance Imaging
ms	milli seconde
MSE	mean squared error
MTSSL	(1-Oxyl-2,2,5,5-tetramethylpyrroline-3-methyl) methanethiosulfonate
N	newton
NER	Nitroxide Exchange Reaction
nm	nanometer
NMP	Nitroxide Mediated Polymerization
NMR	Nuclear Magnetic Resonance
NO	nitroxide
PAFs	Porous Aromatic Frameworks
Pd	Palladium
PDI	Polydispersity Index
PEG	Polyethylene glycol
PMMA	Poly(methyl methacrylate)
PS	Polystyrene
Q	swelling degree
r.t.	room temperature
RNA	ribonucleic acid
SA	Surface Area
SAM	Self-Assembled Monolayer
SE	Spectroscopic Ellipsometry
SEC	size exclusion chromatography
SEM	Scanning Electron Microscopy
S _N	nucleophile substitution
S _N Ar	Nucleophilic aromatic substitution
SURGEL	SURface-mounted Gel
SURMOF	SURface-mounted Metal-Organic Framework
TBPM	tetra(4-dihydroxyborylphenyl)methane

<i>tBu</i>	tertbutyl
TDM	Transition Dipole Moment
TEM	Transmission Electron Microscopy
TEMPO	(2,2,6,6-Tetramethylpiperidin-1-yl)oxyl
TGA	Thermogravimetric Analysis
THF	tetrahydrofuran
TMINO	Tetramethyl Isoindoline Nitroxide
TMS	Tetramethylsilane
ToF-SIMS	Time-of-Flight Secondary Ion Mass Spectrometry
TPM	tetraphenylmethane
TYC	Thiol-yne coupling
UV	Ultraviolet
Xe	Xenon
XRD	X-ray Diffraction

7. References

- [1] N. Roy, B. Bruchmann, J.-M. Lehn, *Chem. Soc. Rev.* **2015**, *44*, 3786, DOI 10.1039/C5CS00194C.
- [2] Y. Jin, Q. Wang, P. Taynton, W. Zhang, *Acc. Chem. Res.* **2014**, *47*, 1575, DOI 10.1021/ar500037v.
- [3] S. J. Rowan, S. J. Cantrill, G. R. L. Cousins, J. K. M. Sanders, J. F. Stoddart, *Angew. Chem. Int. Ed.* **2002**, *41*, 898, DOI 10.1002/1521-3773(20020315)41:6<898::AID-ANIE898>3.0.CO;2-E.
- [4] J.-M. Lehn, *Chem. Eur. J.* **1999**, *5*, 2455, DOI 10.1002/(SICI)1521-3765(19990903)5:9<2455::AID-CHEM2455>3.0.CO;2-H.
- [5] J. Li, J. M. A. Carnall, M. C. A. Stuart, S. Otto, *Angew. Chem. Int. Ed.* **2011**, *50*, 8384, DOI 10.1002/anie.201103297.
- [6] P. Reutenauer, P. J. Boul, J.-M. Lehn, *Eur. J. Org. Chem.* **2009**, 1691, DOI 10.1002/ejoc.200801269.
- [7] a) W. Zhang, J. S. Moore, *Adv. Synth. Catal.* **2007**, *349*, 93, DOI 10.1002/adsc.200600476; b) A. Furstner, P. W. Davies, *Chem. Commun.* **2005**, 2307, DOI 10.1039/B419143A.
- [8] a) G. C. Vougioukalakis, R. H. Grubbs, *Chem. Rev.* **2010**, *110*, 1746, DOI 10.1021/cr9002424; b) A. Fürstner, *Angew. Chem. Int. Ed.* **2000**, *39*, 3012, DOI 10.1002/1521-3773(20000901)39:17<3012::AID-ANIE3012>3.0.CO;2-G.
- [9] M. E. Belowich, J. F. Stoddart, *Chem. Soc. Rev.* **2012**, *41*, 2003, DOI 10.1039/C2CS15305J.
- [10] P. T. Corbett, J. Leclaire, L. Vial, K. R. West, J.-L. Wietor, J. K. M. Sanders, S. Otto, *Chem. Rev.* **2006**, *106*, 3652, DOI 10.1021/cr020452p.
- [11] N. Ponnuswamy, F. B. L. Cougnon, J. M. Clough, G. D. Pantoş, J. K. M. Sanders, *Science* **2012**, *338*, 783, DOI 10.1126/science.1227032.
- [12] a) O. G. Ballesteros, L. Maretti, R. Sastre, J. C. Scaiano, *Macromolecules* **2001**, *34*, 6184, DOI 10.1021/ma0103831; b) C. J. Hawker, G. G. Barclay, J. Dao, *J. Am. Chem. Soc.* **1996**, *118*, 11467, DOI 10.1021/ja9624228.
- [13] A. Studer, *Chem. Eur. J.* **2001**, *7*, 1159, DOI 10.1002/1521-3765(20010316)7:3A6<1159:3A%3AAID-CHEM1159>3.0.CO%3B2-I.
- [14] N. J. Turro, G. Lem, I. S. Zavarine, *Macromolecules* **2000**, *33*, 9782, DOI 10.1021/ma001327n.
- [15] H. Otsuka, K. Aotani, Y. Higaki, Y. Amamoto, A. Takahara, *Macromolecules* **2007**, *40*, 1429, DOI 10.1021/ma061667u.
- [16] I. Wessely, V. Mugnaini, A. Bihlmeier, G. Jeschke, S. Bräse, M. Tsotsalas, *RSC Adv.* **2016**, *6*, 55715, DOI 10.1039/C6RA06510D.
- [17] J. Matko, K. Ohki, M. Edidin, *Biochemistry* **2002**, *31*, 703, DOI 10.1021/BI00118A010.
- [18] G. I. Likhtenstein, K. Ishii, S. Nakatsuji, *Photochem. Photobiol.* **2007**, *83*, 871, DOI 10.1111/J.1751-1097.2007.00141.X.

- [19] J. P. Blinco, K. E. Fairfull-Smith, B. J. Morrow, S. E. Bottle, *Aust. J. Chem.* **2011**, *64*, 373, DOI 10.1071/CH10442.
- [20] B. Schulte, M. Tsotsalas, M. Becker, A. Studer, L. de Cola, *Angew. Chem. Int. Ed.* **2010**, *49*, 6881, DOI 10.1002/anie.201002851.
- [21] David H. Solomon, Ezio Rizzardo, Paul Cacioli, US06629929.
- [22] C. J. Hawker, G. G. Barclay, A. Orellana, J. Dao, W. Devonport, *Macromolecules* **1996**, *29*, 5245, DOI 10.1021/ma951905d.
- [23] K. Matyjaszewski, B. E. Woodworth, X. Zhang, S. G. Gaynor, Z. Metzner, *Macromolecules* **1998**, *31*, 5955, DOI 10.1021/ma9807264.
- [24] D. Benoit, V. Chaplinski, R. Braslau, C. J. Hawker, *J. Am. Chem. Soc.* **1999**, *121*, 3904, DOI 10.1021/ja984013c.
- [25] E. Beaudoin, D. Bertin, D. Gigmes, S. R. A. Marque, D. Siri, P. Tordo, *Eur. J. Org. Chem.* **2006**, *2006*, 1755, DOI 10.1002/ejoc.200500725.
- [26] P. Nesvadba, *CHIMIA* **2006**, *60*, 832, DOI 10.2533/chimia.2006.832.
- [27] McNaught and A. Wilkinson in *IUPAC. Compendium of Chemical Terminology*.
- [28] L. Tebben, A. Studer, *Angew. Chem. Int. Ed.* **2011**, *50*, 5034, DOI 10.1002/anie.201002547.
- [29] L. Columbus, W. L. Hubbell, *Trends. Biochem. Sci.* **2002**, *27*, 288, DOI 10.1016/S0968-0004(02)02095-9.
- [30] J. L. Battiste, G. Wagner, *Biochemistry* **2000**, *39*, 5355, DOI 10.1021/bi000060h.
- [31] G. M. Clore, J. Iwahara, *Chem. Rev.* **2009**, *109*, 4108, DOI 10.1021/cr900033p.
- [32] P. Kuppusamy, P. Wang, R. A. Shankar, L. Ma, C. E. Trimble, C. J. C. Hsia, J. L. Zweier, *Magn. Reson. Med.* **1998**, *40*, 806, DOI 10.1002/mrm.1910400604.
- [33] H. V.-T. Nguyen, Q. Chen, J. T. Paletta, P. Harvey, Y. Jiang, H. Zhang, M. D. Boska, M. F. Ottaviani, A. Jasanoff, A. Rajca et al., *ACS Cent. Sci.* **2017**, *3*, 800, DOI 10.1021/acscentsci.7b00253.
- [34] L. M. Reid, T. Li, Y. Cao, C. P. Berlinguette, *Sustainable Energy Fuels* **2018**, *2*, 1905, DOI 10.1039/C8SE00175H.
- [35] A. E. J. d. Nooy, A. C. Besemer, H. van Bekkum, *Synthesis* **1996**, 1153, DOI 10.1055/s-1996-4369.
- [36] a) K.-A. Hansen, J. P. Blinco, *Polym. Chem.* **2018**, *9*, 1479, DOI 10.1039/C7PY02001E; b) V. Sciannamea, R. Jérôme, C. Detrembleur, *Chem. Rev.* **2008**, *108*, 1104, DOI 10.1021/cr0680540.
- [37] P. Théato, B. S. Sumerlin, R. K. O'Reilly, T. H. Epps, *Chem. Soc. Rev.* **2013**, *42*, 7055, DOI 10.1039/C3CS90057F.
- [38] F. D. Jochum, P. Théato, *Chem. Soc. Rev.* **2013**, *42*, 7468, DOI 10.1039/C2CS35191A.
- [39] M. I. Gibson, R. K. O'Reilly, *Chem. Soc. Rev.* **2013**, *42*, 7204, DOI 10.1039/C3CS60035A.
- [40] J. Huang, A. Heise, *Chem. Soc. Rev.* **2013**, *42*, 7373, DOI 10.1039/C3CS60063G.
- [41] S. Murdan, *J. Control. Release* **2003**, *92*, 1, DOI 10.1016/S0168-3659(03)00303-1.

- [42] X. Yan, F. Wang, B. Zheng, F. Huang, *Chem. Soc. Rev.* **2012**, *41*, 6042, DOI 10.1039/C2CS35091B.
- [43] E. A. Appel, F. Biedermann, U. Rauwald, S. T. Jones, J. M. Zayed, O. A. Scherman, *J. Am. Chem. Soc.* **2010**, *132*, 14251, DOI 10.1021/ja106362w.
- [44] O. Pieroni, A. Fissi, J. L. Houben, F. Ciardelli, *J. Am. Chem. Soc.* **1985**, *107*, 2990, DOI 10.1021/ja00296a036.
- [45] O. Pieroni, A. Fissi, N. Angelini, F. Lenci, *Acc. Chem. Res.* **2001**, *34*, 9, DOI 10.1021/ar990141%2B.
- [46] S. Schmitt, M. Silvestre, M. Tsotsalas, A.-L. Winkler, A. Shahnas, S. Grosjean, F. Laye, H. Gliemann, J. Lahann, S. Bräse et al., *ACS nano* **2015**, *9*, 4219, DOI 10.1021/acsnano.5b00483.
- [47] D. A. Davis, A. Hamilton, J. Yang, L. D. Cremar, D. van Gough, S. L. Potisek, M. T. Ong, P. V. Braun, T. J. Martínez, S. R. White et al., *Nature* **2009**, *459*, 68, DOI 10.1038/nature07970.
- [48] S. K. R. Dronskowski in *Handbook of Solid State Chemistry* (Eds.: R. Dronskowski, S. Kikkawa, A. Stein), Wiley, **2017**, pp. 201–225.
- [49] D. Y. Zhu, M. Z. Rong, M. Q. Zhang, *Prog. Polym. Sci.* **2015**, *49-50*, 175, DOI 10.1016/j.progpolymsci.2015.07.002.
- [50] X. Chen, M. A. Dam, K. Ono, A. Mal, H. Shen, S. R. Nutt, K. Sheran, F. Wudl, *Science* **2002**, *295*, 1698, DOI 10.1126/science.1065879.
- [51] a) S.-Y. Ding, J. Gao, Q. Wang, Y. Zhang, W.-G. Song, C.-Y. Su, W. Wang, *J. Am. Chem. Soc.* **2011**, *133*, 19816, DOI 10.1021/ja206846p; b) P. Thomas, C. Pei, B. Roy, S. Ghosh, S. Das, A. Banerjee, T. Ben, S. Qiu, S. Roy, *J. Mater. Chem. A* **2015**, *3*, 1431, DOI 10.1039/C4TA01304B.
- [52] a) F. Xu, X. Chen, Z. Tang, D. Wu, R. Fu, D. Jiang, *Chem. Commun.* **2014**, *50*, 4788, DOI 10.1039/c4cc01002g; b) F. Xu, H. Xu, X. Chen, D. Wu, Y. Wu, H. Liu, C. Gu, R. Fu, D. Jiang, *Angew. Chem. Int. Ed.* **2015**, *54*, 6814, DOI 10.1002/anie.201501706; c) Y. Li, S. Roy, T. Ben, S. Xu, S. Qiu, *Phys. Chem. Chem. Phys.* **2014**, *16*, 12909, DOI 10.1039/c4cp00550c.
- [53] a) B. Li, Y. Zhang, R. Krishna, K. Yao, Y. Han, Z. Wu, D. Ma, Z. Shi, T. Pham, B. Space et al., *J. Am. Chem. Soc.* **2014**, *136*, 8654, DOI 10.1021/ja502119z; b) P. M. Budd, K. J. Msayib, C. E. Tattershall, B. S. Ghanem, K. Reynolds, McKeown, Neil B. Fritsch, D., *J. Membrane. Sci.* **2005**, *251*, 263, DOI 10.1016/j.memsci.2005.01.009; c) Y. Zhao, K. X. Yao, B. Teng, T. Zhang, Y. Han, *Energy Environ. Sci.* **2013**, *6*, 3684, DOI 10.1039/c3ee42548g.
- [54] a) H. Ma, B. Liu, B. Li, L. Zhang, Y.-G. Li, H.-Q. Tan, H.-Y. Zang, G. Zhu, *J. Am. Chem. Soc.* **2016**, *138*, 5897, DOI 10.1021/jacs.5b13490; b) H. Xu, S. Tao, D. Jiang, *Nat. Mater.* **2016**, *15*, 722, DOI 10.1038/nmat4611.
- [55] a) R. S. Sprick, J.-X. Jiang, B. Bonillo, S. Ren, T. Ratvijitvech, P. Guiglion, M. A. Zwijnenburg, D. J. Adams, A. I. Cooper, *J. Am. Chem. Soc.* **2015**, *137*, 3265, DOI 10.1021/ja511552k; b) V. S. Vyas, F. Haase, L. Stegbauer, G. Savasci, F. Podjaski, C. Ochsenfeld, B. V. Lotsch, *Nat. Commun.* **2015**, *6*,

- 8508, DOI 10.1038/ncomms9508; c) K. V. Rao, R. Haldar, T. K. Maji, S. J. George, *Phys. Chem. Chem. Phys.* **2016**, *18*, 156, DOI 10.1039/C5CP05052A.
- [56] T. Tozawa, J. T. A. Jones, S. I. Swamy, S. Jiang, D. J. Adams, S. Shakespeare, R. Clowes, D. Bradshaw, T. Hasell, S. Y. Chong et al., *Nat. Mater.* **2009**, *8*, 973 EP -.
- [57] N. B. McKeown, P. M. Budd, *Macromolecules* **2010**, *43*, 5163, DOI 10.1021/ma1006396.
- [58] P. M. Budd, B. S. Ghanem, S. Makhseed, N. B. McKeown, K. J. Msayib, C. E. Tattershall, *Chem. Commun.* **2004**, 230, DOI 10.1039/B311764B.
- [59] A. P. Côté, A. I. Benin, N. W. Ockwig, M. O'Keeffe, A. J. Matzger, O. M. Yaghi, *Science* **2005**, *310*, 1166, DOI 10.1126/science.1120411.
- [60] H. M. El-Kaderi, J. R. Hunt, J. L. Mendoza-Cortés, A. P. Côté, R. E. Taylor, M. O'Keeffe, O. M. Yaghi, *Science* **2007**, *316*, 268, DOI 10.1126/science.1139915.
- [61] M. G. Rabbani, A. K. Sekizkardes, Z. Kahveci, T. E. Reich, R. Ding, H. M. El-Kaderi, *Chem. Eur. J.* **2013**, *19*, 3324, DOI 10.1002/chem.201203753.
- [62] F. J. Uribe-Romo, J. R. Hunt, H. Furukawa, C. Klöck, M. O'Keeffe, O. M. Yaghi, *J. Am. Chem. Soc.* **2009**, *131*, 4570, DOI 10.1021/ja8096256.
- [63] L. Stegbauer, K. Schwinghammer, B. V. Lotsch, *Chem. Sci.* **2014**, *5*, 2789, DOI 10.1039/C4SC00016A.
- [64] P. Kuhn, M. Antonietti, A. Thomas, *Angew. Chem. Int. Ed.* **2008**, *47*, 3450, DOI 10.1002/anie.200705710.
- [65] J. Guo, Y. Xu, S. Jin, L. Chen, T. Kaji, Y. Honsho, M. A. Addicoat, J. Kim, A. Saeki, H. Ihee et al., *Nat. Commun.* **2013**, *4*, 2736, DOI 10.1038/ncomms3736.
- [66] S. Dalapati, S. Jin, J. Gao, Y. Xu, A. Nagai, D. Jiang, *J. Am. Chem. Soc.* **2013**, *135*, 17310, DOI 10.1021/ja4103293.
- [67] J.-X. Jiang, F. Su, A. Trewin, C. D. Wood, N. L. Campbell, H. Niu, C. Dickinson, A. Y. Ganin, M. J. Rosseinsky, Y. Z. Khimyak et al., *Angew. Chem. Int. Ed.* **2007**, *46*, 8574, DOI 10.1002/anie.200701595.
- [68] R. Dawson, F. Su, H. Niu, C. D. Wood, J. T. A. Jones, Y. Z. Khimyak, A. I. Cooper, *Macromolecules* **2008**, *41*, 1591, DOI 10.1021/ma702411b.
- [69] J.-X. Jiang, F. Su, H. Niu, C. D. Wood, N. L. Campbell, Y. Z. Khimyak, A. I. Cooper, *Chem. Commun.* **2008**, 486, DOI 10.1039/B715563H.
- [70] J. Weber, A. Thomas, *J. Am. Chem. Soc.* **2008**, *130*, 6334, DOI 10.1021/ja801691x.
- [71] L. Chen, Y. Honsho, S. Seki, D. Jiang, *J. Am. Chem. Soc.* **2010**, *132*, 6742, DOI 10.1021/ja100327h.
- [72] J. Schmidt, M. Werner, A. Thomas, *Macromolecules* **2009**, *42*, 4426, DOI 10.1021/ma9005473.
- [73] J. Schmidt, J. Weber, J. D. Epping, M. Antonietti, A. Thomas, *Adv. Mater.* **2009**, *21*, 702, DOI 10.1002/adma.200802692.

- [74] J. Xia, S. Yuan, Z. Wang, S. Kirklin, B. Dorney, D.-J. Liu, L. Yu, *Macromolecules* **2010**, *43*, 3325, DOI 10.1021/ma100026f.
- [75] O. Kahn, *Molecular magnetism*, VCH, New York, NY, **1993**.
- [76] M. Thommes, K. Kaneko, A. V. Neimark, J. P. Olivier, F. Rodriguez-Reinoso, J. Rouquerol, K. S. Sing, *Pure. App. Chem.* **2015**, *87*, 160, DOI 10.1515/pac-2014-1117.
- [77] S. Lowell, *Characterization of porous solids and powders. Surface area, pore size and density*, Springer, Dordrecht, **2010**.
- [78] K. S. W. Sing, *Pure. App. Chem.* **1985**, *57*, 603, DOI 10.1351/pac198557040603.
- [79] Z. AlOthman, *Materials* **2012**, *5*, 2874, DOI 10.3390/ma5122874.
- [80] I. Langmuir, *J. Am. Chem. Soc.* **1918**, *40*, 1361, DOI 10.1021/ja02242a004.
- [81] S. Brunauer, P. H. Emmett, E. Teller, *J. Am. Chem. Soc.* **1938**, *60*, 309, DOI 10.1021/ja01269a023.
- [82] a) B. H. Stuart, *Infrared spectroscopy. Fundamentals and applications*, Wiley, Chichester, **2008**; b) N. B. Colthup, L. H. Daly, S. E. Wiberly, *Introduction to infrared and Raman spectroscopy*, Academic Press, San Diego, Calif., **1998**.
- [83] H. Günzler, H.-U. Gremlich, *IR-Spektroskopie. Eine Einführung*, Wiley-VCH, Weinheim, **2012**.
- [84] H. Fujiwara, *Spectroscopic ellipsometry. Principles and applications*, Wiley, Chichester, **2009**.
- [85] K. N. de Oliveira, P. Costa, J. R. Santin, L. Mazzambani, C. Bürger, C. Mora, R. J. Nunes, M. M. de Souza, *Bioorgan. Med. Chem.* **2011**, *19*, 4295, DOI 10.1016/j.bmc.2011.05.056.
- [86] P. G. Griffiths, G. Moad, E. Rizzardo, *Aust. J. Chem.* **1983**, *36*, 397, DOI 10.1071/CH9830397.
- [87] K. S. Chan, X. Z. Li, S. Y. Lee, *Organometallics* **2010**, *29*, 2850, DOI 10.1021/om1000869.
- [88] K. E. Fairfull-Smith, E. A. Debele, J. P. Allen, M. C. Pfrunder, J. C. McMurtrie, *Eur. J. Org. Chem.* **2013**, *2013*, 4829, DOI 10.1002/ejoc.201300313.
- [89] O. L. Plietzsch, *Dissertation*, Logos Verlag Berlin, **2010**.
- [90] I. Wessely, *Dissertation*, Logos Verlag Berlin, **2017**.
- [91] M. Kleinert, T. Winkler, A. Terfort, T. K. Lindhorst, *Org. Biomol. Chem.* **2008**, *6*, 2118, DOI 10.1039/B801595C.
- [92] M. Lang, *Dissertation*, Logos Verlag Berlin, **2018**.
- [93] M. Ai, S. Shishatskiy, J. Wind, X. Zhang, C.T. Nottbohm, N. Mellech, A. Winter, H. Vieker, J. Qiu, K. Dietz et al., *Adv. Mater.* **2014**, *26*, 3421, DOI 10.1002/adma.201304536.
- [94] H. Zhang, S. Takeoka, *Macromolecules* **2012**, *45*, 4315, DOI 10.1021/ma3005394.
- [95] Q. An, I. D. Wessely, Y. Matt, Z. Hassan, S. Bräse, M. Tsotsalas, *Polym. Chem.* **2019**, *10*, 672, DOI 10.1039/C8PY01474D.
- [96] J.-X. Jiang, F. Su, A. Trewin, C. D. Wood, H. Niu, J. T. A. Jones, Y. Z. Khimyak, A. I. Cooper, *J. Am. Chem. Soc.* **2008**, *130*, 7710, DOI 10.1021/ja8010176.

- [97] G. Madras, G. Y. Chung, J. M. Smith, B. J. McCoy, *Ind. Eng. Chem. Res.* **1997**, *36*, 2019, DOI 10.1021/ie9607513.
- [98] S. Matsushima, A. Takano, Y. Takahashi, Y. Matsushita, *J. Polym. Sci. Part B: Polym. Phys.* **2017**, *55*, 757, DOI 10.1002/polb.24326.
- [99] Q. An, Y. Hassan, X. Yan, P. Krolla-Sidenstein, T. Mohammed, M. Lang, S. Bräse, M. Tsotsalas, *Beilstein J. Org. Chem.* **2017**, *13*, 558, DOI 10.3762/bjoc.13.54.

8. Attachment

8.1 CV

Personal data

Name: Qi An
Title: M.Sc.
Nationality: German
Status: Married

Education

01/2016 – 05/2019 Karlsruhe Institute of Technology (KIT)
Expected degree: Dr. rer. nat.
Field of study: Organic chemistry
Supervisor: Dr. Manuel Tsotsalas
Topic of the thesis: *Synthesis and characterization of dynamic covalent materials*

10/2014 – 12/2015 Karlsruhe Institute of Technology (KIT)
Degree: M.Sc. Chemistry, Grade: 1.8
Field of study: Chemistry / Organic chemistry
Supervisor: Prof. Dr. Stefan Bräse
Topic of thesis: *Aufbau organischer Netzwerke mittels Nitroxid Austausch Reaktion*

10/2010 – 10/2014	Karlsruhe Institute of Technology (KIT) Degree: B.Sc. Chemistry, Grade: 2.3 Field of study: Chemistry / Inorganic chemistry Supervisor: Prof. Dr. Peter Roesky Topic of thesis: <i>Synthese eines neuen Aminotropinimin-Liganden</i>
2004 – 2010	Otto Hahn Gymnasium Degree: Abitur, Grade: 3.0
2002 – 2004	Schiller Schule Karlsruhe (Vorbereitungsklasse)
1997 – 2002	Jinmen-Grundschule Qingdao

8.2 Publications

An, Q.; Hassan, Y.; Yan, X.; Krolla-Sidenstein, P.; Mohammed, T.; Lang, M.; Bräse, S.; Tsotsalas, M. Fast and efficient synthesis of microporous polymer nanomembranes via light-induced click reaction. *Beilstein Journal of Organic Chemistry* **2017**, *13*, 558-563, DOI: 10.3762/bjoc.13.54.

Fischer, T. S.; Spann, S.; An, Q.; Luy, B.; Tsotsalas, M.; Blinco, J. P.; Mutlu, H.; Barner-Kowollik C. Self-reporting and Refoldable Profluorescent Single-Chain Nanoparticles. *Chem. Sci.* **2018**, *9*, 4696-4702. DOI: 10.1039/c8sc01009a

An, Q.; Wessely, I. D.; Matt, Y.; Hassan, Z.; Bräse, S.; Tsotsalas, M. Recycling and self-healing of dynamic covalent polymer networks with a precisely tuneable crosslinking degree. *Polym. Chem.* **2019**, *10*, 672-678. DOI: 10.1039/C8PY01474D

Wessely, I. D.; An, Q.; Matt, Y.; Bräse, S.; Tsotsalas, M. Synthesis of Porous Organic Polymer via Nitroxide Exchange Reaction with tuneable Porosity. *in preparation*.

Sulzer, D.; Matt, Y.; An, Q.; Tsotsalas, M.; Bräse, S.; Bihlmeier, A. Quantum Chemical investigation of Side Group effect in Nitroxide Exchange Reaction. *in preparation*.

8.3 Conference contributions as oral presentations

An, Q.; Matt, Y.; Wessely, I. D.; Bräse, S.; Tsotsalas, M.; Synthesis of Stimuli-Responsive and Self-healing Porous Polymers via Dynamic Nitroxide Exchange Reaction, 6th International Conference on Metal-Organic Frameworks & Open Framework Compounds, Auckland (New Zealand), 2018.

8.4 Conference contributions as poster presentations

An, Q.; Wessely, I. D.; Weidler, P.; Krolla-Sidenstein, P.; Gliemann, H.; Wöll, C.; Tsotsalas, M. Reversible Nitroxide Exchange Reaction for the Synthesis of Covalent Organic Frameworks, 5th International Conference on Metal-Organic Frameworks & Open Framework Compounds, Long Beach (USA), 2016.

An, Q.; Wessely, I. D.; Weidler, P.; Tsotsalas, M. Reversible Nitroxide Exchange Reaction for the Synthesis of Porous Organic Polymers, 2nd European Conference on Metal-Organic Frameworks and Porous Polymer, Delft (The Netherlands), 2017.

An, Q.; Wessely, I. D.; Matt, Y.; Hassan, Z.; Bräse, S.; Tsotsalas, M. Synthesis of Dynamic Covalent Polymer via Nitroxide Exchange Reaction, Biennial Meeting of the GDCh-Division of Macromolecular Chemistry, Karlsruhe (DE), 2018.

9. Acknowledgment

First, I want to thank my supervisor Dr. Manuel Tsotsalas for the extraordinary mentoring and the possibility to do my thesis in his group. Especially, I want to thank him for giving me the opportunity to work on all these interesting projects and for his support during the realization.

Furthermore, I want to thank Prof. Patrick Théato for accepting to be the co-referee of my thesis and appreciate the time he contributed for reviewing my thesis.

For the synthesis of all building blocks, I want to thank Dr. Isabelle Wessely, Yannick Matt and Prof. Dr. Stefan Bräse at IOC. The realization of all these interesting projects will never be possible without their valuable cooperation.

I'd also like to express my gratitude to Prof. Christof Wöll for giving me the opportunity to work at the Institute of Functional Interfaces during my studies and use all required facilities.

I would like to thank Dr. Hartmut Gliemann and Dr. Peter Weidler for their help and support as the department heads for the organization matter during my time in IFG.

I would like to thank Dr. Peter Weidler, Stefan Heißler, Peter Krolla and for offering me the training of diverse characterization methods and also for the helpful discussion for my projects.

I would like to thank all recent and former COOI members for their support in the past three years. I really appreciate the time to work with you.

I want to thank Dr. David Sulzer and Dr. Angela Bihlmeier for the support with their quantum chemical calculations.

I also want to thank Dr. Audrey Llevot for guiding me into the field of polymer science and also the LCPO group for my short stay in Bordeaux.

For fruitful discussions as well as their help through proof reading, I want to acknowledge the constant support of Dr. Zahid Hassan, Dr. Hatice Mutlu and Dr. Audrey Llevot.

For measurement of DSC I want to thank Dr. Hatice Mutlu, for the measurement of TGA I want to express my gratitude to Dr. Dominique Mook.

For the possibility to use their Ar sorption instrument, I want to thank Dr. Alexei Kiselev from the Institute of Meteorology and Climate Research.

I want to thank the Deutsche Forschungsgemeinschaft (DFG) within the Collaborative Research Center 1176 (SFB1176) for the financial support during my study at KIT.

The special thank is dedicated to my parents and my cousin Meng, for the support and cheering me up during the past three years.

Last but not least, my deep gratitude is dedicated to my beloved husband Kai, thank you for your continuous love, your understanding and your unlimited support in the life as well as in research field as a mentor during the past three years.